Morphologies of Selective Area Grown Nanowires

Material Distributions and Equilibrium Faceting of SAG Structures

Master's Thesis
Written by *Tobias Særkjær*

Supervised by
Peter Krogstrup

Co-Supervised by
Sergej Schuwalow and Tomaš Stankevič

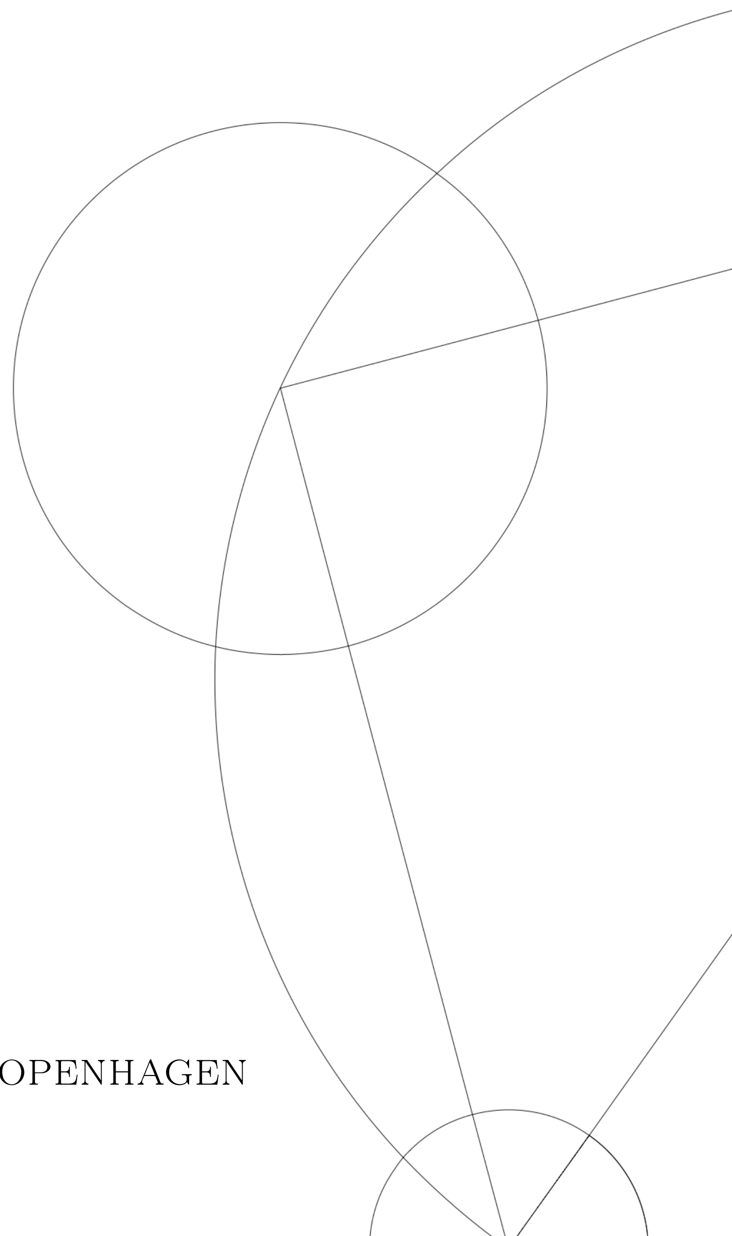

University of Copenhagen

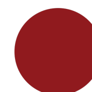

UNIVERSITY OF COPENHAGEN

NAME OF INSTITUTE:	Niels Bohr Institute
NAME OF DEPARTMENT:	Center for Quantum Devices
AUTHOR(S):	Tobias Særkjær
EMAIL:	znl919@alumni.ku.dk
TITLE AND SUBTITLE:	Morphologies of Selective Area Grown Nanowires - Material Distributions and Equilibrium Faceting of SAG Structures
SUPERVISOR(S):	Peter Krogstrup Co-Supervised by Sergej Schuwalow and Tomaš Stankevič
HANDED IN:	2020-06-13
DEFENDED:	2020-06-26

NAME ____________________

SIGNATURE ____________________

DATE ____________________

Abstract

Simulations of materials with properties interesting for applications in quantum computing has so far been mostly focused on understanding the electronic structures and associated phenomena in the presence of interfaces. While this is indeed of utmost importance, the strict requirements for uniformity in nanowire (NW) structures emphasizes the importance of understanding and control of morphological parameters in NW systems.
This thesis shows modelling of nanowire morphologies from selective area growth (SAG) in two different "domains".
First, the overall distribution of crystal volume is examined by way of coupled diffusion equations describing the steady state adatom density during growth, including incoming beam flux, incorporation and desorption. The model reliably reproduces the trends from analyses of final mass distribution in experiments.
Second, the shaping of crystal volumes is modelled by way of constrained Wulff shaping (CWS), equilibrium shapes minimizing the surface energy under constraints imposed by the chosen SAG lithography.
Finally, in the last section we examine the changes in chemical potentials associated with growth of crystal volume for a generalized shape, setting up the framework for dynamic modelling of crystal growth.

Resumé

Simulationer af materialer med egenskaber relevante for brug i kvantecomputere har indtil nu primært været fokuseret på forståelse af den elektroniske struktur og associerede fænomener nær grænseflader. Dette er yderst vigtigt, men de strenge krav for ensformighed i nanowire-strukturer understreger nødvendigheden for forståelse af og kontrol over de morfologiske parametre i nanowire-systemer.
Dette speciale viser modeller for nanowire-morfologier fra selective area growth (SAG) i to forskellige "domæner".
Først undersøges den overordnede fordeling af krystalvolumen via koblede diffusionsligninger, der beskriver statisk fordeling af adatomer under vækst, inklusiv indkommende stråleflux, inkorporation og desorption. Modellen reproducerer på pålidelig vis trends fra analyser af endelige massedistributioner fra eksperimenter.
Dernæst simuleres udformningen af krystaller via betingede Wulff former (CWS), ekvilibriumsformer som minimerer overfladeenergi under betingelser forbundet med SAG-litografien.
I det sidste afsnit undersøger vi ændringer i kemiske potentialer forårsaget af krystalvækst for generaliserede former, og lægger fundamentet for dynamiske simulationer af krystalvækst.

Contents

1 Introduction 4

2 Basics of SAG in MBE 6
- 2.1 Basics of Molecular Beam Epitaxy (MBE) . . . 6
- 2.2 Basics of Crystal Growth . . . 7
- 2.3 Basics of Selective Area Growth (SAG) . . . 10

3 Adatom Density from Diffusion Equations 14
- 3.1 Basics of Diffusion . . . 14
- 3.2 1D SAG Diffusion Equations . . . 15
- 3.3 Solutions to 1D SAG Diffusion Equations . . . 16

4 Faceting of Crystal NWs 20
- 4.1 Wulff Construction . . . 21
- 4.2 Surface Energy Densities from DFT . . . 24
- 4.3 γ-plot for GaAs in the $[1\bar{1}0]$ Zone Axis . . . 25
- 4.4 Constrained Wulff Shaping (CWS) . . . 27
  - 4.4.1 3-facet Equilibrium NW Model . . . 27
  - 4.4.2 4-facet Equilibrium NW Model . . . 31
  - 4.4.3 5-facet Equilibrium NW Model . . . 32
  - 4.4.4 6-facet Equilibrium NW Model . . . 35
  - 4.4.5 CWS Fitting of Equilibrium Shapes . . . 36

5 Crystal Growth Driving Forces 41
- 5.1 3-facet Chemical Potential Model . . . 42
- 5.2 5-facet Chemical Potential Model . . . 47
  - 5.2.1 Adding Crystal Volume on Facet t . . . 50
  - 5.2.2 Adding Crystal Volume on Facet i . . . 52
  - 5.2.3 Adding Crystal Volume on Facet o . . . 53
  - 5.2.4 Adding Crystal Volume on Facet v . . . 54

6 Future Work: Dynamic Modelling 57

7 Conclusion 60
- 7.1 Acknowledgements . . . 60

8 Appendix 64
- 8.1 Diffusion Solutions for Steady State Adatom Density . . . 64
  - 8.1.1 Diffusion Solutions and Rates . . . 64
  - 8.1.2 Diffusion Solutions and Nanowire Pitch . . . 65
- 8.2 Stereographic Projection for [100] type NWs . . . 65
- 8.3 3-facet Model Analytic Solutions for CWS . . . 65
- 8.4 MATLAB codes . . . 70

8.4.1 fourarray_bvp5c 70
8.4.2 gamma_plot 74
8.4.3 wulff_caller_timovr 76
8.4.4 wulff_func_timovr 79
8.4.5 excesses_dGdN 80

1 Introduction

In 2003 Kitaev [1] published a seminal paper on quantum computing, which opened a research path followed to this day. In short, the basic idea of Kitaev's proposal is topological protection of the quantum states used in calculations performed by manipulation of qubits. Systems without topological protection experience decoherence due to interactions with their environment, and must go to great lengths in order to safeguard and error-correct data across multiple qubits. Topologically protected systems would inherently address this problem and yield increases to qubit efficiency of several orders of magnitude [2], by eliminating the need for error correction. The implications of achieving reliable and scalable production of topologically protected qubits are difficult to overstate, and the academic interest in this field is well warranted.

One promising platform for topologically protected qubits is the Majorana Fermion or Majorana Zero Mode, the emergence of which could be realized in Semiconductor-Superconductor Nanowire (NW) Heterostructures [3]. This design rests on Zeeman splitting of spin states without exceeding the critical field for the superconductor. Materials such as the III-V semiconductors InAs or InSb are interesting for NWs, due to their high spin-orbit coupling and low band gap, which makes them viable as transport channels with proximity induced superconductivity.

In terms of architecture, the designs proposed by Karzig et. al. [4] in order to realize a qubit which meets the necessary requirements for operations and measurements share a key feature: arrays of parallel semiconductor NWs (see figure 5). This sort of design almost calls for Selective Area Growth (SAG), which shows great promise in terms of both control and scalability of devices. With SAG the NW material of choice is grown in lithographically defined patterns onto a substrate, which is typically another III-V semiconductor with a larger band gap, such as GaAs or InP. While certain combinations of substrate/NW materials are approximately lattice matched, one typically can grow a "buffer" of the substrate material to allow the NW some additional freedom for relaxation of misfit strain in order to minimize misfit dislocations [5].

SAG is well understood in terms of masking of growth patterns, controlling temperatures and fluxes for selectivity [6], and alloying materials in an attempt to obtain desirable material properties. However, cross-sectional analyses of SAG structures show a surprising variety of morphologies, as well as dislocations, associated strain fields, and complicated material distributions for ternary alloys. A necessity for better understanding the actual kinetics of crystal growth arises with the extreme requirements for uniformity for applications in quantum computing.

The theoretical framework of this thesis falls into two main parts. The first part applies Fick theory of diffusion in an examination of the large scale distribution of adatoms across different parts of the SAG pattern. The second part employs constrained Wulff shaping (CWS) in a study of NW shape evolution as a function of available crystal volume. Along the way, both parts are compared to experimental observations, demonstrating the generality of methods and tranferability across geometries and material compositions. The primary work is carried out for NWs grown along the $[1\bar{1}0]$ direction on a

(001) substrate, but the method is directly transferable to other directions and substrate types.

In total, the theoretical framework developed serves to explain some of the overall trends observed in crystal growth by way of Molecular Beam Epitaxy (MBE), from the distribution of crystal volume on larger scales, to the faceted structures of NWs that emerge as a final result. Finally, an initial framework for further studies of the kinetics through dynamic modelling is established through considerations of surface excess chemical potentials.

2 Basics of SAG in MBE

Any effort to predict dynamics of SAG growth in MBE must start from a basic understanding of the system in question. We will start with a basic description of the workings of the MBE, the system of machinery in which the crystal is grown. This is followed by a general description of crystal growth in terms of transitions between generalized states, since diffusion of material can be described as the transition between initial and final positional states, and crystal growth is the transition into the solid phase. Subsequently we will provide a basic description of SAG, masking, lithography and tuning of selectivity to obtain crystal growth on select parts of a masked substrate. Together these three parts outline the central features of how crystalline structures such as NWs are grown in MBE.

2.1 Basics of Molecular Beam Epitaxy (MBE)

MBE is the method of choice for growing nanosize crystal structures due to the level of control that is obtainable. The workings of an MBE system is a science in and of itself, and a more detailed description of the intricate mechanisms involved in the design and operation of MBE can be found in literature [7]. While these details are interesting indeed, they are also mostly unnecessary for the theoretical work in this thesis, most of which relies on quite a simple model.

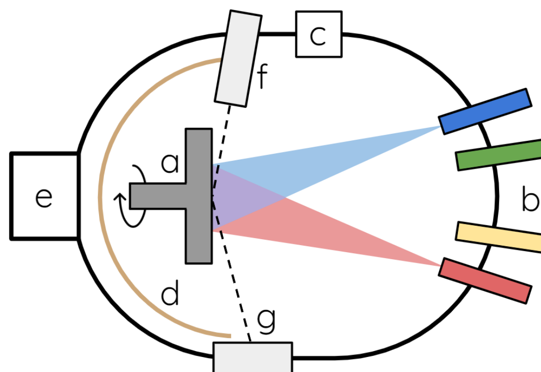

Figure 1: Schematic of MBE with indications of components. a) Rotating substrate holder and heater. b) Effusion cells. c) Vacuum pump(s). d) Cryo shrouds. e) Load lock. f) RHEED gun. g) RHEED screen.

The key components of the MBE are shown in figure 1. The sample, in this case our lithographically patterned substrate, is attached to the sample holder (**a**), which keeps the sample at a controlled temperature during growth, and rotates throughout to ensure an even distribution of atoms incoming from the effusion cells. Once atoms from the incoming beam reach the sample, they adsorp onto the surface and become adatoms available in the system.

The effusion cells (**b**) are the sources of materials (e.g. In, Ga or As atoms) chosen

for a given growth. The workings of the effusion cells vary from material to material, but effectively the effusion cells can be thought of as a bombarding the substrate with atoms of the chosen element. The flux of incoming atoms can be controlled separately for each species by setting the temperature of the material or adjusting the valve opening, and shutters in front of each effusion cell ensures the ability to shut off the supply with high precision timing, allowing formation of atomically sharp boundaries between different crystals.

The vacuum pumps (**c**) ensure that the entire MBE is kept at an ultra high vacuum (UHV) to avoid unwanted atoms contaminating the sample grown or interacting with atoms from our effusion cells. Different systems of pumps are available, and typically one pump brings the system to high vacuum, at which point another system of pumps kicks in to bring the pressure down to the UHV range of $10^{-9} - 10^{-11}$ Torr. The cryo shrouds (**d**) further help to lower the pressure by thermally trapping stray atoms, and access to the system is gated by the load lock (**e**), which acts as a preparatory vacuum chamber with initial degassing.

The Reflection High-Energy Electron Diffraction setup (**f** and **g**) emits high-energy electrons at a very shallow angle and detects the diffraction coming from the surface of the growing crystal. Diffraction intensity will fluctuate depending on the roughness of the topmost growth layer, which allows for real-time tracking of the exact number of monolayers (MLs) grown measured by RHEED oscillations [8, 9] as well as extraction of other information about the material.

2.2 Basics of Crystal Growth

This section follows the formalism laid out by Krogstrup et al. (2013) [10] for III-V NW growth, in this case applied to SAG. While the growth is for a III-V material, in the following we shall consider the kinetics of the group III adatoms only (we will describe the adatom state below). The reason for this simplification is adequate overpressure of the corresponding group V beam (see section 2.3). In short, we assume the group V adatoms to be present whenever needed[1]. This is a typical growth regime, where the group V species, such as As in the case of GaAs, is constantly supplied from the effusion cells. At substrate temperatures of roughly 500°C As atoms do not stick to the surface to build an As layer, but quickly desorp. Without continuous As overpressure in the MBE chamber, As would desorp from the substrate, damaging the original substrate or undoing the growth.

We shall consider four main types of states for the element type grown:

1. (f) beam flux incoming from the effusion cells. This is an effective beam flux after subtrating the desorption.

[1] This assumption is kept in order to simplify our model, although experimental observations indicate that group V overpressure is not simply saturated under typical growth conditions. A more detailed model would include inter-diffusion of both groups III and V species and interactions between these, which is outside the scope of this thesis.

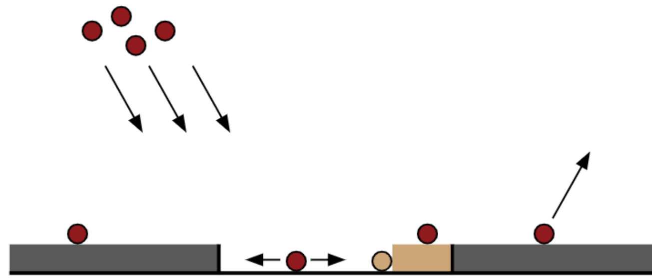

Figure 2: Different phase transitions relevant for SAG growth. Mask marked by grey, trench without mask in the middle. From the top is a uniform beam incoming from effusion cells (see section 2.1) adsorbing into adatoms (red circles) available across the geometry. Some growth has already occurred in the trench (marked in gold), and one adatom (gold circle) is about to undergo transition from adatom to solid to contribute to growth. On the right another adatom is about to undergo desorption back to vapor phase and disappear from the system. All adatoms undergo random walk. Not shown is the initial nucleation of the growth in the trench.

2. (a) adatom phase. Atoms incoming from the beam undergo adsorption, and become adatoms available for diffusion (see section 3.1), desorption or incorporation into the crystal. Adatoms are "loosely" bound to the surface, not yet incorporated into the crystal but on the crystal surface.

3. (s) solid state or crystal phase. The state in which the atom has incorporated and contributed to growth of the crystal. We can think of this as the "final" phase, although transitions from the crystal phase to adatom or vapor phase (desorption) are in principle available.

4. (v) vapor phase. When an adatom transitions into vapor phase, it desorbs and leaves the system.

Our actual interest is transitions between these main types of states. For clarity we shall give a short description of the main types of transitions between states, and our treatment of these transitions going forward (see section 3.2). The following describes net transition rates as the difference between gross transition rates.:

1. ($f \to a$) Incoming beam flux is converted into adatom phase. Any conversion factor between the two can be absorbed, so the effective beam flux, f, can be thought of as the incoming amount of adatoms (per unit time per unit area). As such, this transition will be treated as just a term for adatoms being spontaneously created by way of beam flux (in equation 8) uniformly across the geometry. Since incoming beam flux is distinguished from desorbing vapor phase, there are no transitions to state f. Note that incoming beam flux is also often phrased in terms of a corresponding growth rate of monolayers per second (ML/s) for "planar" growth of a large film.

2. ($a \to a'$) The diffusion of adatoms (see section 3.1) is in principle the transition from the adatom state in one lattice site to the adatom state in another lattice site. This transition will be treated with a Fickian diffusion term (see section 3.1 and equation 8).

3. ($a \to s$) The incorporation of adatoms into the crystal is the transition from adatom to solid state. Selectivity (see section 2.3) and our picture of net rates as the difference in gross rates (explained further below) means that there is effectively no net transition from state s to state a.

4. ($a \to v$) The desorption of an adatom is the transition from adatom to vapor state. Vapor state atoms could in principle re-adsorb and become part of the system, and we shall treat this as a correction yielding a net transition rate in section 3.2.

To shorten our expressions going foward, the transition $p \to q$ will from here on out be shortened to pq, implicitly referring to states of the group III atoms in states either on the mask or in a trench. Figure 3 depicts the energetic landscape in Gibbs free energy for a generalized pq transition.

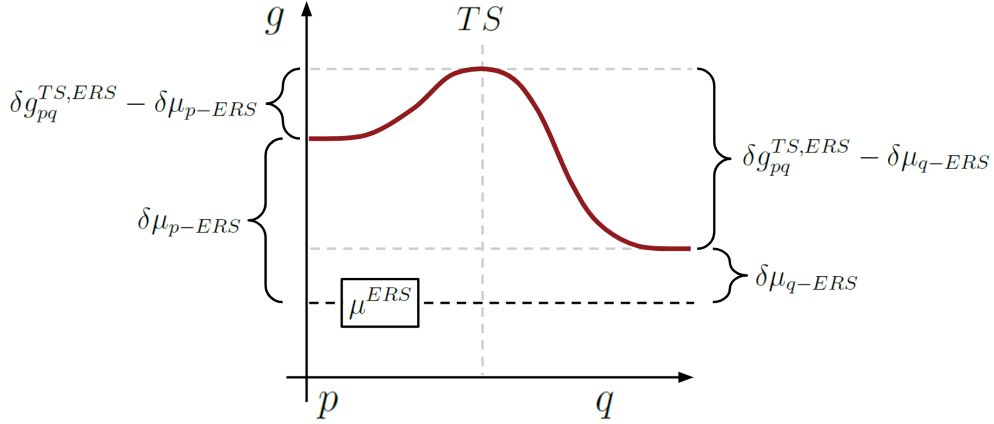

Figure 3: Energetics of phase transitions. The horizontal axis denotes states, and the vertical axis the Gibbs free energy. The dashed black line indicates the energy of the equilibrium reference state.

All our energies are defined with respect to an equilibrium reference state (ERS), which can conveniently be chosen to be the bulk solid of the given semiconductor [10]. The energy of this ERS is marked as μ^{ERS} in figure 3. The energy of state p is thus:

$$\delta\mu_{p-ERS} = \mu_p - \mu^{ERS} \tag{1}$$

with a corresponding expression for q. The energetic barrier mentioned above for the pq transition is the quantity:

$$\delta g_{pq}^{TS} = \delta g_{pq}^{TS,ERS} - \delta\mu_{p-ERS} \neq \delta g_{qp}^{TS} \tag{2}$$

where the last inequality is included to highlight that the energetic barrier for transition pq is in general different from that for the transition qp, which should also be evident from the difference in "levels" on the left and right sides of figure 3. Note that the energetic landscape in figure 3 shows a reversible transition, in that the Gibbs free energy of the transition state is the same for pq as for qp.

In general the expression for the transition probability pq is an exponential:

$$P_{pq} \propto \exp\Big(-\delta g_{pq}^{TS}/k_B T\Big) \tag{3}$$

and thus the gross transition rate for pq is given as:

$$\Gamma_{pq} = \Xi_{pq}\rho_p \exp\Big(-\delta g_{pq}^{TS}/k_B T\Big) \tag{4}$$

where Ξ_{pq} is the attempt rate or knocking rate per atom in state p with any factor of proportionality from equation 3 absorbed, and ρ_p is the density of atoms in state p. Since we are interested in net transition rates, the expression for the net transition rate pq becomes a bit more involved:

$$\Delta\Gamma_{pq} = \Gamma_{pq} - \Gamma_{qp} = \Xi_{pq}\rho_p \exp\Big(-\delta g_{pq}^{TS}/k_B T\Big) - \Xi_{qp}\rho_q \exp\Big(-\delta g_{qp}^{TS}/k_B T\Big) \tag{5}$$

While equation 5 has quite a complicated form, we shall apply some simplifying assumptions for transitions relevant for our system in section 3.2. First we will need to review some key features of SAG.

2.3 Basics of Selective Area Growth (SAG)

As an initial step for SAG, a substrate is prepared to serve as a basis for the growth. In the simple case of homoepitaxial growth, the substrate is prepared from the same III/V material as the crystal that is about to be grown. A pattern is designed, depending on the desired geometry, and masking out trenches is achieved by a combination of deposition of masking material, deposition of resist, lithography and etching. Each of these steps can be achieved in a variety of ways, depending on which methods are compatible with the choice of materials. The result is a substrate that is entirely covered by a masking agent, except for the "trenches" where the substrate is exposed. The NWs will eventually grow in these trenches, so regions are labeled as NW or trench regions interchangeably, always as opposed to mask regions (see figures 5 and 6).

As mentioned in section 2.2 above, we can simplify our conceptual model by adequate group V overpressure. While the actual physical system has a complex process of both groups III and V species, the overpressure lets us assume that the necessary group V atoms are present whenever needed. Thus the availability of the group III species becomes the relevant factor.

Since some parts of the substrate are directly exposed in the NW regions, while other parts are covered by the masking agent, an atom on a surface will be subject to very

different conditions, depending on the region in which it is located. This corresponds to transition rates $\Delta\Gamma_{pq}$ from equation 5 with two different sets of states pq and $p'q'$, depending on NW or mask region. In section 3.2 we shall denote this with a superscript: $\Delta\Gamma^{m}_{pq}$ with m denoting the material as either NW or mask region. The available transitions are the same in both types of regions, but the different energetic landscapes cause large differences in the transition rates, as outlined in section 2.2.

In general a group III type atom incoming from the molecular beam, will adsorb on to on a surface of the sample, either NW or mask region or mask, and thus become an adatom available in the system. From here, the adatom ultimately has two possible fates. The adatom can end up incorporating as part of the crystal, either in a NW or mask region by transition with the rate $\Delta\Gamma^{m}_{as}$, where as means adatom to solid (see section 2.2). Alternatively the adatom can end up not contributing to growth, by desorption back to vapor (av) from either a NW or mask region with transition rate $\Delta\Gamma^{m}_{av}$.

However, between an atom starting it's life as an adatom and ending it by incorporation or desorption, the adatom can undergo a long series of events. Very importantly, the adatom undergoes transitions governed by the rate $\Delta\Gamma^{mm'}_{aa'}$, which is non-zero unless states a and a' share material region and have equal densities ρ_a and $\rho_{a'}$ (see equation 5). These transitions are responsible for adatom diffusion, as we shall see in section 3.1. Note that these transitions can cross material boundaries between NW and mask regions, which is the reason for the double superscript mm' above.

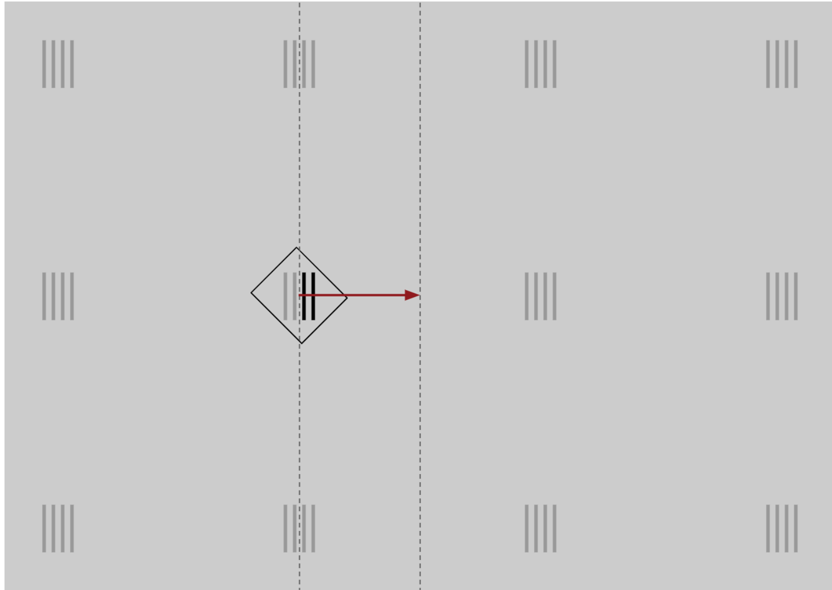

Figure 4: Schematic of 4-arrays of NWs (dark grey) on part of a larger mask (light grey). Box indicates zoomed region shown as SEM in figure 5. Black NWs correspond to those depicted in the schematic in figure 6. Dashed vertical lines indicate planes of mirror symmetry, allowing for examination of 1-dimensional axis indicated by arrow. The distance between 4-arrays is much larger than the length of NWs, L_{NW}.

For practical reasons the pattern studied in this thesis is a general pattern consisting on 4 NWs surrounded by a mask (see figures 4 and 5). The geometry is reduced by planes of mirror symmetry, since the overall pattern is symmetric. With this type of pattern, large amounts of experimental data is available to the author for comparison, since this type of masking has been used extensively for growths available through Microsoft Quantum Materials Lab (MQML) Lyngby due to relevance for realizing topologically protected qubits as mentioned in section 1.

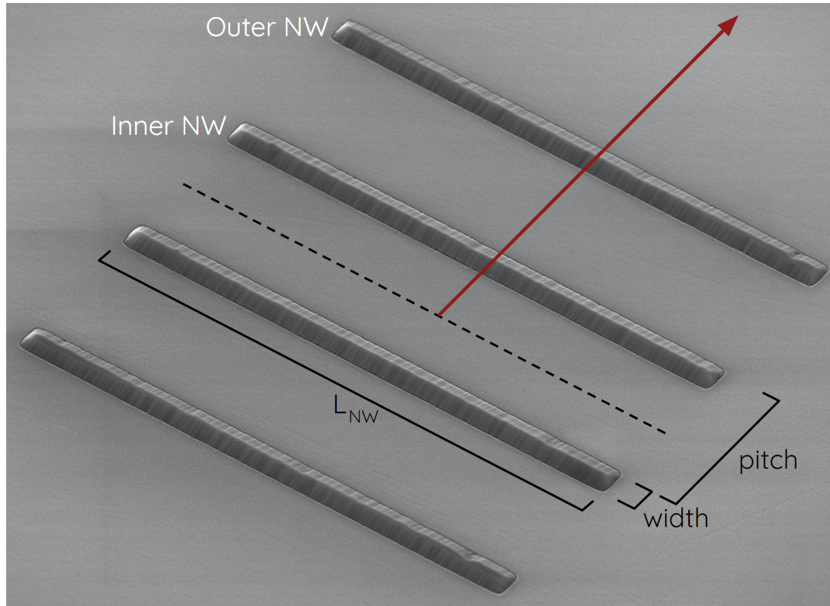

Figure 5: SEM image of 4-array of NWs grown in 4 trenches with surrounding mask. The dashed line indicates one plane of mirror symmetry, the other one being located outside the picture (see figure 4). The red arrow indicates part of the 1-dimensional axis in the problem, assuming axial translational symmetry. Dimensions are labeled with *pitch* as the spatial periodicity of NWs, and *width* and L_{NW} being the dimensions of individual NWs. The NWs in this SEM image are approximately $5\mu m$ long.

While areas closer to the ends are subject to more complicated effects, the middle sections can be viewed as essentially a 1-dimensional system with translational symmetry along the length of the NWs (assuming $L_{NW} \gg pitch$), comparing figures 5 and 6 with the axis marked by the red arrow. For the entirety of this thesis we shall be concerned with this "bulk" or middle part of the NWs. We note that this 1-dimensional approach hinges on the relative dimensions in the geometry, and becomes increasingly vulnerable with increasing *pitch*, *width* or diffusion length (λ), or decreasing L_{NW}.

The features of the chosen pattern are consistent throughout this thesis (4 regions labeled as NWs or trenches, surrounded by a masked region), but it should be noted that the entire framework developed is valid for other patterns, assuming translational symmetry allowing for a reduction to a 1-dimensional problem.

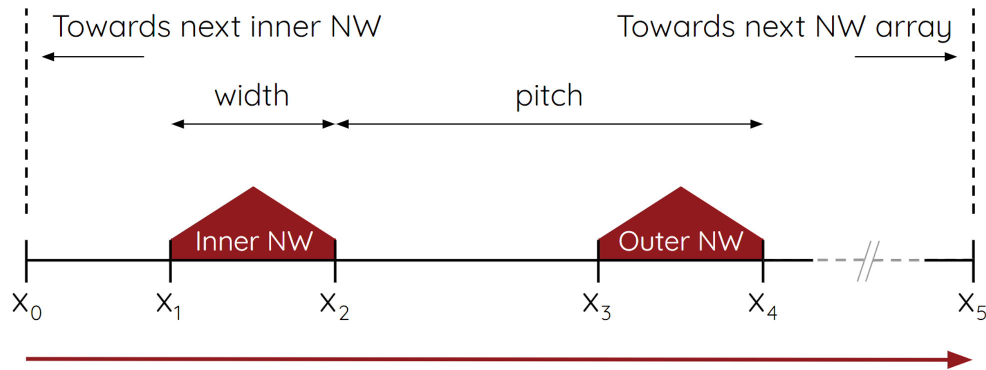

Figure 6: The 1-dimensional geometry for a 4-array of NWs. The dashed vertical lines indicate planes of mirror symmetry, with the two other NWs positioned to the left, mirrored in the leftmost plane. The red arrow indicates the direction of the same axis as marked in figure 5, where the plane x_0 is also shown. The dashed mask part on the right indicates a very large distance half way towards the next NW array (see figure 4).

In summary, for the purposes of the SAG MBE model in this thesis, the most important features of SAG are:

- We start from substrate covered by a masking agent apart from NW/trench regions. NW trenches and mask regions have different conditions for incorporation, desorption and diffusion (see figure 5).
- The relevant part of the geometry in question shows approximate translational symmetry, which allows for a 1-dimensional statement of the setup (compare figures 5 and 6).
- Atoms incoming from the beam adsorb onto a surface, becoming adatoms which undergo random walk governed by diffusion equations (see section 3.1).
- Adatoms end their random walk by either incorporation with contribution to growth or desorption back to vapor phase with no contribution to growth.

We will gather these features in coupled differential equations for diffusion in section 3.2 below.

3 Adatom Density from Diffusion Equations

Author's note: An edited version of this section is included in reference [11] by M. Espiñeira, A. W. Christensen, et.al. (2020).

3.1 Basics of Diffusion

As described in section 2.2 the crystal growth in MBE occurs due to adatoms making transitions between different states across the mask and the substrate. Each available lattice site can be thought of as a positional state with transitional states between lattice sites. The transitions are stochastic, and each adatom essentially undergoes a random walk, moving from one site to the other, from adsorption until eventual incorporation (transition to the solid phase) or desorption (transition back to the vapor phase). The different types of states are illustrated in figure 2.

It is well known, that particles undergoing random walks follow diffusion equations [12, 13] for mass distribution as a collective or for probability density for any given single particle. Diffusion equations have been successfully employed in other studies of MBE growth [10, 14], for e.g. vapor-liquid-solid growth (VLS) of free standing NWs.

The classical framework for diffusion is that of Fick diffusion [15], the essence of which can be stated in Fick's 1st and 2nd laws (for a 1-dimensional system). Fick's 1st law is often stated as:

$$J = -D\frac{dn}{dx} \tag{6}$$

where n is the count of the diffusing species, J (units in 1D: [count/time]) is the diffusive flux of this species in the direction of positive x, and D (units in 1D: [length/time]) is the diffusivity of the species[2]. The negative sign shows the general and intuitive trend, that the diffusing species moves from regions with higher concentration to regions with lower concentration. This is often phrased as diffusion "down the slope of the gradient".

Fick's 2nd law states:

$$\frac{\partial n}{\partial t} = D\frac{\partial^2 n}{\partial x^2} \tag{7}$$

relating the change over time to the distribution of the concentration. From differentiation of equation 6 we see that the right side of equation 7 is negative the spatial derivative of a flux; concentration increases for an area with more incoming flux than outgoing. This is essentially an expression of mass conservation, where a gradient of the flux must lead to an accumulation. The concept is illustrated in figure 7.

Here we should note the setup for Fick's laws: Fick studied the diffusion of salt in a solvent [15], a closed system in the sense that the total amount of salt is kept constant,

[2] Units of diffusivity and flux depend on dimensionality and the diffusing quantity. In 3 dimensions the flux, J, of a concentration, c, can be phrased with units of [number/(time $\times$ area)], where the flux is in the direction of positive x passing through the plane normal to x. The units of diffusivity are then [area/time], since the concentration has "inherent" units of [number/volume].

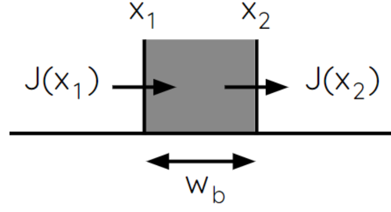

Figure 7: Diffusion of mass into and out of the small grey region of width w_b between x_1 and x_2. Two observations follow directly from conservation of mass: In case of $J(x_1) > J(x_2)$ we must have an accumulation of mass in the grey region, since more mass enters than leaves. In the limit of $w_b \to 0$ we must have $J(x_2) \to J(x_1)$, since mass cannot accumulate in a infinitely narrow region.

and only the distribution is changed. In our MBE system the total amount of adatoms available in the system changes due to all the transitions mentioned in section 2.2, and we have a steady influx of new adatoms via the beam from the effusion cells. As such we must tweak our version of equation 7 accordingly.

3.2 1D SAG Diffusion Equations

As described in section 2.1, the effusion cells of the MBE bombard the masked substrate with a steady beam of atoms, which adsorb and undergo diffusion, until they end up either contributing to growth or desorbing from the system. In our simplified model, the diffusing substance is the group III species of adatoms.

The total change in adatom density per unit time is caused by diffusion, desorption, growth and incoming beam flux (see figure 2) - or in equation form, adapted from equation 7:

$$\frac{\partial \rho(x)}{\partial t} = D\frac{\partial^2 \rho(x)}{\partial x^2} - \Delta\Gamma_{av}(x) - \Delta\Gamma_{as}(x) + f_{III}(x) \tag{8}$$

In equation 8 above, $\rho(x)$ is the adatom density, D is the diffusivity, $\Delta\Gamma^s_{av/as}$ denotes the net transition rates from adatom to vapor/solid (see section 2.2 and equation 5), and $f_{III}(x)$ is a rate of incoming group III adatoms from the molecular beam. The first term on the right denotes the rate of change in adatom concentration due to diffusion, as we would expect from equation 7. The next two negative terms are adatoms lost to desorption and incorporation, and the last term is adatoms gained by impinging beam from the effusion cells.

Assuming that the crystal prefers to grow in trenches over growing on the surface of the mask (good selectivity), we note a low probability for desorption in NW regions due to a high binding energy in the crystal phase:

$$\Gamma^{NW}_{sa} \ll \Gamma^{NW}_{as} \tag{9}$$

We also note that for steady state the density of atoms in the vapor phase should be proportional to the density of adatoms times the transition probability av:

$$\rho_v \propto \rho_a \exp\left(-\delta g_{av}^{TS} \right) \tag{10}$$

Using equations 9 and 10 with equation 5 allow us to recast the rates $\Delta\Gamma_{av}(x)$ and $\Delta\Gamma_{as}(x)$, and an assumption of a uniform beam from the effusion cells lets us restate equation 8 in steady state as:

$$0 = D_m \frac{\partial^2 \rho(x)}{\partial x^2} - \rho(x)\left(\nu_{av}^m + \nu_{as}^m\right) + f \tag{11}$$

where ν_{av}^m and ν_{as}^m are now the desorption (adatom-to-vapor) and growth (adatom-to-solid) rates per adatom on material m. We have renamed our beam flux $f_{III}(x)$ to just f for simplicity, since it is uniform. We note that our choice of steady state is for sake of simplicity; we know that the NWs grow over time, and thus the geometry underlying the problem is constantly evolving. However, a steady state solution might still serve to enlighten the problem and show trends.

Equation 11 looks deceptively simple, but the sub-/superscript m is a reminder that a material dependent version of this equation must hold simultaneously on each material region of figure 6, with diffusivities and transition rates being functions of region. This makes the problem a multi-point boundary value problem (mpbvp). We note that we can treat equation 11 with "exploratory" values for D_m, ν_{av}^m, ν_{as}^m in order to examine the trends produces for a variety of diffusivities and transition rates.

The mpbvp stated in equation 11 above can be solved numerically for the geometry outlined in figure 6 by mpbvp solvers, given appropriate boundary conditions. The boundary conditions in question are:

1. Zero flux ($\partial\rho(x)/\partial x = 0$) at external boundaries x_0 and x_5 due to the symmetries in the problem and Fick's first law. Since all parameters are mirror symmetric across the boundary, the net flux of adatoms across the boundary is zero.

2. Flux continuity at internal boundaries x_1 through x_4. Adatoms exiting one region must enter the next region. This is illustrated in figure 7 with $w_b = 0$.

3. Continuity of adatom density at internal boundaries x_1 through x_4.

3.3 Solutions to 1D SAG Diffusion Equations

Our choice mpbvp solver is the `'bvp5c'`[3] from MATLAB [16] (for code see appendix section 8.4.1). While the "inner workings" of this solver are interesting from a mathematical or programming perspective, we shall resort to just utilizing the solver as a tool for this thesis. Each region of the geometry in figure 6 is defined with a separate set of differential equations corresponding to equation 11, with material parameters kept

[3] Documentation for `'bvp5c'`: https://www.mathworks.com/help/matlab/ref/bvp5c.html

constant in regions of the same type. The solver computes a solution which satisfies the differential equations on a mesh across all regions simultaneously, while obeying the boundary conditions on each boundary. Leaving NW pitch, width (see figure 6) and rates as variable parameters allows for an examination of the steady state adatom density as a function of these. As commented in section 3.2 above, we can explore the parameter space of different values for D_m, ν_{av}^m, ν_{as}^m dependent on material region.

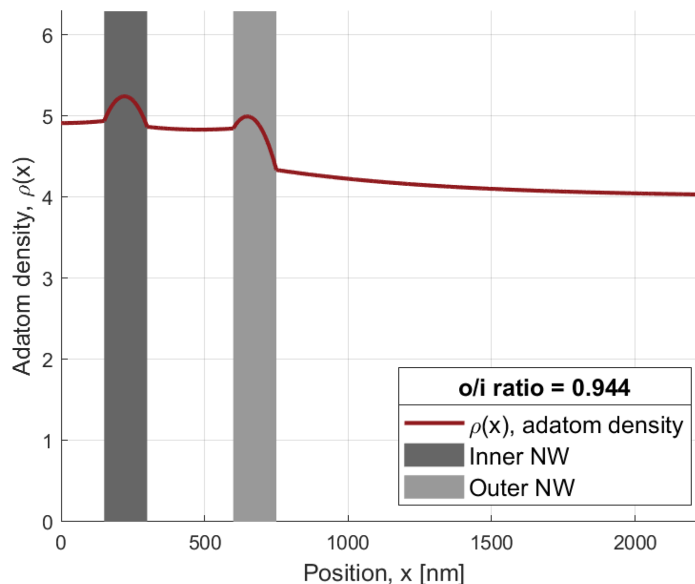

Figure 8: The steady state adatom density is plotted across part of the 1-dimensional geometry for a 4-array of NWs. The "o/i ratio" displayed is the ratio of the adatom density summed across the outer NW and the inner NW. In this case the desorption rate on the mask is 2.5 times higher than the incorporation rate in the trenches.

One such solution generated through the use of `'bvp5c'` with exploratory values is shown in figure 8, with the desorption rate on the mask being 2.5 times the incorporation rate in the trenches (see more examples in section 8.1.1). We note a clear trend in figure 8 with more adatoms towards the inner NW compared to the outer NW. We label this "**source behaviour**", where the NWs act as sources of adatoms in terms of diffusion. The diffusion is driven by adatoms disappearing more rapidly on the mask due to desorption than on the NWs due to growth. The dynamics of crystal growth are much more complex than this simplified picture, but our "source model" shows that some experimentally observed trends (see below) can be caused by diffusion during growth. This is, of course, through an assumption of a positive correlation between steady state adatom density and final crystal volume.

Figure 9 shows experimental data by Anna Wulff Christensen [17], which displays growth volume for 4-arrays of NWs measured by atomic force microscopy (AFM). The data shows two trends: inner NWs show more volume that outer NWs, and all NWs grow

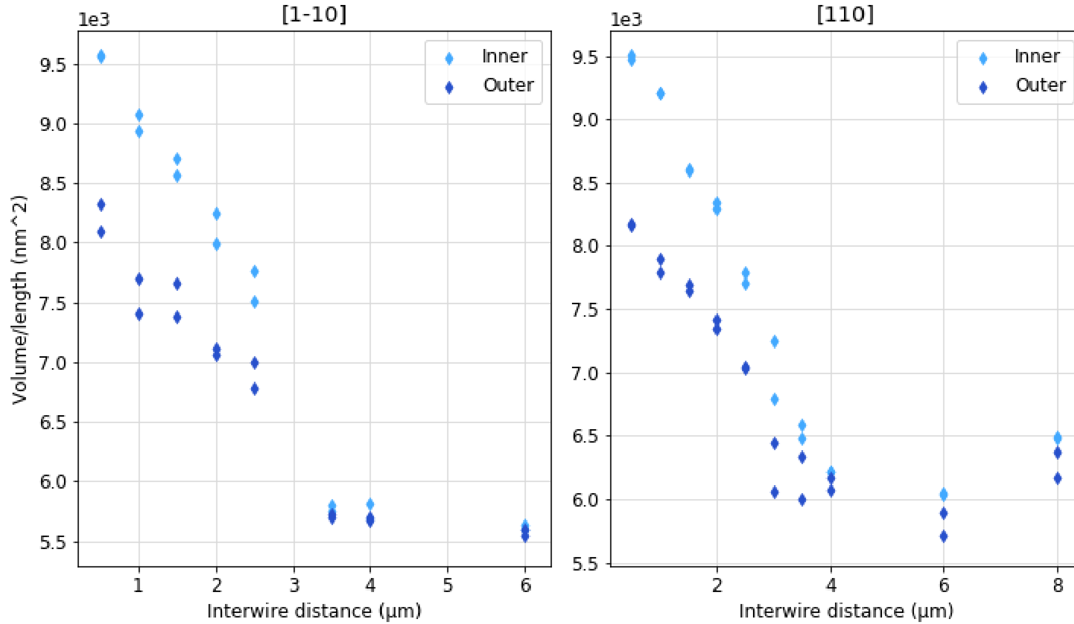

Figure 9: Experimental data of 4-arrays of NWs measured by Anna Wulff Christensen [17], showing a consistent trend of higher growth rates on inner NWs than outer NWs, as well as growth rates decreasing with increasing pitch. Labels on top show NW directions. "Interwire distance" on the x-axis is pitch, and the y-axis shows average cross sectional area.

less rapidly with increasing pitch. Both trends are well explained by the present model of source behaviour for the steady state adatom density (see section 8.1.2). In simplified terms, inner NWs have a higher steady state adatom density, and thus grow more rapidly, since they have two neighbor sources, while outer NWs have just one. Increasing pitch increases the distance between source NWs and thus more adatoms undergo desorption while travelling between NWs, decreasing the overall growth rate.

The source behaviour also explains experimental observations that the incorporation rate in masked SAG growth is experimentally significantly lower than the corresponding growth rate for planar 2D growths [11, 17]. Here we see a lifetime limiting mechanism in SAG, which is not present in planar growth: adatoms from a NW region can diffuse onto the mask, where the higher desorption rate offers an easier means of escape. The growth rate is lower in the masked SAG case compared to planar growth, since the adatoms can desorp through this two step process.

These two observations (and no growth on the mask) confirm that the adatom lifetime on the mask is desorption limited, as expected. Since the desorption probability in the SAG trenches should be the same as for planar growth (assuming equal conditions), there must be a net flux of adatoms from the trenches to the mask, causing the lower growth rate. A net flux from the trenches onto the mask must be caused by a negative gradient

in adatom density, and desorption must be the cause of this since incorporation on the mask is prohibited.

We should clarify what "source behaviour" means: the adatoms lost from the NWs due to diffusion are more than offset by the incoming beam, and as such the crystal volume in NW regions still grows over time. However, in terms of diffusion the NWs can act as if they have a negative collection area (that is, area of negative collection); during growth, the NWs can spew out adatoms in an area around them.

We must be cautious when attempting to quantitatively tie the steady state adatom density to a final volume for a given growth, for several reasons. There is no guarantee that the growth occurs primarily with steady state adatom distribution. Thus the final volume can be a complicated function of adatom density and other factors. The growth rate can easily vary even locally throughout growth, and the magnitude of the "source behaviour" can vary with it. This will be the focus of our attention when we examine driving forces much later in section 5. For now we will settle for the qualitative explanation of the experimentally observed trends.

While figure 8 shows a solution with source behaviour, this behaviour depends strongly on the transition rates in question. Further study of the steady state adatom distribution as function of the rates on the regions shows that the "source behaviour" can change to "sink behaviour" (where the net flux of adatoms is from mask regions to NW regions) if the incorporation rate on the mask is higher than the desorption rate on the mask. The rates can effectively be changed by a growth parameter such as temperature or pressure, as we saw in section 2.2. This rate-dependence of the source- or sink-behaviour is examined further in the appendix section 8.1.1. We note that a change from "source" to "sink behaviour" should be accompanied by a corresponding change in growth rate from lower than planar growth rate to higher.

Lastly we note that while figure 8 shows a clear variation of adatom density across a single NW domain, the specific distribution inside any given NW domain is assumed to depend not on the adatom density function but instead - at least as a first approach - on equilibrium shaping of the crystal volume inside a given domain. While the adatom density function tells us about trends in the distribution of crystal volume across the SAG geometry, the shaping or faceting of said volumes inside a NW region is treated in section 4 below.

4 Faceting of Crystal NWs

With the previous section 3.3 explaining the experimentally observed volume distribution across the SAG geometry, the next issue is faceting: the specific cross sectional shapes with quite clearly defined sharp edges seen in e.g. figures 5, 11 and 12. Other studies find similar clearly defined facets with variations depending on, among other parameters, substrate and NW orientation and of course the materials in question. The possible facets can be deduced via crystallography and basic linear algebra (the dot product between the Miller indices of the NW direction and any possible facet showing translational symmetry along the NW axis must be zero), and summarized in stereographic projections.

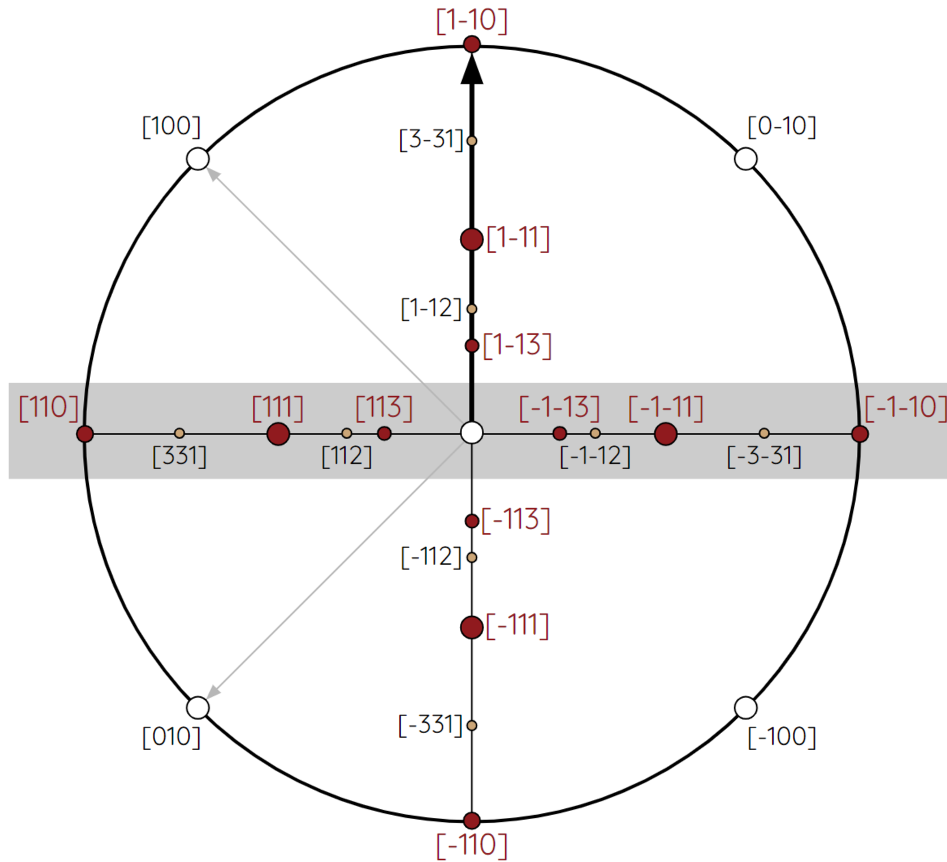

Figure 10: Part of a stereographic projection for zincblende on a (001) substrate with focus on the $[1\bar{1}0]$ type NW. The figure only shows the main directions and facets in the $\langle 110 \rangle$ type directions for increased readability. The $[1\bar{1}0]$ direction is upwards with allowed facets indicated by the normal directions perpendicular to the NW direction, marked by the shaded area. The angle with respect to the (001) substrate starts from $0°$ in the center and increases linearly to $90°$ at the perimeter.

The stereographic projection in figure 10 shows the high-symmetry facets for zincblende[4] for the $\langle 110 \rangle$[5] type NW directions on a (001) substrate, which will be relevant for our further studies. In principle a much wider range of directions could have been included in the same figure at the cost of readability. A similar projection for the $\langle 100 \rangle$ type NW directions on a (001) substrate can be found in the appendix section 8.2. We will focus our attention on the $[1\bar{1}0]$ type NWs with main facets indicated by red in figure 10 and summarized in table 1, but the method from here on out is directly transferable to other NW orientations and substrate types.

Figures 11 and 12 show two different growths of III-V semiconductor NWs in the $[1\bar{1}0]$ direction, specifically InAs on InP substrates. For "MQML115" in figure 11, one buffer of ternary alloy InGaAs was grown before InAs. The boundary between the buffer and NW layers is barely visible in figure 11b. In the case of "MQML190", two ternary alloyed InGaAs buffers were grown before the InAs NW. Both cases should obey the stereographic projection shown in figure 10, and clear faceting in correspondance with the expectation is observed. These types of observations together with the stereographic projection allow us to "pick" the facets for our study. First we need to review the basics of Wulff Construction.

4.1 Wulff Construction

Wulff Construction is best described as an algorithm for determining crystal facets based on an underlying γ-function. The γ-funcion is generally 3-dimensional and can be phrased in terms on spherical coordinates: $\gamma(r, \theta, \phi)$. It is expressed such that the radial value, r, of the γ-function is proportional to the surface energy density associated with the facet normal to the vector with angular coordinates θ and ϕ [19]. The γ-function must obey the bulk crystal symmetries, since equivalent planes must have equal surface energies. While the γ-function is explicitly phrased in terms of the spherical coordinates, it is of course implicitly also a function of the materials in question and the crystal environment.

To obtain a faceted crystal shape from the γ-function, we must proceed along the following steps (see figure 13):

1. Plot the γ-function with value r for each set of values (θ, ϕ).
2. At each point on the γ-function, draw the plane normal to the radial vector. The set of points defined by these planes constitutes our Initial Wulff Shape (IWS).

[4]The III-V compounds used for NWs in this thesis grow in zincblende structure on (001) substrates. The zincblende structure consists of two interpenetrating FCC structures offset by $\frac{a}{4}[111]$. This means that symmetry considerations of the FCC do not directly carry over to the zincblende structure. This shows up in experiments, e.g. in a large discrepancy in diffusion lengths observed experimentally along the two directions.

[5]While [110] and $[1\bar{1}0]$ type NWs are equivalent in terms of which facets can theoretically exist, the reconstructions of these facets may differ due to the difference between FCC and zincblende as explained in previous footnote. For generality we will stick with $\langle 110 \rangle$ directions whenever possible, and note that experimental observations shown in this thesis are from the $[1\bar{1}0]$ direction.

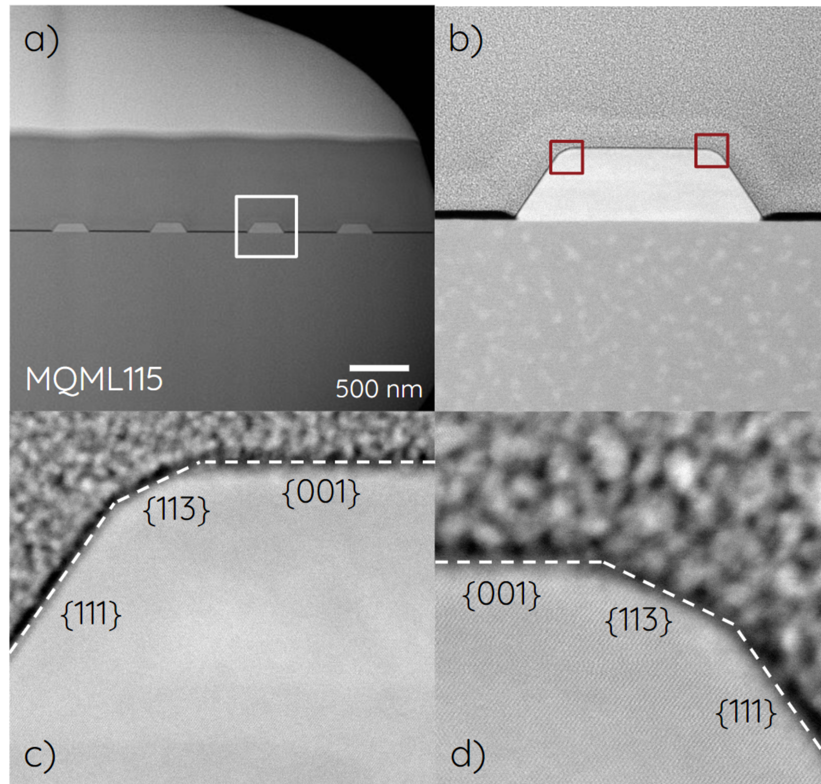

Figure 11: Cross sectional TEM images by Martín Espiñeira of a NW growth in regime 1, viewed in the $[1\bar{1}0]$ zone axis. "MQML115" is an internal growth ID with InP (001) substrate, InGaAs buffer and InAs NW. **a)** Overview of 4-array. **b)** Image of the single NW indicated in panel a. A very slight change in contrast is visible, indicating the InGaAs-InAs boundary. **c)** Zoom of section of single NW in panel b showing faceting. **d)** Another zoom section of single NW from panel b. Dashed lines are guides to the eye, indicating expected angles for the labeled facets.

3. Further restrict the IWS such that for every value of (θ, ϕ), we keep only the point in IWS with the lowest r-value.

4. The remaining points now constitute the Wulff shape.

The Wulff shape emerging from the algorithm described above constitutes the equilibrium crystal shape, in the sense that the shape minimizes the surface energy for a free floating crystal. It can be shown, that the Wulff shape is always convex [19, 20, 21], which allows us to draw a schematic representation of the allowed facets. Figure 13 shows a 2-dimensional example of the Wulff construction described above.

The bulk energy density is irrelevant for the shape, since the bulk contribution is equal for shapes of equal volumes. One immediate implication of this is, that the Wulff

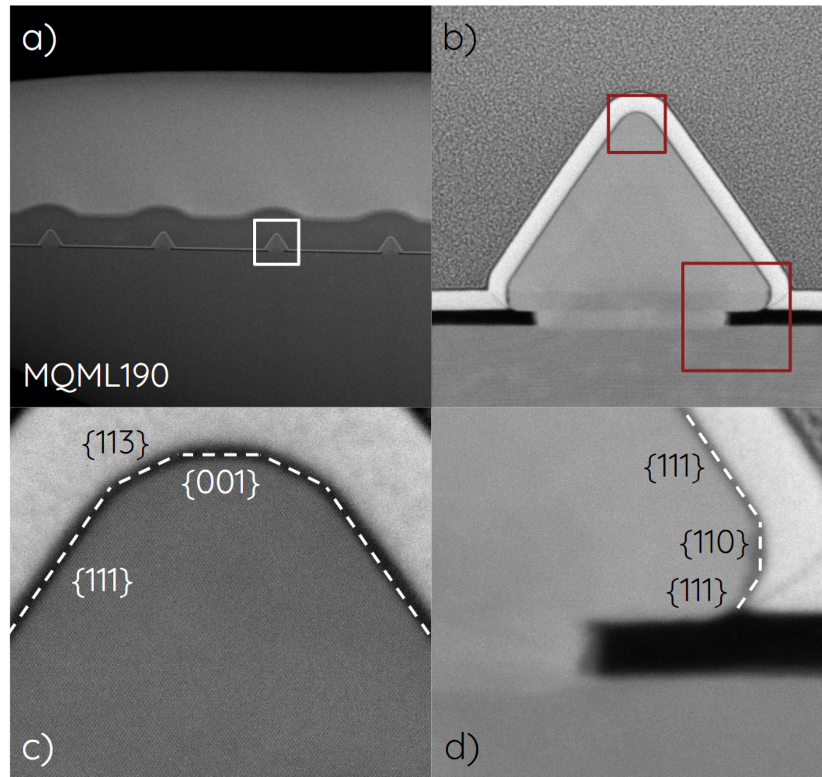

Figure 12: Cross sectional TEM images by Martín Espiñeira of a NW growth across regime 1 into regime 2, viewed in the $[1\bar{1}0]$ zone axis. "MQML190" is an internal growth ID with InP (001) substrate, two InGaAs buffers and InAs NW. **a)** Overview of 4-array. **b)** Image of the single NW indicated in panel a. **c)** Zoom of section of single NW in panel b showing faceting. **d)** Another zoom sections of single NW from panel b. Dashed lines are guides to the eye, indicating expected angles for the labeled facets.

shape is size independent[6]; a crystal of a larger volume has the same equilibrium shape just scaled to size. We also notice that a proportional rescaling of the surface energy densities does not change the shape. A scaling the plot of the surface energies just results in a rescaled γ-plot, which in turn produces a rescaled Wulff construction of the same shape. This means, that only the ratios of the surface energies matters, as opposed to the actual numerical values[7]. Another notable feature is, that the Wulff shape obeys the same symmetries as the underlying crystal, since that is the case for the γ-function. Another study notes that *"the equilibrium shape rarely contains faces with indexes higher than three"* [22].

[6]With a few additional assumptions of negligible contributions from edges, vertices and strain as explicitly stated later in section 5.

[7]We will exploit this feature later in section 4.4.5 when we attempt to deduce ratios of surface energy densities for e.g. ternary alloys from models of equilibrium shape evolutions.

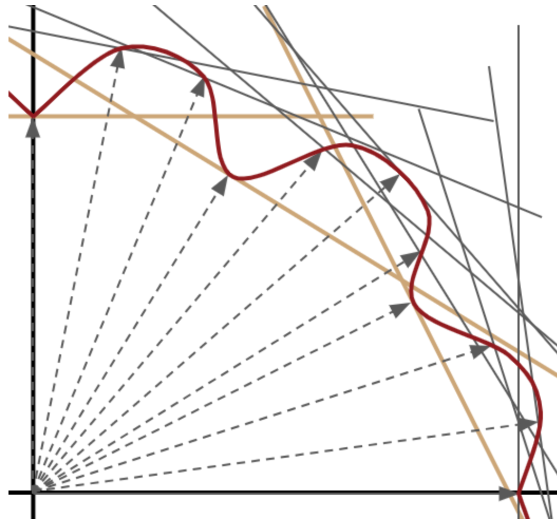

Figure 13: 2-dimensional example of Wulff construction from made up example of a γ-function (red). We will show the γ-functions for GaAs later in section 4.3. The dashed arrows show some selected radial vectors with normal planes drawn as solid lines at distance r. The gold colored planes show the Wulff shape after restriction of the IWS. Note that only the planes drawn in gold end up contributing to the final shape.

4.2 Surface Energy Densities from DFT

As seen in section 4.1, the surface energy densities (SED, proportional to the radial distance in figure 13) end up determining the Wulff shape. The SED values used for calculations of equilibrium shapes throughout this work are those for a $[1\bar{1}0]$ type GaAs NW displayed in table 1. These are obtained by Yeu et. al. (2019) [23] and Jenichen (2013) [24], based on first principles calculations (density functional theory, DFT) resulting in stability diagrams for different surface reconstructions. While numerous other studies have performed calculations of surface energy densities for GaAs and other III-V semiconductors [27, 28, 29], most of them do calculations of either an average surface or just one facet type. In contrast, the aforementioned study [23] is conducted for exactly the types of facets we need for $[1\bar{1}0]$ type NWs, and extensive work is done to include corrections and examine the role of both growth temperature and As pressure. While these additional T- and P-dependencies are interesting and important, they comprise an entire study in and of themselves. The interested reader should consult the source texts for additional details [23, 24]. We note two important facts: we can use calculated values for the surface energy densities, and these do show some dependence on both temperature and pressure.

Regarding the {112} facet type shown in table 1, we quote the conclusion, that *"For (112)A and B surfaces faceting into inverted-pyramidal depressions with (110), (111) and (113) facets is more stable than the plane reconstruction patterns"* [24]. In short, for GaAs the {112} facets are predicted to be energetically unstable. This is also reflected in

Label	Type	Angle	SED (γ)
GaAs			
t	{001}	0°	60 meV/Å^2
i	{113}A	25.24°	56 meV/Å^2
m^*	{112}A	35.26°	70 meV/Å^2
o	{111}A	54.74°	53 meV/Å^2
v	{110}	90°	51 meV/Å^2
r	{111}A	54.74°	53 meV/Å^2
InAs			
t	{001}	0°	48 meV/Å^2
i	{113}A	25.24°	44 meV/Å^2
$m^\dagger$	{112}A	35.26°	70 meV/Å^2
o	{111}A	54.74°	40 meV/Å^2
v	{110}	90°	40 meV/Å^2
r	{111}A	54.74°	40 meV/Å^2

Table 1: One set of surface energy densities for GaAs and InAs from Yeu et. al. (2019) [23]. The asterisk* denotes that the value for {112} facet type is obtained from Jenichen & Engler (2013) [24] and translated for comparison with those from Yeu et. al. (2019), since the methods of calculation differ, and Yeu et. al. (2019) does not include calculations for the {112} facet type. The translation is by linear interpolation from points of comparison. The dagger† denotes that no value was found, and this value was chosen to exclude facet m for InAs as in the case of GaAs. Angles are with respect to the (001) substrate indicated in e.g. figures 19 and 30. Values for GaAs are used in calculations of equilibrium shape evolutions throughout this work. Values depend on temperature and pressure.

the high SED value seen in table 1 and the resulting γ-plot excluding this facet in figure 14. The {112} facet type will nevertheless become relevant, when we explore qualitative fitting of SED ratios in section 4.4.5.

4.3 γ-plot for GaAs in the $[1\bar{1}0]$ Zone Axis

The previous section 4.1 shows how to obtain a size independent equilibrium crystal shape from surface energy densities associated with different crystal facets, and table 1 shows these values obtained from literature. From these inputs we can construct the γ-plot for GaAs to gain some insight into the expected faceting for this very studied binary alloy, to complement what we observe in experiments and read out from the stereographic projections.

The functional form of the γ-function (which is, in general 3-dimensional) can be described in terms of the angular coordinates θ and ω which together cover 4π [10]:

$$\gamma_{vs}(\theta,\omega) = \gamma_{vs0} - \sum_{hkl} c_{hkl} \frac{I_{hkl}}{1 + \left(\phi_{hkl}(\theta,\omega)/w_{hkl}\right)^2} \tag{12}$$

The hkl-index runs across all the high symmetry facets, the quantity γ_{vs0} denotes the maximum surface energy density, and I_{hkl} denotes the "dip" in intensity at facet hkl, that is: $I_{hkl} = \gamma_{vs0} - \gamma_{hkl}$. The quantity ϕ_{hkl} describes the angular distance to the high symmetry facet hkl, and w_{hkl} (not to be confused with the angular coordinate, ω) is the width of the dip around facet hkl. Since "dips" from several nearby high symmetry facets can overlap, the constant c_{hkl} can be adjusted from the default value close to unity to account for this. The values of γ_{vs0}, c_{hkl} and w_{hkl} are empirically adjustable parameters, which allow for visualization of the γ-function (see figure 14).

We will concern ourselves with the faceting of a NW viewed in cross section, and as such we only need a 2D slice of the 3D γ-function. We can simplify equation 12 to a 2-dimensional version, only dependent on the angle θ which now covers 2π:

$$\gamma(\theta) = \gamma_{max} - \sum_{hkl} c_{hkl} \frac{I_{hkl}}{1 + \left((\theta - \theta_{hkl})/w_{hkl}\right)^2} \tag{13}$$

The hkl-index runs the chosen facets (those displayed in table 1), which in principle neglects "dip" contributions from nearby angles outside our slice. This could be absorbed in the c_{hkl} parameter, but is to some extent desirable since the c_{hkl} parameter is meant to counteract overlapping "dips". The remaining quantities are as explained below equation 12. The angular distance $\phi_{hkl}(\theta, \omega)$ is now straight forwardly evaluated as $\theta - \theta_{hkl}$.

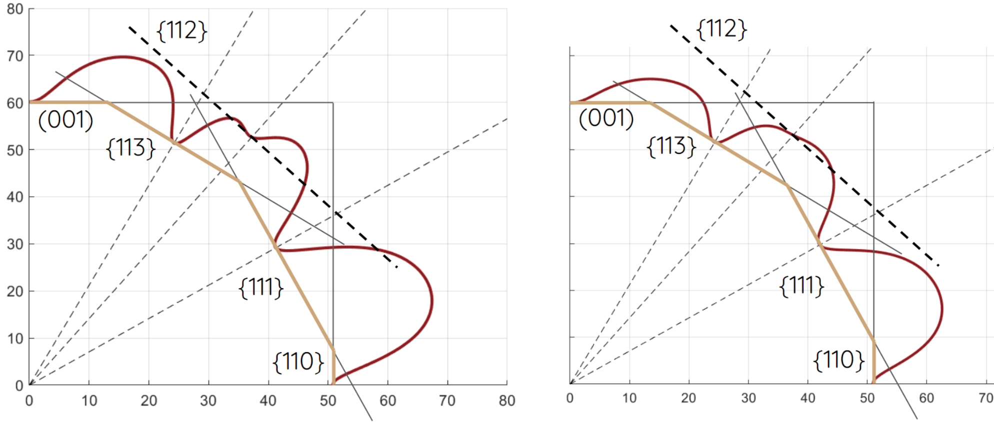

Figure 14: Example γ-plots for GaAs in the $[1\bar{1}0]$ zone axis, generated from the function in equation 13 with the hkl-indices running the facets shown in table 1. Two different examples are shown, since γ_{max} is variable, as well as the parameters c_{hkl} and w_{hkl}. The resulting Wulff shape is indicated in gold, and facets are labeled. Note that the $\{112\}$ facet is energetically unfavored but included for sake of completion, since this is sometimes observed in growths with e.g. surfactants. For relatively low values of γ_{max} (72 meV/Å^2, right figure) a cusp around the $\{112\}$ facet is barely present, and in any case this facet is excluded from the final Wulff shape due to the high associated SED. Units are meV/Å^2 but unimportant for the shape.

We can now plot the angular dependence of the γ-function in cartesian coordinates,

in a manner similar to that seen in figure 13. The result is shown in figure 14. With the basic Wulff construction and experimental observations showing the available facets, we are now ready to apply the principles of Wulff construction for our case of $[1\bar{1}0]$ type SAG NWs.

4.4 Constrained Wulff Shaping (CWS)

We have shown how Wulff construction results in a Wulff shape for a "free floating" crystal[8]. However, in our case the NW crystal shape is grown on a masked substrate, and is thus subject to a lithographic constraint, which is the mask opening. Just like the Wulff shaping minimizes surface energy, the guiding principle for CWS is surface energy minimization, now under constraints. Note that the equilibrium shape in CWS can no longer be independent of volume, since the crystal can no longer scale freely to accomodate a change in volume; the part of the crystal bound to the trench has the trench width as a set dimension.

Our SAG NW model is assumed 1-dimensional, that is, it shows translational symmetry along the $[1\bar{1}0]$ axis of the NW (see section 3.2). As a consequence, we can examine volume by considerations of cross sectional area, specifically the cross sectional 2-dimensional Wulff shape of the NW grown in a trench. We will use "volume" and "area" interchangably where there is no risk of confusion. The width of the NW is initially fixed to the width of the mask opening. We will assume homoepitaxial growth throughout, so there are no complications due to strain arising from lattice mismatch.

Figure 15 (top) shows the initial condition for CWS. At the beginning of MBE growth, the NW trench is "empty", and the trench fills up layer-by-layer during the first stages of growth. Once the trench is filled, the crystal volume available for CWS can be viewed as that which exceeds the flat filled trench as shown in figure 15 (bottom). The point of our investigation is now the shape of this additional volume displayed in gold.

Sticking with the principles for Wulff construction outlined in section 4.1 above, the equilibrium shape for a given volume or cross sectional area will now be that, which minimizes the surface energy. Note that the boundary marked by the dashed line in figure 13 bottom has no surface energy contribution, since the boundary is merely a marker for our convenience; the dashed line is inside a homoepitaxial "bulk". In other words, much of the crystal shape is already determined; only the additional volume in figure 15 undergoes equilibrium shaping while maintaining the bulk boundary towards the part already grown in the NW trench.

4.4.1 3-facet Equilibrium NW Model

For reasons outlined earlier in section 4 we consider only the facets listed in table 1. To start with a simple model, we restrict ourselves to a choice of 3 facet types. It turns out

[8] "Free floating" means with all surfaces being towards the same type and phase of material. The values quoted in table 1 are for surfaces in an environment with a certain As pressure. However, the method would apply equally well to a crystal forming in e.g. a liquid solution, given surface energy densities calculated for this type of liquid environment.

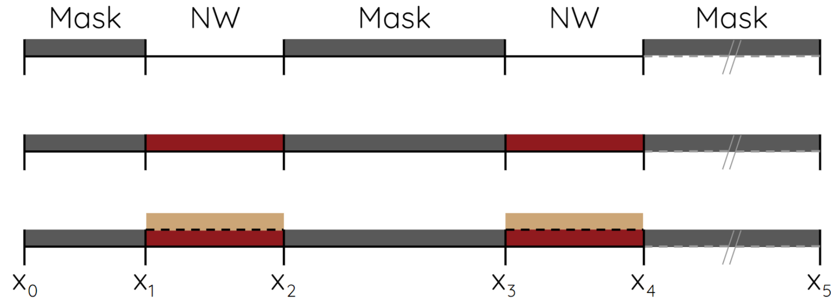

Figure 15: **Top:** Mask displayed in grey, no growth in trenches at the very beginning. **Mid:** The NW trenches fill up, here shown leaving a flat surface (red). **Bottom:** Once the trench is filled, any additional volume (gold) must be distributed by CWS, since growth on mask is not allowed by selectivity. Regardless of whether the trench initially fills up flat or not, the interesting volume for CWS becomes that which exceeds the filled trench: the volume displayed in gold. Note that both domains red and gold consist of the same NW material. For our purposes the zone axis is $[1\bar{1}0]$, but similar considerations would be valid for any other NW direction assuming translational symmetry.

that this simple model can be solved analytically for the minimum surface energy.

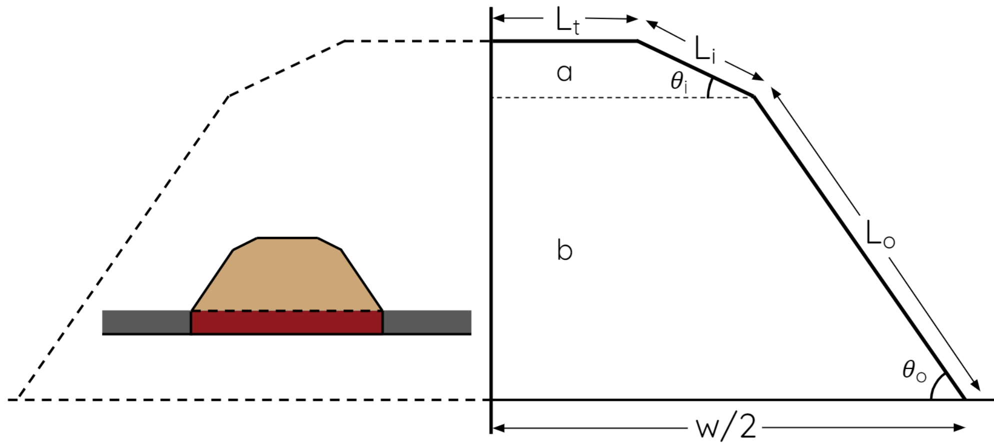

Figure 16: Schematic cross section of a $[1\bar{1}0]$ type NW with {001}, {113} and {111} facets labeled t, i and o, respectively. The figure is conceptual, as the facet lengths will vary, depending on width, crystal volume and surface energy densities. Subscripts are kept general, but shown angles correspond to those of the chosen facets. Note that the convex requirement for the Wulff shape fixes the order of the facets: facet angles increase moving from the symmetry plane (middle) towards the outside (right): $\theta_i < \theta_o$. Insert shows NW cross section in partial schematic from figure 15 for clarity.

While figure 16 shows only dimensions for one half of a NW cross section (assuming a bulk lower boundary towards the substrate), the vertical symmetry plane means that

all facet lengths and the cross sectional area just doubles for the full cross section (see equations 14, 15 and 16 below). Thus finding the equilibrium shape for this half model corresponds to the equilibrium shape for the full cross section of a single NW through symmetry. From the schematic in figure 16 we can proceed analytically as follows:

1. Three facet types translates to three degrees of freedom.
2. Eliminate one degree of freedom by expressing the cross sectional area of the NW in terms of the lengths of the facets (equation 14).
3. Eliminate another degree of freedom by expressing the width of lower bulk boundary in terms of the length of the facets (equation 15).
4. Express the surface energy in terms of the last remaining degree of freedom and minimize by setting the derivative with respect to the last degree of freedom equal to zero.
5. This yields the value for one degree of freedom at minimum energy. Equations 14 and 15 yield the remaining two.

Expressing the area of the half cross section in figure 16 is straight forward:

$$\begin{aligned} A_{half} &= \frac{1}{2}\Big[L_t + L_t + L_i\cos(\theta_i)\Big]L_i\sin(\theta_i) \\ &\quad + \frac{1}{2}\Big[L_t + L_i\cos(\theta_i) + L_t + L_i\cos(\theta_i) + L_o\cos(\theta_o)\Big]L_o\sin(\theta_o) \end{aligned} \tag{14}$$

where the terms are in order of areas labeled a and b in figure 16. Expressing the half width:

$$w/2 = L_t + L_i\cos(\theta_i) + L_o\cos(\theta_o) \tag{15}$$

The (half) surface energy associated with figure 16 is:

$$E_{half} = L_x\Big[\gamma_t L_t + \gamma_i L_i + \gamma_o L_o\Big] \tag{16}$$

with γ_k being the surface energy density for facet $k \in \{t, i, o\}$ in figure 16, and L_x is the NW length. The surface energy densities in equation 16 (proportional to the γ-function from section 4.1) can be varied for a qualitative match to an observed NW cross section, or they can be fixed from e.g. DFT calculations for predictive analysis. The CWS results presented in this section and sections 4.4.2 and 4.4.3 are obtained from the values presented in table 1.

Through elimination of variables, the equations for facet lengths expressed in terms of each other, total area and constrained width become quite long. The same goes for the subsequent minimization of surface energy, all of which is best treated with a symbolic

solver. The exact equations are less important than their general form and the fact that they can be solved symbolically. The equations have 2nd order polynomial components (as evident from equation 14), which produce both negative and imaginary solutions for facet lengths. Under any circumstances the solutions can be grouped into self-consistent sets, which can be sorted to keep the facets lengths real and positive. The curious reader with too much spare time can examine these analytic solutions in the appendix section 8.3.

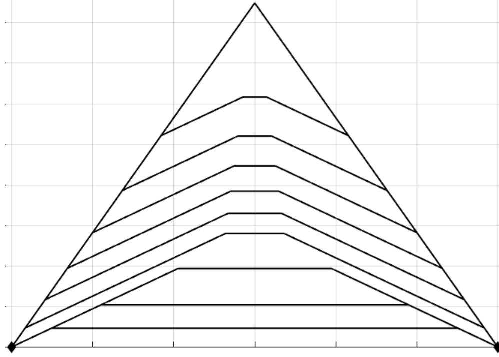

Figure 17: The cross sectional, simplified shape evolution of a homoepitaxial GaAs $[1\bar{1}0]$ type NW from CWS in steps of 10% of "full" volume, with "full" volume being the maximum size of the crystal under the constraint on width and on available facets. This figure is produced with analytic minima to the surface energy function as outlined in section 4.4.1 and solved for in the appendix section 8.3. The surface energy densities are shown in table 1, obtained from another DFT study of the allowed GaAs facets [23]. The final triangular cross section marks the "full" volume, which is also the transition between regimes 1 and 2. Black diamonds along the bottom mark the lithographic constraint imposed by the trench width.

This analytic solution can be evaluated for a fixed width and a varying set of volumes to produce a visualization of the shape evolution of the NW as function of volume. Figure 17 shows the shape evolution of the CWS under the given constraint on bottom width of the NW and the allowed facets in set steps of volume. The final shape is just the maximum crystal volume (or equivalently cross sectional area) that can be accommodated with the available facets and a constrained width, in this case a fully {111}-faceted NW. In general we will denote the cross sectional area of a fully {111}-faceted morphology on a (001) substrate as the "full" area:

$$V_{full} \propto A_{full} \equiv \frac{w^2}{4}\tan(\theta) \simeq 0.3536w^2 \tag{17}$$

where w is the width of the NW trench and θ is the angle of the {111} planes relative to the (001) substrate.

We label the stage of the crystal growth shown in figure 17 as "regime 1". This raises the obvious question: how do we conduct a similar analysis in the case of overgrowth,

when the crystal has to accommodate more volume than what is possible with this configuration?

4.4.2 4-facet Equilibrium NW Model

If we want to allow for overgrowing additional volume ("regime 2"), we need to include another type of facet in the model. We could allow for overgrowth by breaking the constraint on the bottom width in cases of a volume exceeding the maximum allowed. However, this would mean crystal growth on the mask region next to the NW trench, which we have restricted by selectivity as described in section 2.1[9].

Instead we can include another facet of a type which already exists due to crystal symmetry, and which allows for unlimited growth: The NW schematic in figure 18 includes another {111} type facet, still obeying the crystal symmetry and the translational symmetry of the NW. Note that the angles and surface energies of the "new" facets (labeled r) are equal to those of the other {111} facet (labeled o). While the bottom width is still contrained to the width of the trench, the crystal can now grow to arbitrary size.

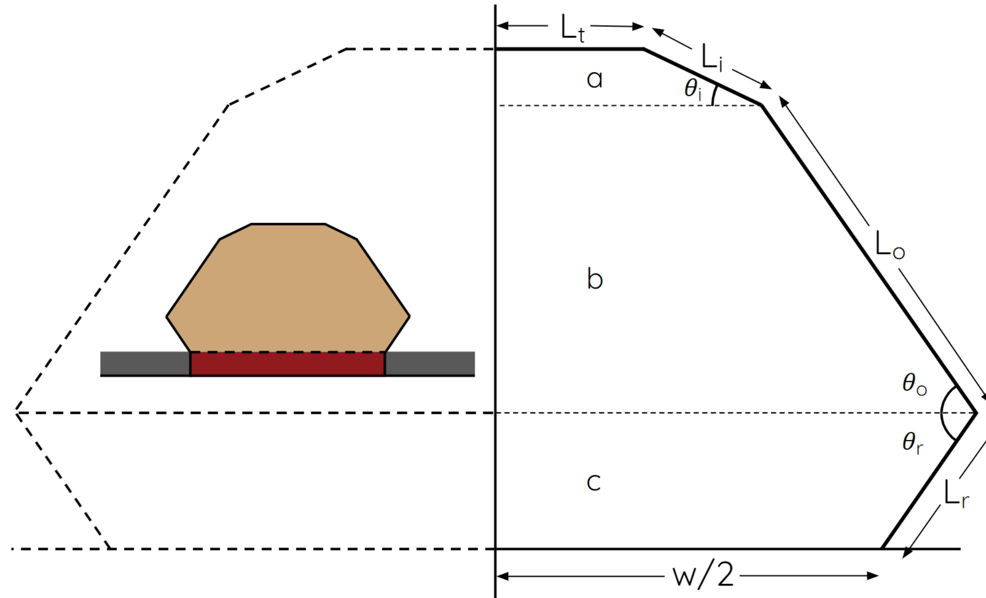

Figure 18: Schematic cross section of $[1\bar{1}0]$ type NW with {001}, {113}, {111} and {111} facets labeled t, i, o and r, respectively, now allowing for overgrowth. Insert shows NW cross section in partial schematic from figure 15 for clarity. Since only the bottom width is fixed lithographically, the crystal can now grow to arbitrary size. Note that $\theta_r = \theta_o$ and $\gamma_r = \gamma_o$ due to the symmetries of the crystal viewed in the $[1\bar{1}0]$ zone axis. The order of the facets is still fixed due to the requirement of a convex shape.

The additional facet introduces an additional degree of freedom in the system, and

[9] In actual NW growth we sometimes do see growth on the mask next to the NW trench. For now we will keep the model simple and include additional volume by means of additional facets.

the procedure outlined by bullet points in section 4.4.1 compounds in complexity, since eliminating two variables still leaves us with a parameter space of the remaining two and no guarantee that the derivative of the surface energy function with respect to any of the facets lengths will be zero for a real and positive value. We note that the analytic solutions for the 3-facet case are already quite lengthy (see appendix section 8.3), and another method is desirable.

We can minimize the surface energy by a numerical solver instead of by analytic expressions. Our choice of solver is the `'fmincon'`[10], again from MATLAB [16] (for code see appendix sections 8.4.3 and 8.4.4), which exactly minimizes a multivariable function under a set of constraints. Once again we will refrain from a further examination of the numerical solver and merely utilize it as a tool. However, the solver can in principle be used for more general models. The only requirements are the ability to express the area and constraints in terms of the facet lengths and known quantities. We shall utilize this below and skip directly to a model with one (and subsequently two) additional facet(s).

4.4.3 5-facet Equilibrium NW Model

Using a numerical solver makes e.g. the addition of a "vertical" {110} facet (see figure 19) as trivial as adjusting a few lines of code, compared to compounding complexity if we were to seek an analytic solution.

With the morphology in figure 19, we adjust our expression for the half area:

$$\begin{aligned} A_{half} =& \frac{1}{2}\Big[L_t + L_t + L_i\cos(\theta_i)\Big]L_i\sin(\theta_i) \\ &+ \frac{1}{2}\Big[L_t + L_i\cos(\theta_i) + L_t + L_i\cos(\theta_i) + L_o\cos(\theta_o)\Big]L_o\sin(\theta_o) \\ &+ \Big[w_{half} + L_r\cos(\theta_o)\Big]L_v \\ &+ \frac{1}{2}\Big[w_{half} + w_{half} + L_r\cos(\theta_o)\Big]L_r\sin(\theta_r) \end{aligned} \tag{18}$$

The half width is given as:

$$w/2 = L_t + L_i\cos(\theta_i) + L_o\cos(\theta_o) - L_r\cos(\theta_r) \tag{19}$$

The energy function is:

$$E_{half} = L_x\sum_k \gamma_k L_k \tag{20}$$

where the k-indices now run all the chosen facets: $k \in \{t, i, o, v, r\}$.

Using `'fmincon'` we minimize the energy function in equation 20 under the constraints given by equations 18 and 19, and additionally require all facet lenghts to be

[10] Documentation for `'fmincon'`: https://www.mathworks.com/help/optim/ug/fmincon.html

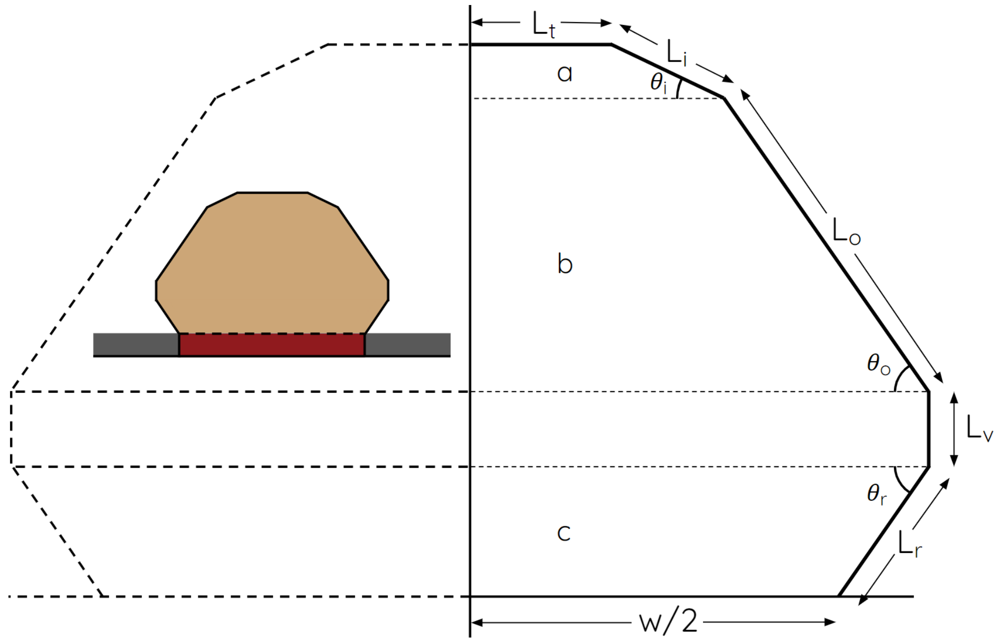

Figure 19: Schematic cross section of $[1\bar{1}0]$ type NW with {001}, {113}, {111}, {110} and {111} facets labeled t, i, o, v and r, respectively, allowing overgrowth and a vertical facet. Insert shows NW cross section in partial schematic from figure 15 for clarity. Once again the order of the facets is fixed for a convex shape. The convexity only pertains to the non-constrained part.

real and positive (or zero)[11]. Once again we can vary volume for a fixed width. Figure 20 shows the shape evolution of the CWS under the given constraint on bottom width of the NW, but this time with facets allowing for overgrowth and solved numerically with `'fmincon'`.

Comparing figures 17 and 20, we see that for the chosen set of surface energy densities, the crystal grows almost without utilizing the "overgrowth"-facets (labeled v and r in figure 19), at least until near full volume is reached. It is not surprising, that the 5-facet model with option for overgrowth employs the additional degree of freedom before growing the full volume into a peak shape like in figure 17. As the growth approaches the peak, very little volume is added by paying the energetic cost of elongating the outer {111} facets (labeled o). At some point more volume can be added by growing another small {110} facet (labeled v) and adding a thin layer on the outside of the shape instead. The predicted equilibrium shape evolution is compared to experimental observations in section 4.4.5.

Varying the surface energy densities for different facets and rerunning the shape evolution shows some trends. Since the guiding principle of CWS is surface energy

[11] The code includes an additional {112} facet labeled m for generality as explained in section 4.4.4 below.

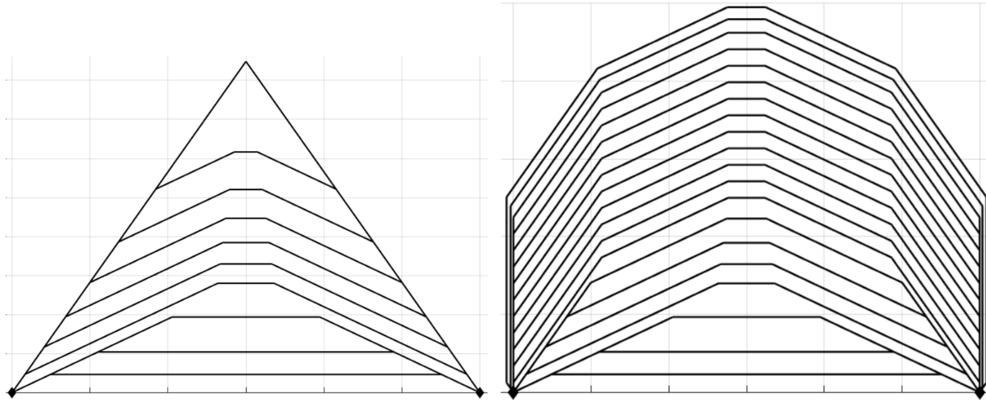

Figure 20: **Left:** Figure 17 shown here for comparison. **Right:** The cross sectional shape evolution of a homoepitaxial GaAs $[1\bar{1}0]$ type NW from CWS in steps of 10% up to 200% of "full" volume. The crystal overgrows and surpasses the original constraint on volume. The surface energy densities are shown in table 1, obtained from another DFT study of the allowed GaAs facets [23] and equal to those used in the 3-facet model shown in figure 17. Note that the models show similar shapes for the first $\sim 70\%$ of "full" volume. Black diamonds along the bottom mark the lithographic constraint imposed by the trench width. Note that the SED values in table 1 are dependent on temperature and pressure, and subsequently the equilibrium shapes are as well.

minimization, the general trend shows rapid elimination of a given facet with increasing surface energy density for said facet. As outlined in section 4.1 the studies additionally show, that in the case of equal surface energy densities for different facets, the facet with lower Miller indices is more prevalent. Generally the CWS simulation is able to reproduce the faceting observed experimentally.

Finally a few tweaks to the model would let us model another NW direction, e.g. [100]. Notably the bulk FCC in [100] zone axis shows different symmetries from $[1\bar{1}0]$, which is to be taken into account (see stereographic projection for [100] in the appendix section 8.2).

Our ability to construct plots of time evolution of equilibrium faceting like the one in figure 20 from essentially only a stereographic projection and ratios of SEDs hints at the possibility of "reverse engineering": deducing SED ratios from qualitative matching of predicted shapes to those observed in experiments - assuming equilibrium shapes during growth. This could prove valuable as an alternative to involved DFT calculations, which would be very complicated for e.g. different surface reconstructions of ternary alloys. This should of course be exercised with caution, and has some limitations. We discuss this in section 4.4.5.

4.4.4 6-facet Equilibrium NW Model

As a small addition, we include a {112} type facet labeled m in our model, since this sometimes shows up in growths, e.g. GaAs grown with Sb surfactant, denoted GaAs(Sb). We will only show an updated schematic of the facets, and update equations for the half area and half width. The energy function is unchanged except for the inclusion of the new m facet in the k-indices.

Note that for e.g. pure GaAs, the SED associated with this type m facet is so high, that it is excluded from the Wulff constructions as shown in section 4.3. In this case the length of facet m is just found to be zero from the numerical solver. We include this facet for generality, since it is used for qualitative fitting for GaAs(Sb) buffers in section 4.4.5. The general solvers provided in the appendix sections 8.4.3, 8.4.4 and 4.4.1 include this {112} type facet m.

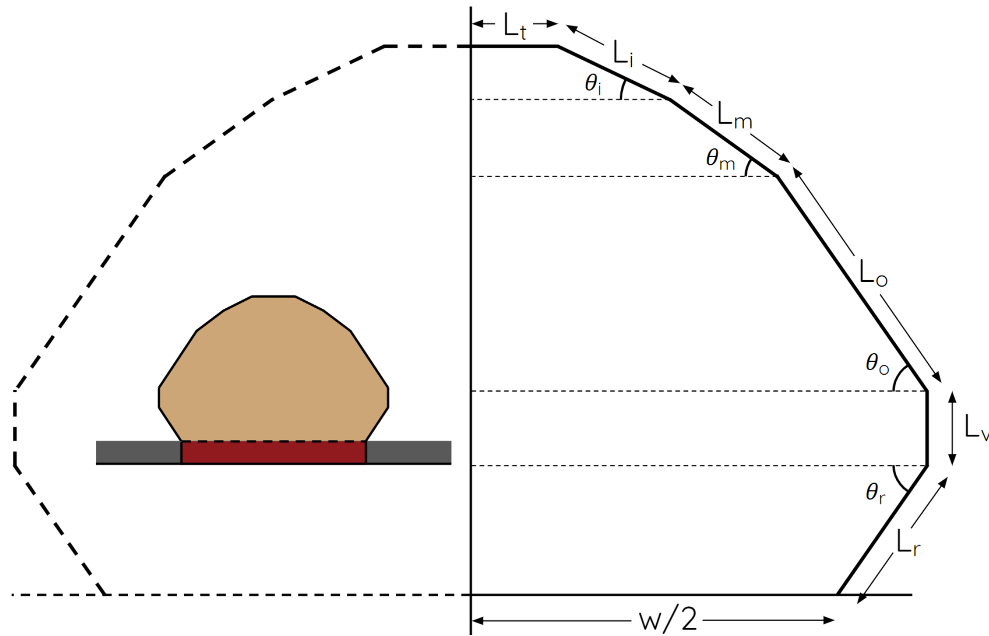

Figure 21: Schematic cross section of $[1\bar{1}0]$ type NW with {001}, {113}, {112}, {111}, {110} and {111} facets labeled t, i, m, o, v and r, respectively. Insert shows NW cross section in partial schematic from figure 15 for clarity. Once again the order of the facets is fixed for a convex shape. The convexity only pertains to the non-constrained part.

With the morphology in figure 19, we adjust our expression for the half area:

$$
\begin{aligned}
A_{half} = &\frac{1}{2}\Big[2L_t + L_i\cos(\theta_i)\Big]L_i\sin(\theta_i) \\
&+ \frac{1}{2}\Big[2L_t + 2L_i\cos(\theta_i) + L_m\cos(\theta_m)\Big]L_m\sin(\theta_m) \\
&+ \frac{1}{2}\Big[2L_t + 2L_i\cos(\theta_i) + 2L_m\cos(\theta_m) + L_o\cos(\theta_o)\Big]L_o\sin(\theta_o) \\
&+ \Big[w_{half} + L_r\cos(\theta_o)\Big]L_v \\
&+ \frac{1}{2}\Big[2w_{half} + L_r\cos(\theta_o)\Big]L_r\sin(\theta_r)
\end{aligned} \tag{21}
$$

And the expression for the half width now becomes (compare to equation 19):

$$
w/2 = L_t + L_i\cos(\theta_i) + L_m\cos(\theta_m) + L_o\cos(\theta_o) - L_r\cos(\theta_r) \tag{22}
$$

Both of these adjustments are, as mentioned in section 4.4.2 merely adjustments to a few lines of code. Both of these updates are included in the codes provided in the appendix sections 8.4.3 and 8.4.4.

4.4.5 CWS Fitting of Equilibrium Shapes

In this section we will tentatively explore qualitative fitting of equilibrium shapes predicted by CWS to experimental observations - assuming that the observed shapes represent equilibrium. First we will present results for the case of GaAs.

Figure 20 shows our prediction for the equilibrium shape evolution of a homoepitaxial $[1\bar{1}0]$ type GaAs NW grown without use of surfactants, based on the SED values listed in table 1. A similar prediction for InAs is shown in figure 22 with the GaAs prediction for comparison. The two predictions look roughly similar, with the InAs version showing a smaller top facet.

Since these predictions show a wide range of time steps, they can be compared with shapes observed in growths across a wide range of volumes. Note that the SED values in table 1 are dependent on temperature and pressure, and subsequently the equilibrium shapes are as well.

An example comparison with AFM data from experiment is shown in figure 23, with arrows highlighting an interesting discrepancy between the model and the observation. The discrepancy consists mainly of the regions on the outside of the $\{113\}$ facets marked by arrows, where the model predicts continuation of growth by elongation of $\{111\}$ facets. The four different AFM scans shows different stages of growth due to a change in pitch (which effectively cause a change in growth rate, see section 3.3), and the emergence of the less defined region on the outside of the $\{113\}$ facets is apparently accompanied by a variety of angles. We note that any given facet should have a fixed angle, purely dictated by crystallography.

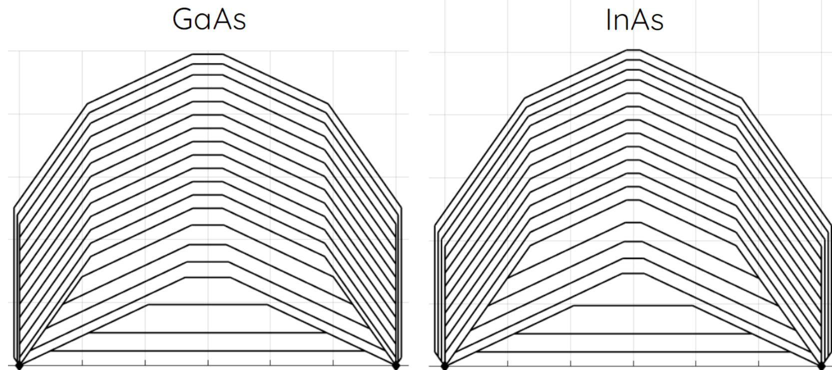

Figure 22: Side by side comparison of GaAs and InAs equilibrium cross sectional shape evolutions for homoepitaxial $[1\bar{1}0]$ type NWs with SEDs shown in table 1. Both predictions are dependent on growth conditions such as temperature and pressure.

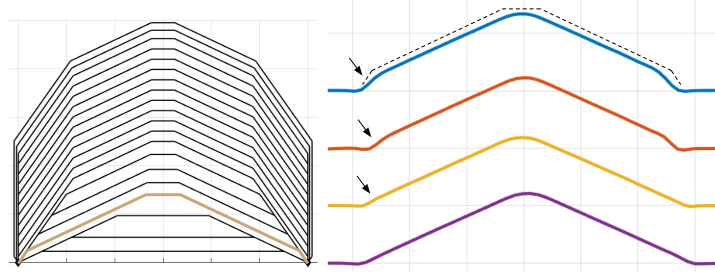

Figure 23: **Left:** Equilibrium cross sectional shape evolution of GaAs values in table 1 with growth stage marked at 40% of "full". Note the beginning growth of {111} facets in the model at the marker. **Right:** Colored lines show data from experiment obtained by atomic force microscopy (AFM) line scans of four GaAs buffers on GaAs (001) substrate from MQML091. The four buffers have different pitches in the range $0.5 - 2.0\mu\text{m}$, which results in different incorporation rates as shown in sections 3.3 and 8.1.2 and thus slightly different stages of growth. Each plot is averaged over 80 lines, and dashed lines show the 40% of "full" GaAs shape from left panel, offset for comparison. Arrows indicate discrepancies. From visual inspection it is obvious, that the morphology on the outside of the {113} facets does not match the expected. Growths by Daria Beznasyuk, AFM data by Anna Wulff Christensen.

This discrepancy could in part be caused by our data treatment, where each AFM plot is averaged over 80 line scans. Each line scan could show more well defined facets, but small variations between line scans could create features in the overall average. This is shown conceptually for the initial formation of {111} planes in a fully {113} faceted NW in figure 24. We see that the averaging produces a smearing of the outer {113} facet boundary, and different distributions for averaging produces a variety of angles. This indeterminable region does, however, seem to also show up in some single line scans.

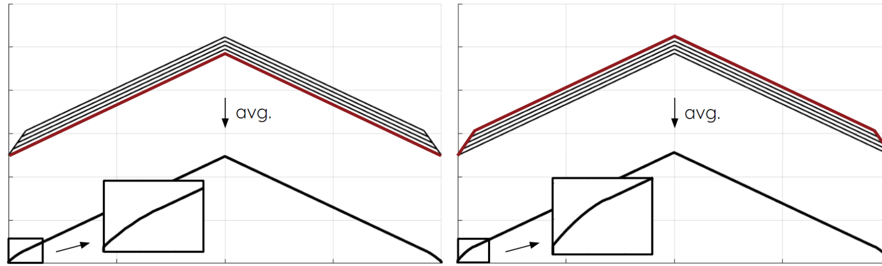

Figure 24: **Top row:** Artificially generated data for fully {113} faceted NW, transitioning to growth by elongation of {111} facets. Red lines indicate more entries of either lower (left) or higher (right) cross sectional areas. **Bottom row:** Corresponding averages produced by "lower" and "higher" distributions. Different distributions produce a "smearing" of the outer boundary of {113} planes, a region with a less defined faceting, and a different angles in the resulting region.

Another possible explanation is the decomposition of {112} facets mentioned in section 4.2 [24]. What looks somewhat similar to {112} facets in AFM could be alternating depressions of {111} and {113} facets as shown in figure 25. This could also explain the apparent range of angles shown in figure 23, since a decomposition could consist of segments of varying length and thus a variation of angles. In short the observed morphology could be a less clearly faceted part of the morphology. We note that alternating depressions of {111} and {113} facets break the assumption of a convex CWS for an equilibrium shape. Additional experiments are desirable if we want to examine this transition further.

If we turn our attention away from pure GaAs, examples such as GaAs with Sb surfactant, GaAs(Sb) as well as the ternary InGaAs show some promise for use in buffers for NW growths. The addition of Sb and In complicates calculations of SEDs from DFT. With the CWS method established above we can attempt to qualitatively fit observed shapes to a set of SED ratios. This method can be directly generalized for equilibrium shapes across different materials, substrates and NW orientations.

The procedure of finding SED ratios from fitting rather than predicting equilibrium shapes from DFT calculations suffers from a few noticable drawbacks. Nevertheless we can attempt to examine the ratios as shown in figure 26, which shows the result of the estimated SED values listed in table 2. With CWS fitting of equilibrium shapes we are able to approximately reproduce the shape of the GaAs(Sb) buffer as well as the InGaAs section shown in figure 26, which tentatively suggests approximately correct ratios of estimated SEDs. This concludes the example of CWS fitting of equilibrium shapes, and once again additional experiments are desirable.

1. The procedure is largely qualitative, as the fits are currently conducted visually. This could probably be improved by a more rigorous fitting procedure.

2. Growths with relatively low volumes often do not employ all facets, and some values are therefore irrelevant when fitting to some shapes.

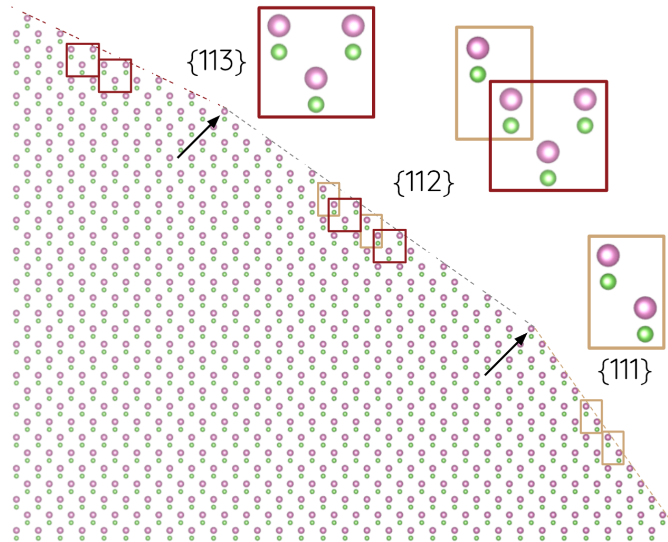

Figure 25: {112} facets shown along with {111} and {113} with arrows marking boundaries between planes. Boxes indicate base sections of the given facets with group III (Ga) in purple and group V (As) in green. Facets are shown as A-variants with group III termination. Composite boxes on {112} show the decomposition of a {112} base section into part {111} and part {113} base sections. For the fixed angle expected for {112} ($\theta_m = 35.26°$) the reconstruction could look like the composite shown here [24]. Longer or shorter {111} and {113} segments would give rise to angle variations. Figure produced with VESTA [25].

3. The shapes are not guaranteed to be unique. In other words, several sets of ratios could in principle produce similar shapes, at least within a certain range of volumes.

4. Since the shapes only rely on ratios, the actual values are out of reach for this method, unless some of the values are known. The actual values may be important for studies of driving forces (see section 5).

5. As soon as the growth is no longer homoepitaxial, we expect an energy term from strain due to lattice mismatch (see equation 24 in section 5). This will affect the minimization of free energy, unless the contribution is negligible.

6. The method relies on surface energy minimization, and as such all predicted shapes are equilibrium shapes. If kinetics play a large role, this method will not be suitable for estimating SED ratios.

7. The version of shape evolution presented in this work assumes growth from a flat trench. Growth on top of an existing buffer could proceed differently, because the buffer to transport channel interface is associated with an interface energy, and because strain considerations could be substantial in heterostructures. Further examination is left for future work.

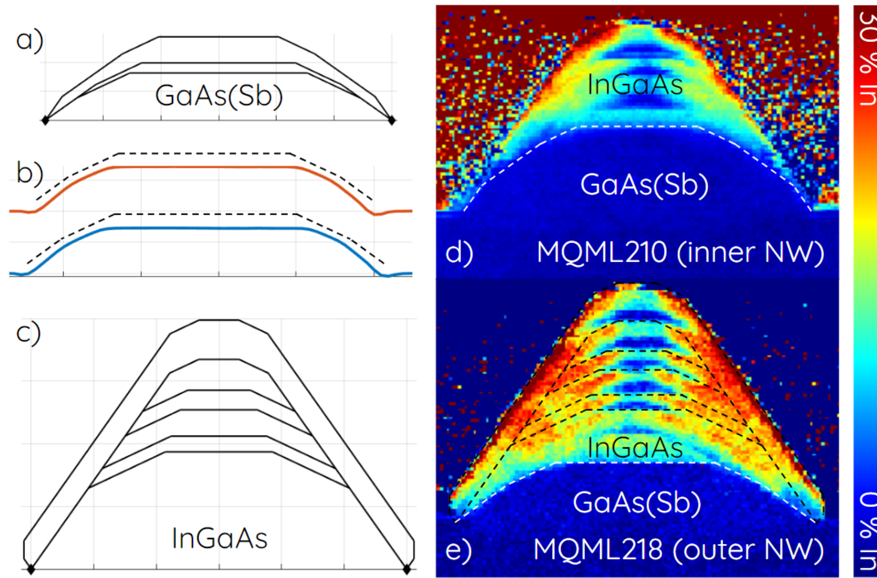

Figure 26: **a)** Equilibrium shape evolution of GaAs(Sb) from qualitatively fit values estimated in table 2 with three different growth stages marked at 30%, 35% and 50% of "full". **b)** Colored lines show AFM data of two GaAs(Sb) buffers on GaAs (001) substrate from MQML014. Each plot is averaged over 80 lines, and dashed lines show the 30% of "full" GaAs(Sb) shape from panel a offset for comparison. **c)** Another set of SED values shown in table 2 produces a possible shape evolution for InGaAs with select growth stages shown for use in panel e. **d)** and **e)** EELS images show material compositions for MQML210 and MQML218. Both growths are GaAs (001) substrates with identical GaAs(Sb) buffer growth conditions and subsequently four and seven layers of InGaAs with GaAs markers between (with three and six GaAs markers, respectively). For MQML210 an inner NW is shown, while an outer NW is shown for MQML218. The difference in growth rates between inner and outer NWs (see section 3.3) is clearly seen with two different stages of buffer growth. White dashed lines show 50% (MQML210, inner NW) and 35% (MQML218, outer NW) of "full" GaAs(Sb) buffer from panel a. Black dashed lines show the shape evolution from panel c superimposed on MQML218, which implies the assumption that growth on the existing GaAs(Sb) buffer evolves as if grown from a flat trench. Growths by Daria Beznasyuk, AFM data by Anna Wulff Christensen, images by Sara Martí-Sánchez and Jordi Arbiol.

This concludes our investigation of CWS for predicting morphology. The remainder of this thesis will explore crystal growth driving forces by changes in chemical potentials during growth.

Label	Type	Angle	SED (γ)
GaAs(Sb)			
t	{001}	0°	44 meV/Å^2
i	{113}A	25.24°	46 meV/Å^2
m	{112}A	35.26°	46 meV/Å^2
o	{111}A	54.74°	48 meV/Å^2
v	{110}	90°	66 meV/Å^2
r	{111}A	54.74°	48 meV/Å^2
InGaAs			
t	{001}	0°	60 meV/Å^2
i	{113}A	25.24°	56.5 meV/Å^2
m	{112}A	35.26°	54 meV/Å^2
o	{111}A	54.74°	43 meV/Å^2
v	{110}	90°	51 meV/Å^2
r	{111}A	54.74°	43 meV/Å^2

Table 2: Surface energy density estimates for GaAs(Sb) and InGaAs from qualitative fitting of model shapes to experimental observations. Note that the fitting relies only on ratios, and that values are tentative. Some values (e.g. for GaAs(Sb) {110} and {111} types) are much less impactful, since they are just high enough that the associated facet does not appear in shapes as shown in figure 26. We remark that the fit shape evolution for InGaAs compares shape evolution from a flat trench (model) to growth on an existing GaAs(Sb) buffer (experiment) directly.

5 Crystal Growth Driving Forces

This section follows the formalism laid out by Krogstrup et al. (2015) [26] for growth kinetics, here applied to a SAG structure with a generalized faceting.

In the previous section 4.4 we investigated the driving force for the crystal shaping: the minimization of surface energies. The driving force for the crystal growth, the transition from adatom to crystal phase is the difference in chemical potentials between the phases. The adatom phase is often called the 'mother phase' and the crystal phase the 'daughter phase', since the latter derives from the former:

$$\Delta\mu_{as} = \delta\mu_a - \delta\mu_s \tag{23}$$

In general both the terms on the right hand side are dependent on both materials and existing facets, as well as growth conditions such as temperatures and fluxes. We can evaluate the term $\delta\mu_s$ as the excess chemical potential relative to a bulk, which is just a surface excess. For the general framework we let X be a set of independent parameters, which fully describe the crystal shape (see examples in sections 5.1 and 5.2). The chemical potential associated with the incorporation of an additional III-V pair of crystal volume into the solid phase is via change in the specific parameter X_β then [26]:

$$\delta\mu_{X_b} = \sum_\alpha \gamma_\alpha \frac{\partial A_\alpha}{\partial X_\beta}\frac{\partial X_\beta}{\partial N} + \delta\mu_b + \delta\varepsilon \tag{24}$$

In equation 24 the first sum-term is a surface energy contribution, γ_α is the surface energy density associated with a surface of type (facet) α, A_α is the surface area of that facet, and N is the number of III-V pairs in the crystal volume (4 pairs per unit cell). The second term, $\delta\mu_b$ is the chemical potential associated with the bulk crystal phase, and the third term $\delta\varepsilon$ is an energy contribution due to strain. For completeness we should include contributions from edges and vertices but we will ignore them since they are one and two dimensions smaller than the surface contribution, at least for crystals of a certain size[12]. Since the bulk contribution will be the same for any shape of the same volume, and we assume the strain contribution to be negligible (at least in homoepitaxial growth), different crystal shapes will differ only in terms of their surface energies described by the first term:

$$\delta\mu_{s,X_b} = \sum_\alpha \gamma_\alpha \frac{\partial A_\alpha}{\partial X_\beta}\frac{\partial X_\beta}{\partial N} \tag{25}$$

The additional s-subscript denotes that we are describing just the surface energy contribution. The excess chemical potential in equation 25 denotes a change to the Gibbs free energy of a generalized state like the ones described back in section 2.2, illustrated in figure 3. From equations 2, 3, 4 and 5 it is obvious, that a change in chemical potential associated with growth on different parts of the crystal impacts the transition rates. After section 5.2 we will be able to quantify this impact.

As an example we will first describe a simple case with a single parameter X_β fully parametrizing growth, and a sufficiently simple crystal shape which follows. We will again assume translational symmetry along the $[1\bar{1}0]$ NW axis.

5.1 3-facet Chemical Potential Model

The simple model allowing for easy parametrization of growth is shown in figure 27. We initially consider growth in regime 1, that is before overgrowth, and assume for the crystal growth to only proceed by increasing h_1, until the cross sectional shape is a full triangle. While this behaviour is not expected in an actual physical system, it serves as a simple example. We will turn our attention to a system with a closer resemblance to an actual growth system in section 5.2.

From figure 27 we express the relevant quantities in terms of our constraint w and the parameter h with L_x being the NW length:

$$L_o = h_1/\sin(\theta) \tag{26}$$

[12]The edge contribution could be significant for very small systems such as ours. In the following we will assume that this is negligible, and leave further examination of edge energy contributions for future work. Note also, that vertices are non-existent in the case of translational symmetry.

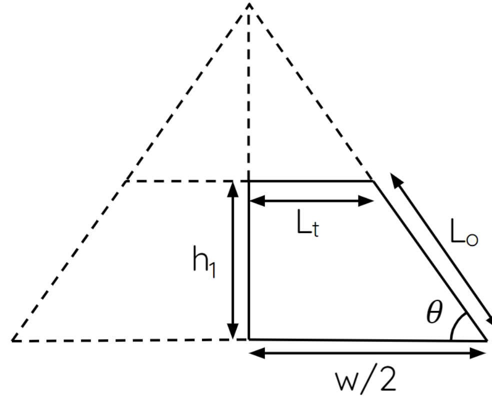

Figure 27: Schematic of NW with flat [001] top facet and {111} side facets, the stage of growth labeled regime 1 (before overgrowth). The growth proceeds increasing h_1, until L_t is eliminated and the cross section is a full triangle at $h_1 = w\tan(\theta)$. All quantities are kept in terms of the right side half of the NW.

$$L_t = (w/2) - \cos(\theta)L_o = (w/2) - \cot(\theta)h_1 \tag{27}$$

$$A_o = L_x L_o = L_x h_1/\sin(\theta) \tag{28}$$

$$A_t = L_x\Big[(w/2) - \cot(\theta)h_1\Big] \tag{29}$$

Equations 28 and 29 let us determine the derivatives:

$$\frac{\partial A_o}{\partial h_1} = L_x/\sin(\theta) \tag{30}$$

$$\frac{\partial A_t}{\partial h_1} = -L_x\cot(\theta) \tag{31}$$

Now the cross sectional area and thus total crystal volume:

$$A_{cs} = h_1\frac{1}{2}\Big[(w/2) + L_t\Big] = h_1(w/2) - \frac{h_1^2}{2}\cot(\theta) \tag{32}$$

$$V = L_x A_{cs} = L_x\Big[h_1(w/2) - \frac{h_1^2}{2}\cot(\theta)\Big] = N\Omega \tag{33}$$

where Ω is the volume of a III-V pair, and N is the total number of these.

$$N = \frac{L_x}{\Omega}\Big[h_1(w/2) - h_1^2\cot(\theta)\Big] \tag{34}$$

$$\frac{\partial N}{\partial h_1} = \frac{L_x}{\Omega}\Bigg[(w/2) - \cot(\theta)h_1\Bigg] \tag{35}$$

From equation 25 we can now evaluate the excess chemical potential (assuming $(\partial h_1/\partial N) = (\partial N/\partial h_1)^{-1}$) due to surface energy contributions with $\alpha \in \{t, o\}$ for the facets. We find for regime 1:

$$\delta\mu_{s,h_1} = \frac{\Omega\Bigg[\gamma_o - \gamma_t\cos(\theta)\Bigg]}{\sin(\theta)\Bigg[(w/2) - \cot(\theta)h_1\Bigg]} \tag{36}$$

We will examine this solution further, but first we need to repeat the procedure for an adequately simple model of regime 2, once the crystal starts overgrowth. This model is shown in figure 28. In our simplified model overgrowth occurs by increasing the thickness of the additional layer marked by d, or equivalently by τ in figure 28. We have chosen to parametrize by the quantity h_2, and the overgrowth is constrained to two types of $\{111\}$ side facets.

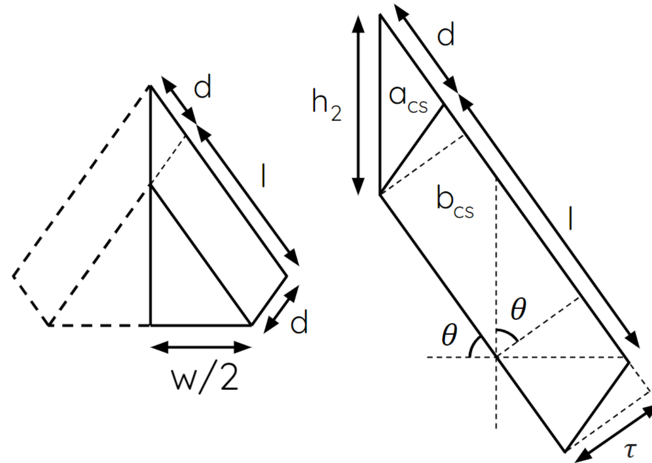

Figure 28: Schematic of NW with two types of $\{111\}$ side facets in the stage of growth labeled regime 2 (overgrowth). All quantities are kept in terms of the right side half of the NW.

$$l = \frac{(w/2)}{\cos(\theta)} \tag{37}$$

$$\tau = h_2\cos(\theta) \tag{38}$$

$$\frac{h_2}{2} = d\sin(\theta) \tag{39}$$

With the surface area (every facet is {111} type and has the same angle θ):

$$A_o = L_x\big(l + 2d\big) = L_x\left[\frac{(w/2)}{\cos(\theta)} + \frac{h_2}{\sin(\theta)}\right] \tag{40}$$

And the derivative:

$$\frac{\partial A_o}{\partial h_2} = L_x/\sin(\theta) \tag{41}$$

For the two cross sectional areas a_{cs} and b_{cs} we have:

$$a_{cs} = d\tau/2 = \frac{h_2^2}{4}\cot(\theta) \tag{42}$$

$$b_{cs} = l\tau = h_2(w/2) \tag{43}$$

which results in a total crystal volume of:

$$V = L_x\big(a_{cs} + b_{cs}\big) = L_x\left[h_2(w/2) + \frac{h_2^2}{4}\cot(\theta)\right] = N\Omega \tag{44}$$

And the derivative:

$$\frac{\partial N}{\partial h_2} = \frac{L_x}{\Omega}\left[(w/2) + \frac{h_2}{2}\cot(\theta)\right] \tag{45}$$

We can now express for regime 2:

$$\delta\mu_{s,h_2} = \frac{\Omega\gamma_o}{\sin(\theta)\left[(w/2) + \frac{h_2}{2}\cot(\theta)\right]} \tag{46}$$

From equations 36 and 46 we can plot the excess chemical potential per unit cell volume incorporated in the crystal due to surface energies for a crystal growth forced to follow the simple model outlined by figures 27 and 28.

The result is shown as the grey plot in figure 29 for $\theta = 54.74°$, which correspods to {111} facets. As remarked back in section 4.4.1 the energy cost of growing the full triangular cross section increases dramatically towards the end of regime 1. This suggests that overgrowth will be preferred before the full triangular cross section is formed. As expected, we find that the change in chemical potential diverges, as we approach the transition between regimes (dashed red line).

The black plot in figure 29 shows a similar investigation, assuming growth by equilibrium CWS as described in section 4.4.3. In this case the derivative in equation 25 is taken numerically, that is by evaluating the total surface energy for each volume value, then dividing the change in energy by the change in volume and factoring out the volume for a III-V pair, assuming 4 pairs per unit cell. We note that the investigation shown is carried out for a NW of trench width 120nm, and that this is somewhat size sensitive; the same kind of investigation relative to "full" cross sectional area will yield different

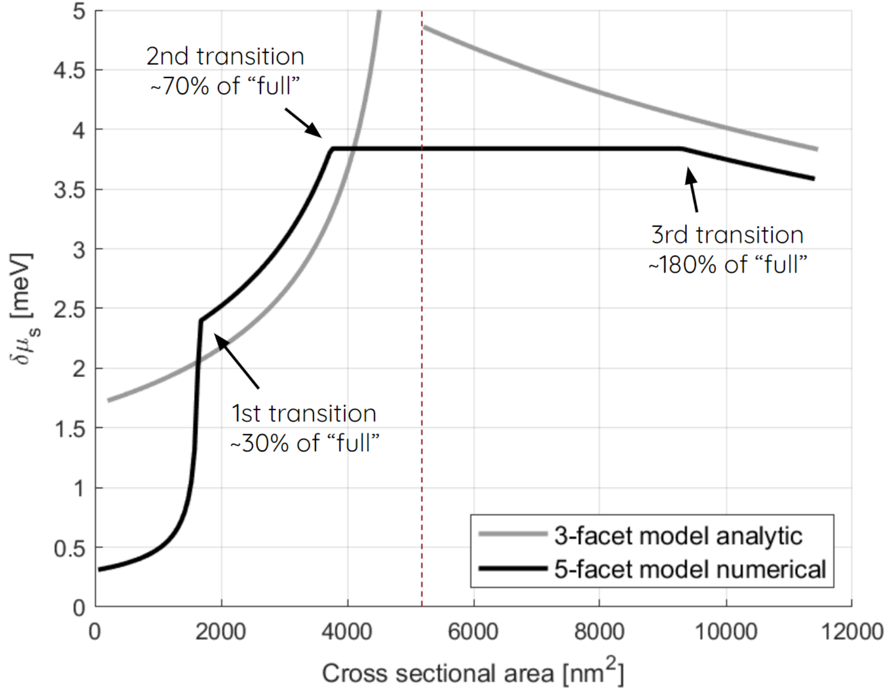

Figure 29: The excess chemical potential due to surface energy per III-V pair incorporated into the crystal for GaAs and a NW trench width of 120nm. The "3-facet model analytic" follows the growth procedure outlined in figures 27 and 28. The "5-facet model numerical" grows by equilibrium surface energy minimization as described in section 4.4.3, and the differentiation in equation 25 is done numerically. The dashed line marks the "full" volume at 0.3536 stw, which is also the transition between regimes 1 and 2 for the 3-facet model. Surface energy density values are those for GaAs shown in table 1, against which these plots can also be compared. The transitions marked are commented on in the main text.

results for a different trench width. This will become more apparent in the upcoming section 5.2, when we derive the analytic expressions for these changes in surface excess chemical potentials for the 5-facet model.

For the equilibrium solution (black plot in figure 29) we note three obvious transitions associated with three different "modes" of growth. From figure 20 we see that initial growth is by increasing the {113} facet lengths up to roughly 30% of "full" cross sectional area, followed by elongation of the {111} facets, marking the first transition. At approximately 70% of "full" the growth starts utilizing the vertical {110} facets, second transition, which continues until approximately 180% of "full" where the inverted {111} facets labeled r start showing up as the third transition. Just for clarity we must again stress that the numerical solution displayed in black in figure 29 is an equilibrium solution.

5.2 5-facet Chemical Potential Model

For a more in-depth treatment of the kinetics, we turn to the same NW model as the one in section 4.4.3 (see figure 30), where the crystal is free to grow by a flat {001} top facet as well as {113}, {111}, vertical {110} and inverted {111} facets. Note that we are returning to the 5-facet model (excluding facet m for now), and our constraint on trench width (see equation 19) means that the 5 facet lengths correspond to only 4 degrees of freedom. For our parametrization of the cross sectional NW shape we will choose the facet lengths L_j with $j \in \{i, o, v, r\}$ as our independent parameters (X_β's in equation 25), noting that L_t will be completely determined from equation 19.

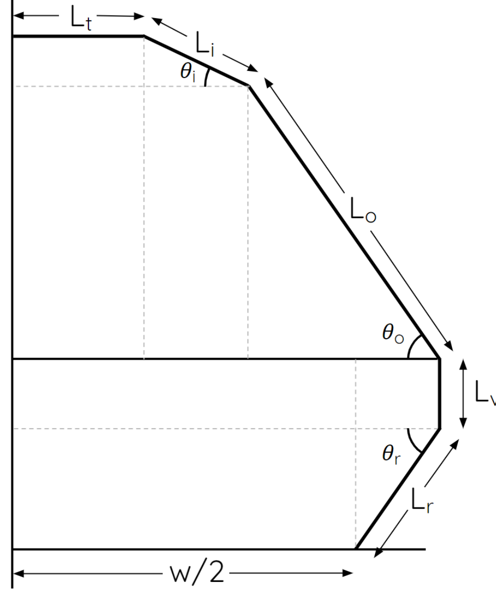

Figure 30: Schematic of NW with {001}, {113}, {111}, {110} and {111} facets labeled t, i, o, v and r, respectively, allowing overgrowth and a vertical facet. This figure is the same as figure 19, with different partitions for easier evaluation of the cross sectional area (see equations 48 and 49).

As in section 5.1 we will express all our quantities in terms of the half volume of a NW of length L_x and half cross section as shown in figure 30:

$$V = L_x A_{cs} = N\Omega \qquad \Rightarrow \qquad N = \frac{L_x}{\Omega} A_{cs} \tag{47}$$

Starting with the cross sectional area of the lower part of the cross section from L_r and L_v:

$$A_{cs\downarrow} = L_v \frac{w}{2} + L_r \frac{w}{2} \sin(\theta_r) + L_v L_r \cos(\theta_r) + \frac{1}{2} L_r^2 \cos(\theta_r) \sin(\theta_r) \tag{48}$$

Turning to the upper half we again note that we can express the area without reference to L_t, as expected:

$$
\begin{aligned}
A_{cs\uparrow} = L_o \sin(\theta_o)\left[\frac{w}{2} + L_r\cos(\theta_r) - \frac{1}{2}L_o\cos(\theta_o)\right] \\
+ L_i \sin(\theta_i)\left[\frac{w}{2} + L_r\cos(\theta_r) - L_o\cos(\theta_o) - \frac{1}{2}L_i\cos(\theta_i)\right]
\end{aligned}
\tag{49}
$$

We obviously have the total (half) cross sectional area as:

$$
A_{cs} = A_{cs\downarrow} + A_{cs\uparrow} \tag{50}
$$

and taking the derivatives with respect to our parameters:

$$
\begin{aligned}
\frac{\partial A_{cs}}{\partial L_r} = \frac{w}{2}\sin(\theta_r) + L_v\cos(\theta_r) + L_r\cos(\theta_r)\sin(\theta_r) \\
+ L_o\sin(\theta_o)\cos(\theta_r) + L_i\sin(\theta_i)\cos(\theta_r)
\end{aligned}
\tag{51}
$$

$$
\frac{\partial A_{cs}}{\partial L_v} = \frac{w}{2} + L_r\cos(\theta_r) \tag{52}
$$

$$
\frac{\partial A_{cs}}{\partial L_o} = \sin(\theta_o)\left[\frac{w}{2} + L_r\cos(\theta_r) - L_o\cos(\theta_o)\right] - L_i\sin(\theta_i)\cos(\theta_o) \tag{53}
$$

$$
\frac{\partial A_{cs}}{\partial L_i} = \sin(\theta_i)\left[\frac{w}{2} + L_r\cos(\theta_r) - L_o\cos(\theta_o) - L_i\cos(\theta_i)\right] \tag{54}
$$

Since our parameters are independent, we get:

$$
\frac{\partial A_j}{\partial L_k} = L_x\delta_{j,k} \tag{55}
$$

for $j, k \in \{i, o, v, r\}$ with $\delta_{j,k}$ as the Kronecker delta, noting that any interdependence between facet lengths can be expressed as a change to L_t. This is how we ensure that the parameters are independent. We still need to evaluate how $A_t = L_x L_t$, the surface area of the remaining facet, changes with respect to our parameters. Again, since our parameters are independent, this is pretty straight forward trigonometry:

$$
\frac{\partial A_t}{\partial L_r} = L_x\cos(\theta_r) \tag{56}
$$

$$
\frac{\partial A_t}{\partial L_v} = 0 \tag{57}
$$

$$
\frac{\partial A_t}{\partial L_o} = -L_x\cos(\theta_o) \tag{58}
$$

$$
\frac{\partial A_t}{\partial L_i} = -L_x\cos(\theta_i) \tag{59}
$$

Using equations 47 with 51-54 together with 55-59 lets us evaluate the sum in equation 25. For good measure we include the full expressions for the $\delta\mu_s$'s. A_α's are surface areas for facets in an NW of length L_x, the L_j's are our shape parameters, i.e. the facet lengths viewed in cross section with $j \in \{i, o, v, r\}$, and the s-subscripts are reminders, that the derivatives are due to surface energy excesses:

$$\delta\mu_{s,L_j} = \sum_\alpha \gamma_\alpha \frac{\partial A_\alpha}{\partial L_j}\frac{\partial L_j}{\partial N} \tag{60}$$

Given our observations above, we can evaluate the quantity in equation 60 for each of the 4 independent parameters:

$$\begin{aligned}\delta\mu_{s,L_r} &= \left[\gamma_r \frac{\partial A_r}{\partial L_r} + \gamma_t \frac{\partial A_t}{\partial L_r}\right]\frac{\partial L_r}{\partial N} \\ &= \frac{\Omega\left[\gamma_r + \gamma_t \cos(\theta_r)\right]}{\left[\frac{w}{2}\sin(\theta_r) + L_v\cos(\theta_r) + L_r\cos(\theta_r)\sin(\theta_r) + L_o\sin(\theta_o)\cos(\theta_r) + L_i\sin(\theta_i)\cos(\theta_r)\right]}\end{aligned} \tag{61}$$

$$\begin{aligned}\delta\mu_{s,L_v} &= \left[\gamma_v \frac{\partial A_v}{\partial L_v} + \gamma_t \frac{\partial A_t}{\partial L_v}\right]\frac{\partial L_r}{\partial N} \\ &= \frac{\Omega\gamma_v}{\left[\frac{w}{2} + L_r\cos(\theta_r)\right]}\end{aligned} \tag{62}$$

$$\begin{aligned}\delta\mu_{s,L_o} &= \left[\gamma_o \frac{\partial A_o}{\partial L_o} + \gamma_t \frac{\partial A_t}{\partial L_o}\right]\frac{\partial L_o}{\partial N} \\ &= \frac{\Omega\left[\gamma_o - \gamma_t\cos(\theta_o)\right]}{\left[\sin(\theta_o)\left[\frac{w}{2} + L_r\cos(\theta_r) - L_o\cos(\theta_o)\right] - L_i\sin(\theta_i)\cos(\theta_o)\right]}\end{aligned} \tag{63}$$

$$\begin{aligned}\delta\mu_{s,L_i} &= \left[\gamma_i \frac{\partial A_i}{\partial L_i} + \gamma_t \frac{\partial A_t}{\partial L_i}\right]\frac{\partial L_i}{\partial N} \\ &= \frac{\Omega\left[\gamma_i - \gamma_t\cos(\theta_i)\right]}{\left[\sin(\theta_i)\left[\frac{w}{2} + L_r\cos(\theta_r) - L_o\cos(\theta_o) - L_i\cos(\theta_i)\right]\right]}\end{aligned} \tag{64}$$

We note that the denominator in equation 64 is just $\sin(\theta_i)$ multiplied by L_t, expressed in terms of the independent parameters.

Given an existing crystal shape, we can measure the facet lengths L_α with $\alpha \in \{t, i, o, v, r\}$, and from equations 61-64 we can evaluate $\delta\mu_{s,L_j}$ with $j \in \{i, o, v, r\}$. This describes the additional cost incurred for crystal growth in terms of surface excess chemical potential for increasing each parameter.

In section 5.1 we described the change in chemical potential due to surface energy contributions from adding a single unit cell of volume to the crystal phase *given an assumption of a specific shape evolution*, either that described by figures 27 and 28 or equilibrium shape evolution depicted in figure 20. With the framework established in this section we can remove the simplifying constraint of a specific shape evolution and outline the steps necessary for dynamic shape evolution as iterative process.

5.2.1 Adding Crystal Volume on Facet t

For the purposes of a dynamic simulation we want to associate growth *on* a given facet with a cost in surface excess chemical potential. The reason is, that quantities such as an adatom density will be phrased on given facets (as back in section 3.2), rather than in terms of the shape parameters (the facet lengths), and we want to associate the adatom density with growth directly. The framework in the previous section does allow such an association, but in a convoluted way through growth of shape parameters. In short, growth by increasing a shape parameter does not necessarily have a direct correspondance to growth on any given facet, as we are about to see. First we note the negative relationship between increasing a parameter, e.g. growth by increasing L_t and growth of additional crystal volume *on* the associated facet t. In short, growing additional crystal volume on a given facet decreases the associated parameter.

This is illustrated in figure 31. We can express the infinitesimal height of the additional layer added to facet t as:

$$y_t = \sin(\theta_i)\delta L_{i,t} = -\tan(\theta_i)\delta L_{t,i} \tag{65}$$

where $\delta L_{i,t}$ denotes the change to the parameter L_i on the side towards facet t (inclined gold facet), and the minus sign is caused by L_t decreasing in length. The volumetric change, ΔV_t, from growth on facet t can be expressed in terms of the change in number of III-V pairs, ΔN, and the length of the translationally symmetric NW, L_x:

$$\Delta V_t = \Delta N\Omega = L_x L_t y_t \qquad \Rightarrow \qquad y_t = \frac{\Delta N\Omega}{L_x L_t} \tag{66}$$

We still need to be able to describe the change in shape parameters caused by this growth. By setting $\Delta N = 1$ in equation 66 and inserting into equation 65 we can evaluate the change to the facet lengths associated with the growth of one additional III-V pair on facet t:

$$\Delta L_{t,t} = -\frac{\Omega}{L_x L_t \tan(\theta_i)} \tag{67}$$

$$\Delta L_{i,t} = \frac{\Omega}{L_x L_t \sin(\theta_i)} \tag{68}$$

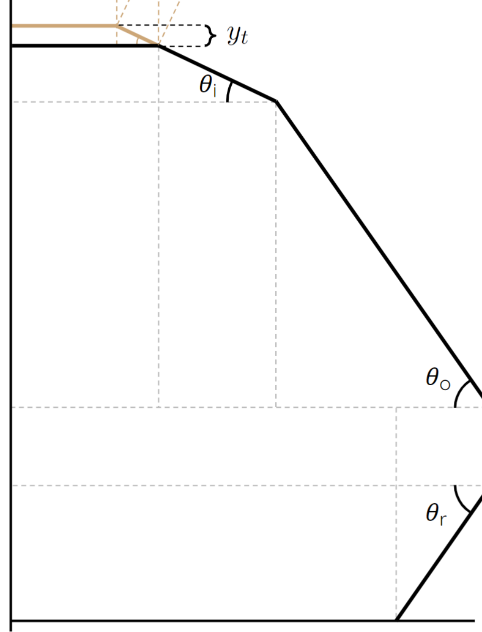

Figure 31: Schematic of NW showing infinitesimal volumetric change with growth on facet t, affecting the dependent parameter L_t and the independent parameter L_i. The original shape is shown in black, with the change marked in gold.

where $\Delta L_{i,t}$ denotes the change to facet length L_i associated with growth on facet t, and $\Delta L_{t,t}$ is the change to L_t that follows. The signs correctly show that L_t decreases with growth on facet t, and we note that the change diverges, as the facet vanishes, much like what we saw for "completing the triangular cross section" in figure 29, which was indeed elimination of a flat top facet towards the end of regime 1. In a physical system the facet length is quantized in units of the lattice parameter (multiplied by some constant dependent on orientation), so the divergence only exists in a continuum derivation, and will be finite in an atomistic treatment. We note that the contributions from edges and vertices will be more significant for very short facet lengths, but we will continue to ignore them for simplicity.

In summary growth of one additional III-V pair on facet t causes the changes in independent shape parameters described by equations 67 and 68, and thus changes the chemical potential by the amounts:

$$\Delta\mu_{s,t} = L_x\left[\gamma_t \Delta L_{t,t} + \gamma_i \Delta L_{i,t}\right] = \frac{\Omega}{L_t}\left[-\frac{\gamma_t}{\tan(\theta_i)} + \frac{\gamma_i}{\sin(\theta_i)}\right] \tag{69}$$

Since the length of facet L_t is quantized in terms of the lattice parameter, there is an upper limit on the surface excess chemical potential associated with growth on facet t. We note that the constraint on width (equation 15) lets us recast L_t to obtain equation 64. This is expected, since growth on facet t is just equivalent to growth by increasing L_i as seen in figure 31. However, growth on a facet is not always directly translated to

growth of a single shape parameter, as we are about to see.

5.2.2 Adding Crystal Volume on Facet i

In similar fashion we treat the addition of crystal volume to facet i as depicted in figure 32. The overall method will resemble that outlined in the previous section, and will be repeated for the facet o and v.

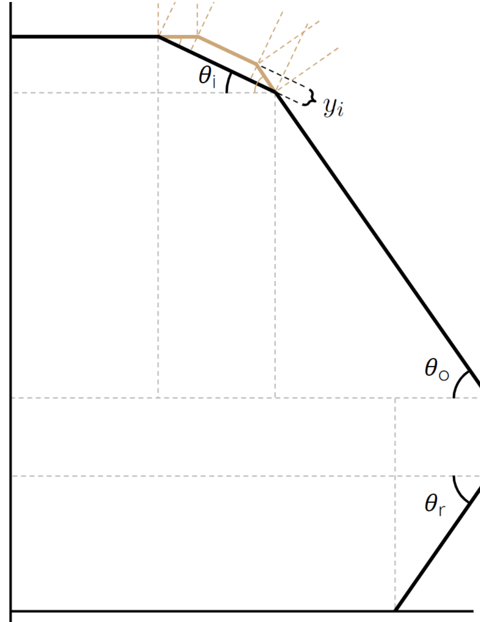

Figure 32: Schematic of NW showing infinitesimal volumetric change with growth on facet i, affecting the dependent parameter L_t and the independent parameters L_i and L_o. The original shape is shown in black, with the change marked in gold.

The infinitesimal height of the additional layer is:

$$\begin{aligned} y_i &= \sin(\theta_i)\delta L_{t,i} \\ &= -\tan(\theta_i)\delta L_{i,t} \\ &= \sin(\theta_o - \theta_i)\delta L_{o,i} \\ &= -\tan(\theta_o - \theta_i)\delta L_{i,o} \end{aligned} \tag{70}$$

where $\delta L_{t,i}$ again denotes changes to L_t associated with growth on facet i, as in the previous section. This time around $L_{i,t}$ denotes the change to L_i towards facet t. The first two lines of equation 70 are from considerations towards facet t, and the last two lines from considerations towards facet o. The volumetric change from growth on facet i, ΔV, can be expressed in terms of the change in number of III-V pairs, ΔN:

$$\Delta V_i = \Delta N \Omega = L_x L_i y_i \qquad \Rightarrow \qquad y_i = \frac{\Delta N \Omega}{L_x L_i} \tag{71}$$

We again set $\Delta N = 1$ in equation 71 and insert into equation 70 to track changes to the parameter L_i through changes in both ends, that is the sum of the following two:

$$\Delta L_{i,i} = -\frac{\Omega}{L_x L_i}\big[\cot(\theta_i) + \cot(\theta_o - \theta_i)\big] \tag{72}$$

Changes to the other parameters are:

$$\Delta L_{t,i} = \frac{\Omega}{L_x L_i \sin(\theta_i)} \tag{73}$$

$$\Delta L_{o,i} = \frac{\Omega}{L_x L_i \sin(\theta_o - \theta_i)} \tag{74}$$

We can now evaluate the change in chemical potential from growing the volume of a III-V pair, Ω, specifically on facet i in the same way we did in the previous section:

$$\Delta\mu_{s,i} = \frac{\Omega}{L_i}\left[\frac{\gamma_t}{\sin(\theta_i)} - \gamma_i\big[\cot(\theta_i) + \cot(\theta_o - \theta_i)\big] + \frac{\gamma_o}{\sin(\theta_o - \theta_i)}\right] \tag{75}$$

5.2.3 Adding Crystal Volume on Facet o

The addition of crystal volume to facet o is shown in figure 33.

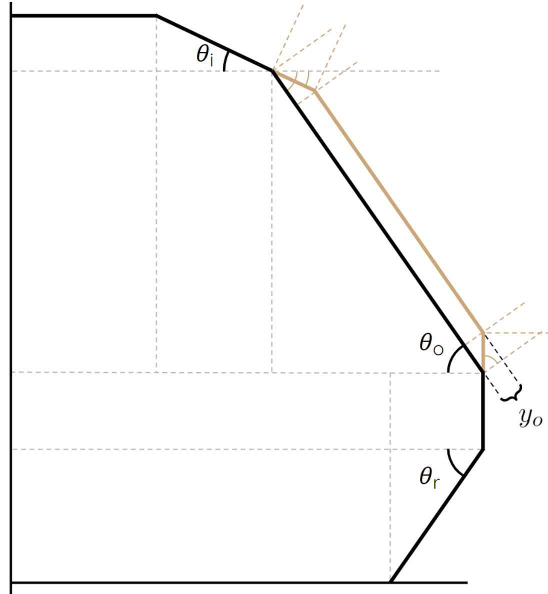

Figure 33: Schematic of NW showing infinitesimal volumetric change with growth on facet o, affecting the parameters L_i, L_o and L_v. The original shape is shown in black, with the change marked in gold.

The infinitesimal height of the additional layer on facet o is:

$$\begin{aligned}y_o &= \sin(\theta_o - \theta_i)\delta L_{i,o} \\ &= -\tan(\theta_o - \theta_i)\delta L_{o,i} \\ &= \cos(\theta_o)\delta L_{v,o} \\ &= -\cot(\theta_o)\delta L_{o,v}\end{aligned} \tag{76}$$

The first (last) two lines relate to the vertex towards facet i (r). The appearance of cos and cot here might seem surprising, since earlier corresponding expressions have only contained sin and tan. However, this is caused by the vertical facet v with $\theta_v = 90°$, and $\cos(\theta_o)$ is actually just a substitute for $\sin(\theta_v - \theta_o)$ and $\cot(\theta_o)$ for $\tan(\theta_v - \theta_o)$. This shows the obvious equivalence with equation 70. Continuing as before we find:

$$\Delta V_o = \Delta N\Omega = L_x L_o y_o \qquad \Rightarrow \qquad y_o = \frac{\Delta N\Omega}{L_x L_o} \tag{77}$$

Setting $\Delta N = 1$ in equation 77, inserting into equation 76 we find the change to the parameter L_o with addition of one III-V pair grown on facet o:

$$\Delta L_{o,o} = -\frac{\Omega}{L_x L_o}\big[\cot(\theta_o - \theta_i) + \tan(\theta_o)\big] \tag{78}$$

Changes to the other parameters are:

$$\Delta L_{i,o} = \frac{\Omega}{L_x L_o \sin(\theta_o - \theta_i)} \tag{79}$$

$$\Delta L_{v,o} = \frac{\Omega}{L_x L_o \cos(\theta_o)} \tag{80}$$

The change in chemical potential from growing the volume of a III-V pair on facet o is then:

$$\Delta\mu_{s,o} = \frac{\Omega}{L_o}\left[\frac{\gamma_i}{\sin(\theta_o - \theta_i)} - \gamma_o\big[\cot(\theta_o - \theta_i) + \tan(\theta_o)\big] + \frac{\gamma_v}{\cos(\theta_o)}\right] \tag{81}$$

From the considerations following equation 76 we note that the general form (for $\theta_i < \theta_o < \theta_v$) is:

$$\Delta\mu_{s,o} = \frac{\Omega}{L_o}\left[\frac{\gamma_i}{\sin(\theta_o - \theta_i)} - \gamma_o\big[\cot(\theta_o - \theta_i) + \cot(\theta_v - \theta_o)\big] + \frac{\gamma_v}{\sin(\theta_v - \theta_o)}\right] \tag{82}$$

5.2.4 Adding Crystal Volume on Facet v

The addition of crystal volume to facet v follows figure 34.

The infinitesimal height of the additional layer on facet v is:

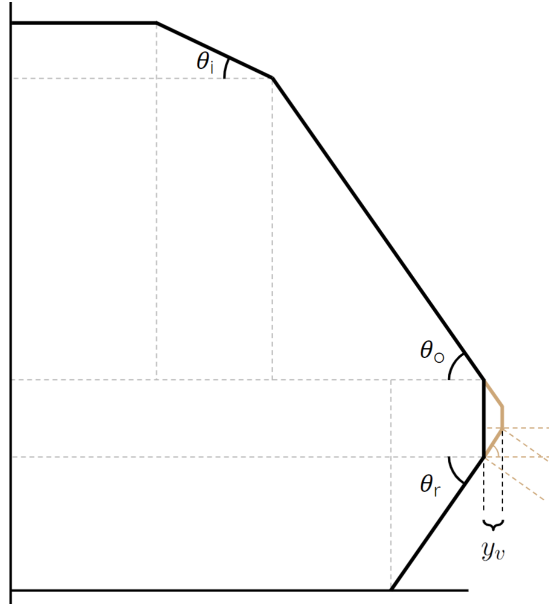

Figure 34: Schematic of NW showing infinitesimal volumetric change with growth on facet v, affecting the parameters L_o, L_v and L_r. The original shape is shown in black, with the change marked in gold.

$$\begin{aligned} y_v &= \cos(\theta_o)\delta L_{o,v} \\ &= -\cot(\theta_o)\delta L_{v,o} \\ &= \cos(\theta_r)\delta L_{r,v} \\ &= -\cot(\theta_r)\delta L_{v,r} \end{aligned} \tag{83}$$

We proceed to find:

$$\Delta V_v = \Delta N\Omega = L_x L_v y_v \qquad \Rightarrow \qquad y_v = \frac{\Delta N\Omega}{L_x L_v} \tag{84}$$

We set $\Delta N = 1$ in equation 84, inserting into equation 83 we find the changes to the parameter L_v caused by growing one additional III-V pair on facet v as:

$$\Delta L_{v,v} = -\frac{\Omega}{L_x L_v}\left[\tan(\theta_o) + \tan(\theta_r)\right] \tag{85}$$

Associated changes to the other parameters are:

$$\Delta L_{o,v} = \frac{\Omega}{L_x L_v \cos(\theta_o)} \tag{86}$$

$$\Delta L_{r,v} = \frac{\Omega}{L_x L_v \cos(\theta_r)} \tag{87}$$

The change in chemical potential from growing the volume of a III-V pair on facet v is:

$$\Delta\mu_{s,v} = \frac{\Omega}{L_v}\left[\frac{\gamma_o}{\cos(\theta_o)} - \gamma_v\big[\tan(\theta_o) + \tan(\theta_r)\big] + \frac{\gamma_r}{\cos(\theta_r)}\right] \tag{88}$$

This is consistent with the general form in equation 82 with $\theta_v = 90°$.

We also note that growth on facet r is not possible in our framework, since that would require growth on to the mask next to the NW trench. This goes to show, that the four degrees of freedom parametrizing the crystal shape by L_i, L_o, L_v and L_r correspond to four degrees of freedom describing crystal growth on facets t, i, o and v.

In summary, for any given crystal shape parametrized by our shape parameters (L_i, L_o, L_v and L_r), we can describe growth of an additional III-V pair on any allowed facet (t, i, o or v) in terms of the changes to our shape parameters (equations 67, 68, 72, 73, 74, 78, 79, 80, 85, 86 and 87) as well as the change in surface excess chemical potential from those changes (equations 69, 75, 81 and 88).

6 Future Work: Dynamic Modelling

The picture of adatom density outlined in section 3 is of course simplified with effective transition rates being only dependent on material region, and the resulting adatom distribution being steady state. Crystal growth in MBE is known to be an out-of-equilibrium process, and there is no reason to expect a simple relationship between the steady state adatom density and the final mass distribution after growth.

Similarly, shape evolution by CWS described in section 4 is simplified in the sense that it produces equilibrium shapes. These equilibrium shapes represent energetic minima for varying crystal volumes under constraints, but crystal growth is expected to occur not only in the one energetically optimal position but instead across the morphology.

In a more general picture the transition rates are at all times functions of a variety of factors. Immediately obvious factors are thermodynamic parameters such as temperature and pressure, but the energy of a given state which directly impacts transition rates, also depends both on facet type and the current crystal shape through the change in chemical potentials seen in section 5.

The sort of shape dependent evolution of chemical potentials with changes in shape parameters described in the latter sections above and the resulting shifts in adatom density which would follow, together call for a dynamic model, where adatom density, faceting of crystal shape and transition rates are all dynamically updated in very short time steps throughout growth. While some kinks will still need to be ironed out, we can draft a to-do-list for this type of model. Actually setting up the dynamic model with thermodynamic data is, unfortunately, outside the scope of this thesis but an obvious point for future work.

We need to establish a general setup for the dynamic model. In principle we want a continuum simulation, but we can achieve an approximation by a simple 1-dimensional finite element method (FEM). In practice this means that we seek solutions on a mesh of discrete points, and if necessary, interpolate the solutions between mesh points. This is exactly what we did in section 3.3, only we did it for steady state and with transition rates dependent only on region, trench or mask.

For any given simulation NW width, pitch and distance between NW arrays are fixed quantities, exactly like in section 3. We can also restrict ourselves to one NW direction per simulation, e.g. $[1\bar{1}0]$, and a list of allowed facets akin to the method in section 4. If we define our 1-dimensional axis, x, to run along the surface of the crystal morphology (see figure 35), we can now fully describe the morphology with an array, B, of boundary points. The boundary points are the x-values for all boundaries between regions, with regions now describing not just the difference between mask and trench but also different crystal facets. We can also describe the adatom density across the entire morphology by the function $\rho(x)$. Note that the length of the x-axis will vary from step to step, and we will need to adjust our adatom density $\rho(x)$ accordingly (see figure 35d).

With the basic definition of our axis x as well as B, and $\rho(x)$ in place, we can describe the calculations required for each time step (dt) passing in simulation. The list is ordered chronologically with each step depending on the previous steps. The first iteration should

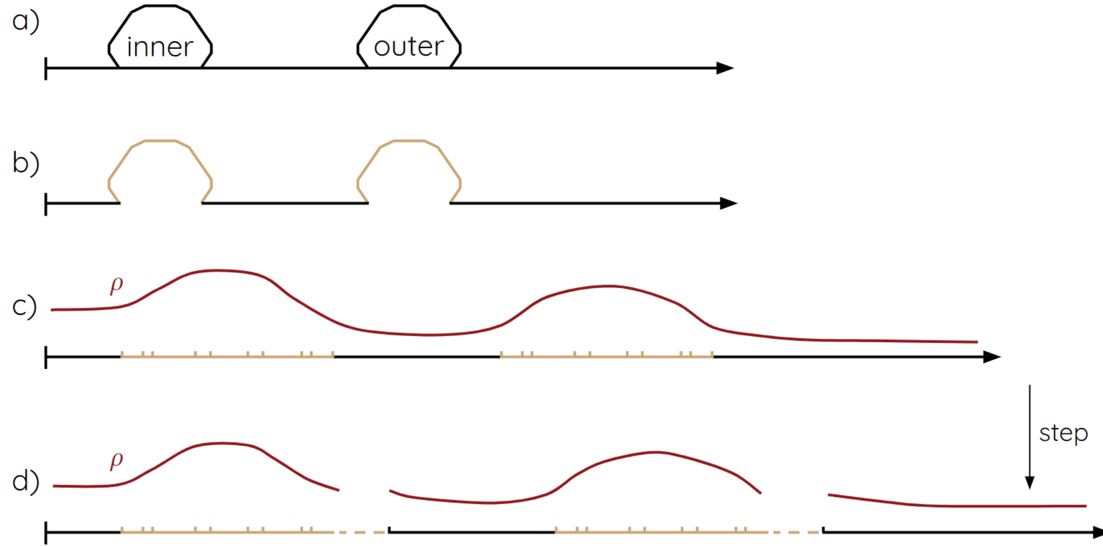

Figure 35: Schematic showing the 1-dimensional geometry for a dynamic model of crystal growth. **a)** The mask and current NW morphology. Left-most boundary is the mirror symmetry plane in the middle of the 4-array. **b)** The 1-dimensional axis runs along the mask (black) as well as the current NW facets (gold). **c)** The 1-dimensional axis is shown as "flattened", along with the adatom density, ρ. Small markers indicate boundary points. **d)** Adding a time step changes the faceting and thus the dimensions of the axis x, creating complications for keeping quantities between time steps.

be able to run from any valid morphology including a "blank slate" with empty trenches.

1. Current 1-dimensional axis along facets is x, current adatom density is $\rho(x)$, and current boundary points is B.

2. Calculate transition rates $\Gamma_{as}(x)$, $\Gamma_{av}(x)$, $\Gamma_{sa}(x)$ and $\Gamma_{va}(x)$ from current quantities across x.

   Every transition rate is a function of chemical potentials of different phases, facet type at x and current crystal shape parametrized by B.

3. Subtract desorption and growth from the adatom density $\rho(x)$ with the term $-dt\big[\Gamma_{as}(x) + \Gamma_{av}(x) - \Gamma_{sa}(x) - \Gamma_{va}(x)\big]$.

4. Add growth to crystal shape with the term $+dt\big[\Gamma_{as}(x) - \Gamma_{sa}(x)\big]$.

5. Update $x \to x^*$ and $B \to B^*$ according to the growth calculated above.

6. Update $\rho(x) \to \rho^*(x)$, rescaling according to $B \to B^*$, with the total adatom count on any given facet obeying previous count with the subtraction calculated above.

7. Add beam flux to $\rho^*(x)$ to obtain $\rho^*_b(x)$.

8. Calculate diffusion rate from $\nabla\big(D\nabla\rho_b^*(x)\big)$ and update $\rho_b^*(x) \to \rho_d^*(x)$ from adatom density after beam to adatom density after diffusion.

9. Advance time by dt and use latest versions of x^*, $\rho_d^*(x)$ and B^* as current version for next step.

The list outlined above looks deceptively simple, but especially the second point, coupling all transition rates to chemical potentials of different phases and facets makes this procedure much more involved than what meets the eye.

In principle the necessary quantities are available in literature together with the framework of section 5, but the task itself is left for future work.

7 Conclusion

This thesis shows the potential of modelling crystal growth, based on two theoretical "domains": an examination of the steady state diffusion behaviour of adatoms during growth, resulting in an overall distribution of crystal volume available for growth, and equilibrium shape evolution of the resulting crystal volume during growth by constrained Wulff shaping.

In both domains the models proposed in this thesis reliable reproduce the trends observed in experiments for SAG NW growth. While much further work is desirable, the methods in this thesis represent a basic understanding of the morphologies produced in SAG.

The framework of changes in chemical potentials associated with growth outlined in the last sections sets the stage for dynamic modelling with transition rates being a function of existing facets and chemical potentials changing dynamically during growth.

7.1 Acknowledgements

The work presented in this thesis is my personal contribution to several larger, collaborative efforts. The thesis has at every step been shaped, guided and enlightened by the experimental work conducted, and the theoretical insights provided, by members of the research group at Microsoft Quantum Materials Lab (MQML) Copenhagen.

No thesis without a supervisor, or in this case a team of supervisors. I wish to express the utmost gratitude towards Peter Krogstrup for his patience, guidance and insight, and for the opportunity to shape and develop my thesis with ample support along the way. Thank you to Sergej Schuwalow and Tomas Stankevic for co-supervising my thesis, for always being available for a chat on theoretical matters and for general guidance throughout. I also wish to thank another unlisted "supervisor", Jeanette Pyrdol, for all her amazing work with the entire team.

I must emphasize experimental observations and data graciously made available by Anna Wulff Christensen, Martín Espiñeira, Daria Beznasyuk as well as general support in all matters from Thue Nikolajsen, Morten Hannibal Madsen, Ajuan Cui, Gunjan Nagda, Somya Gupta, Mohana Rajpalke, Jung-hyun Kang and the rest of the MQML team.

References

[1] A. Y. Kitaev (2003). *Fault-tolerant quantum computation by anyons.* Annals of Physics, 303(1), 2–30. doi:10.1016/s0003-4916(02)00018-0

[2] R. W. Keyes (2005). *Challenges for quantum computing with solid-state devices.* Computer, 38(1), 65–69. doi:10.1109/mc.2005.13

[3] R. M. Lutchyn, J. D. Sau, and S. Das Sarma (2010). *Majorana Fermions and a Topological Phase Transition in Semiconductor-Superconductor Heterostructures.* Physical Review Letters, 105(7). doi:10.1103/physrevlett.105.077001

[4] T. Karzig, C. Knapp, R. M. Lutchyn, P. Bonderson, M. B. Hastings, C. Nayak, J. Alicea, K. Flensberg, S. Plugge, Y. Oreg, C. M. Marcus, and M. H. Freedman (2017). *Scalable designs for quasiparticle-poisoning-protected topological quantum computation with Majorana zero modes.* Physical Review B, 95(23). doi:10.1103/physrevb.95.235305

[5] F. Krizek, J. E. Sestoft, P. Aseev, S. Martí-Sánchez, S. Vaitiekėnas, L. Casparis, S. A. Khan, Y. Liu, T. Stankevič, A. M. Whiticar, A. Fursina, F. Boekhout, R. Koops, E. Uccelli, L. P. Kouwenhoven, C. M. Marcus, J. Arbiol, and P. Krogstrup (2018). *Field effect enhancement in buffered quantum nanowire networks.* Phys. Rev. Materials 2, 093401. doi:10.1103/PhysRevMaterials.2.093401

[6] P. Aseev, A. Fursina, F. Boekhout, F. Krizek, J. E. Sestoft, F. Borsoi, S. Heedt, G. Wang, L. Binci, S. Martí-Sánchez, T. Swoboda, R. Koops, E. Uccelli, J. Arbiol, P. Krogstrup, L. P. Kouwenhoven, and P. Caroff (2018). *Selectivity map for molecular beam epitaxy of advanced III-V quantum nanowire networks.* Nano Letters. doi:10.1021/acs.nanolett.8b03733

[7] M. Henini (2018). *Molecular Beam Epitaxy (MBE): From Research to Mass Production, Second Edition* Elsevier. ISBN:9780128121368

[8] T. Sakamoto (1988). *Rheed Oscillations in MBE and Their Applications to Precisely Controlled Crystal Growth.* Physics, Fabrication, and Applications of Multilayered Structures, 93–110. doi:10.1007/978-1-4757-0091-6_5

[9] G. Lehmpfuhl, A. Ichimiya, and H. Nakahara (1991). *Interpretation of RHEED oscillations during MBE growth.* Surface Science, 245(1-2), L159–L162. doi:10.1016/0039-6028(91)90459-6

[10] P. Krogstrup, H. I. Jørgensen, E. Johnson, M. H. Madsen, C. B. Sørensen, A. F. i Morral, M. Aagesen, J. Nygård, and F. Glas (2013). *Advances in the theory of III–V nanowire growth dynamics.* Journal of Physics D: Applied Physics, 46(31), 313001. doi:10.1088/0022-3727/46/31/313001

[11] M. Espiñeira, A. W. Christensen et al. (2020). In preparation.

[12] K. Pearson (1905). *The Problem of the Random Walk.* Nature, 72(1865), 294–294. doi:10.1038/072294b0

[13] Rayleigh (1905). *The Problem of the Random Walk.* Nature, 72(1866), 318–318. doi:10.1038/072318a0

[14] J. Johansson, C. P. T. Svensson, T. Mårtensson, L. Samuelson, and W. Seifert (2005). *Mass Transport Model for Semiconductor Nanowire Growth.* The Journal of Physical Chemistry B, 109(28), 13567–13571. doi:10.1021/jp051702j

[15] A. Fick (1855). *V. On liquid diffusion.* The London, Edinburgh, and Dublin Philosophical Magazine and Journal of Science, 10(63), 30-39. doi:10.1080/14786445508641925

[16] MATLAB (2019) *(R2019a).* Natick, Massachusetts: The MathWorks Inc.

[17] A. W. Christensen (2019). *Statistical Analysis of Selective Area Grown Nanowire Crystal Morphologies.* Master's Thesis, Niels Bohr Institute, University of Copenhagen.

[18] M. Salvalaglio (2018). *On the mechanistic studies of the growth of anisotropic particles (theory and simulation).* Anisotropic Particle Assemblies, 55–103. doi:10.1016/b978-0-12-804069-0.00003-4

[19] T. L. Einstein (2015). *Equilibrium Shape of Crystals.* Handbook of Crystal Growth, 215–264. doi:10.1016/b978-0-444-56369-9.00005-8

[20] R. F. Sekerka (2005). *Equilibrium and growth shapes of crystals: how do they differ and why should we care?* Crystal Research and Technology, 40(4-5), 291–306. doi:10.1002/crat.200410342

[21] R. V. Zucker, D. Chatain, U. Dahmen, S. Hagège, and W. C. Carter (2012). *New software tools for the calculation and display of isolated and attached interfacial-energy minimizing particle shapes.* Journal of Materials Science, 47(24), 8290–8302. doi:10.1007/s10853-012-6739-x

[22] G. D. Barmparis, Z. Lodziana, N. Lopez and I. N. Remediakis (2015). *Nanoparticle shapes by using Wulff constructions and first-principles calculations.* Beilstein Journal of Nanotechnology, 6, 361–368. doi:10.3762/bjnano.6.35

[23] I. W. Yeu, G. Han, J. Park, C.S. Hwang, and J.-H. Choi (2019). *Equilibrium crystal shape of GaAs and InAs considering surface vibration and new (111)B reconstruction: ab-initio thermodynamics.* Scientific Reports, 9(1). doi:10.1038/s41598-018-37910-y

[24] A. Jenichen, and C. Engler (2013). *Reconstructions and surface facets of the GaAs(112)A and (112)B surfaces: First-principles DFT supercell calculations.* Surface Science, 608, 204–211. doi:10.1016/j.susc.2012.10.011

[25] K. Momma, and F. Izumi (2011) *VESTA 3 for three-dimensional visualization of crystal, volumetric and morphology data.* Journal of Applied Crystallography, 44, 1272-1276. doi:10.1107/S0021889811038970

[26] P. Krogstrup, N. L. B. Ziino, W. Chang, S. M. Albrecth, M. H. Madsen, E. Johnson, J. Nygård, C. M. Marcus, and T. S. Jespersen (2015) *Epitaxy of semiconductor–superconductor nanowires.* Nature Materials, 14(4), 400–406. doi:10.1038/nmat4176

[27] N. Moll, A. Kley, E. Pehlke, and M. Scheffler (1996). *GaAs equilibrium crystal shape from first principles.* Physical Review B, 54(12), 8844–8855. doi:10.1103/physrevb.54.8844

[28] S. B. Zhang, and S.-H. Wei (2004). *Surface Energy and the Common Dangling Bond Rule for Semiconductors.* Physical Review Letters, 92(8). doi:10.1103/physrevlett.92.086102

[29] V. Pankoke, P. Kratzer, and S. Sakong (2011). *Calculation of the diameter-dependent polytypism in GaAs nanowires from an atomic motif expansion of the formation energy.* Physical Review B, 84(7). doi:10.1103/physrevb.84.075455

8 Appendix

8.1 Diffusion Solutions for Steady State Adatom Density

In the following subparts of this appendix we will examine different solutions to the steady state adatom density for comparison with experimentally observed trends [17]. The "default" parameters are listed in the code, section 8.4.1.

8.1.1 Diffusion Solutions and Rates

In the first study we will vary the desorption rate, Γ_{av}, on the mask (through a variation of ν_{av}, see equation 11) to see how the source behaviour is caused by a higher rate of desorption on the mask than rate of incorporation in the trenches. In the code, section 8.4.1, this is a variation of the parameter `nu_SiOav`. The results are shown in figure 36.

We notice the clear trend that the size of the Γ-ratio controls the behaviour as source or sink; Γ-ratio > 1 leads to source behaviour, and Γ-ratio < 1 leads to sink behaviour. Additionally we see that a lower Γ-ratio significantly increases the steady state adatom density across the geometry, as we would expect. As such, source behaviour is tied to a lowered adatom density and presumably a lower growth rate.

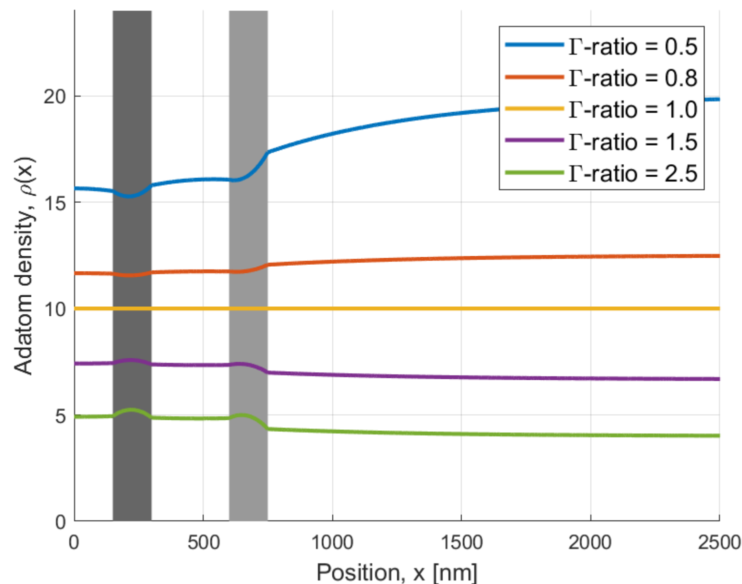

Figure 36: Steady state adatom density shown for 5 different ratios of desorption rate on mask divided by incorporation rate in the trenches (Γ-ratio). Inner NW region is shown in dark grey, outer NW in light grey. The desorption rate on the mask is varied, while all other quantities are kept constant. A clear trend is seen with Γ-ratio > 1 resulting in source behaviour and Γ-ratio < 1 resulting in sink behaviour. The "strength" of the source or sink behaviour scales with the size of Γ-ratio.

8.1.2 Diffusion Solutions and Nanowire Pitch

Next we will examine how the dependence on pitch, to demonstrate the lowering of steady state adatom density with increasing pitch. In the code, section 8.4.1, this is a variation of the parameter p, not to be confused with the general state p. Since changing the pitch changes the 1-dimensional axis, the solutions $\rho(x, p)$ are not easily plotted together. We have chosen instead to plot this average value of $\rho(x)$ across the outer and inner NW regions as a function of pitch.

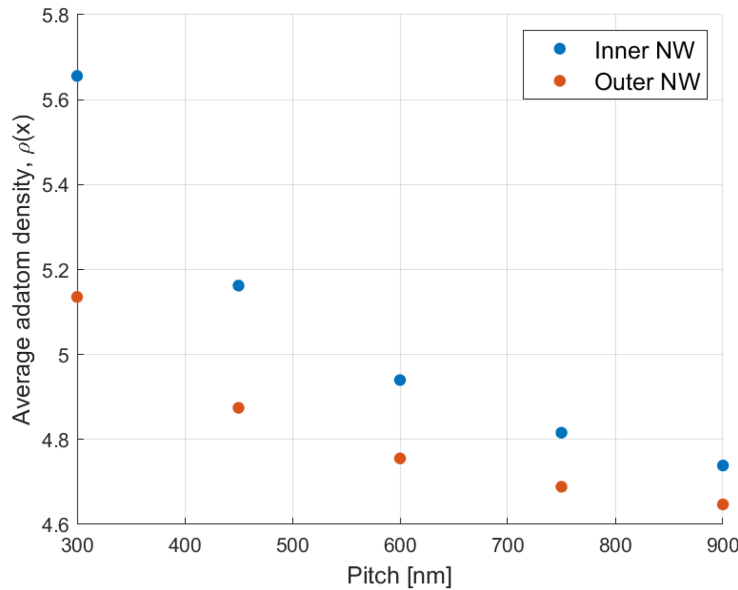

Figure 37: Steady state adatom density shown for 5 different values of pitch. Note that the y-axis does not go to zero. With increasing pitch we clearly see that the overall steady state adatom density decreases, and the ratio between outer and inner NW averages tends towards unity; the source behaviour becomes "weaker" with increasing pitch.

8.2 Stereographic Projection for [100] type NWs

Since $\langle 100 \rangle$ and $\langle 110 \rangle$ make up the main high symmetry directions for the (001) substrate, the stereographic projection for the $\langle 100 \rangle$ type zincblende NW is included here in figure 38. A similar version for the $\langle 110 \rangle$ is found in the main text section figure 10.

8.3 3-facet Model Analytic Solutions for CWS

As mentioned in section 4.4.1 the analytic solutions for the facet lengths L_k with $k \in \{t, i, o\}$ under CWS for a given cross sectional area can be expressed in terms of the known quantities of area, width, the facet angles and surface energy densities. While

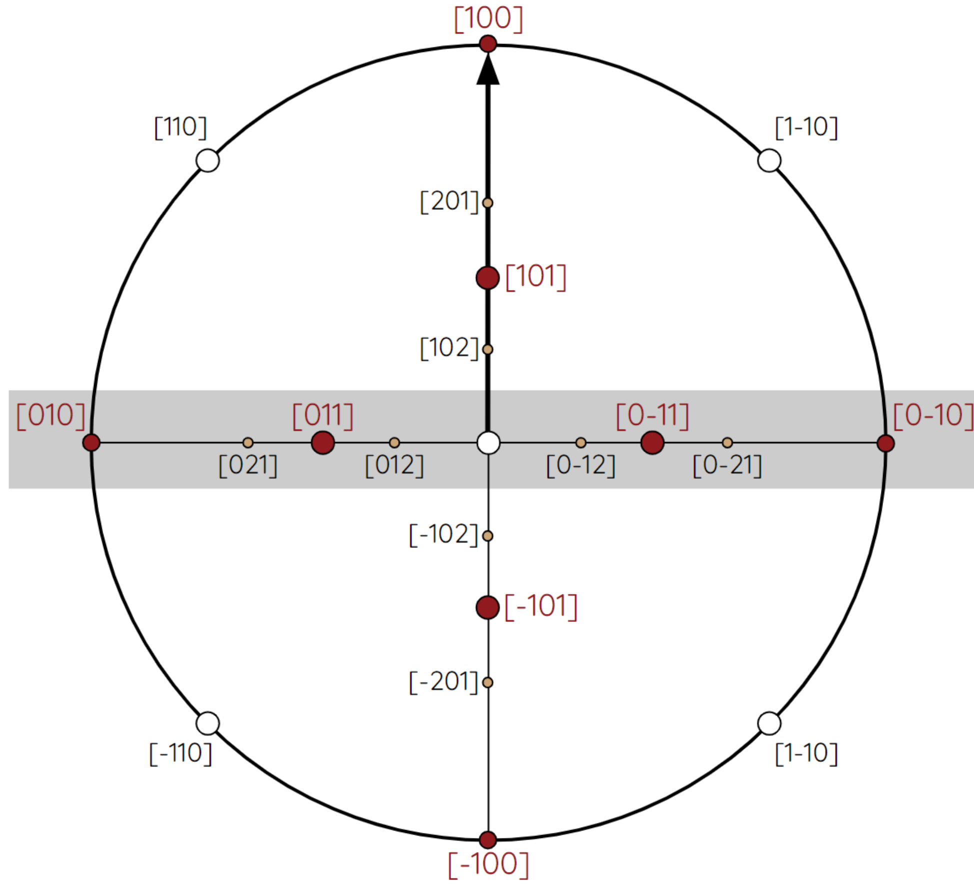

Figure 38: Part of a stereographic projection for zincblende on a (001) substrate with focus on the [100] NW type. The figure only shows the main directions and facets in the $\langle 100 \rangle$ type directions for increased readability. The [100] direction is upwards with allowed facets perpendicular to the NW direction, marked by the shaded area. The angle with respect to the (001) substrate starts from 0° in the center and increases linearly to 90° at the perimeter.

this analytic solution is possible, the numerical method for solving the CWS (see section 4.4.2) seems prefereable both in terms of efficiency and range of validity.

Nevertheless the analytic solutions for CWS in the case of the 3-facet model as shown in figure 16 are included here for the sake of completion and to serve as proof of the method. Throughout A and W will denote the half area and half width from figure 16, respectively.

The expression for L_o is quite esoteric, and multiple sub-expressions are necessary:

$$L_o = \frac{N_{oa} N_{ob} \sqrt{S_o} + N_{of} N_{og}}{D_o} \tag{89}$$

Equations 93, 94 and 95 are to be inserted into equation 92 (in the square root), equation 97 is to be inserted into equation 98, and finally equations 90, 91, 92, 96, 97, and 98 are to be inserted into equation 89.

The numerator of equation 89 carries SI-units of [J^2/m], and the denominator [J^2/m^2], which makes the units for L_o come out as length [m] as desired. We show the different terms and analyze units below:

$$N_{oa} = \Big(E_t \cos(\theta_i) + E_i\Big)\cos(\theta_o) - E_o\cos(\theta_i) \tag{90}$$

$$N_{ob} = \sqrt{2}\Big(\sin(\theta_i)\cos(\theta_o) + \cos(\theta_i)\sin(\theta_o)\Big) \tag{91}$$

We note that N_{oa} has units of energy density [J/m] and N_{ob} has no units.

$$\begin{aligned} S_o = \sin(\theta_i)\cos^2(\theta_o)\Bigg[&N_{oc}\cos(\theta_o)\sin(\theta_o) - N_{od}\cos^2(\theta_o)\cos^2(\theta_i) + \cos(\theta_o)\,N_{oe}\cos(\theta_i) \\ &- 2\cos^2(\theta_o)\Bigg(-\frac{1}{4}E_i W^2\Big(\cos(\theta_o) - 1\Big)\Big(\cos(\theta_o) + 1\Big)\sin(\theta_i) \\ &+ A\cos(\theta_o)\Big(-E_t\cos(\theta_o) + E_o\Big)\Bigg)E_i\Bigg]\cos^2(\theta_i) \end{aligned} \tag{92}$$

This shows that S_o carries units of length squared times energy density squared [J^2] (it will become obvious below, that N_{oc}, N_{od} and N_{oe} carry units [J^2]).

$$\begin{aligned} N_{oc} = &\frac{1}{2}W^2\Big(-E_t\cos(\theta_o) + E_o\Big)^2\cos^3(\theta_i) \\ &- \Bigg(A\Big(-E_t\cos(\theta_o) + E_o\Big)\sin(\theta_i) + W^2 E_i\cos(\theta_o)\Bigg)\Big(-E_t\cos(\theta_o) + E_o\Big)\cos^2(\theta_i) \\ &+ \Bigg[2AE_i\cos(\theta_o)\Big(-E_t\cos(\theta_o) + E_o\Big)\sin(\theta_i) - \frac{1}{2}W^2\Bigg(\left({E_i}^2 + {E_t}^2\right)\cos^2(\theta_o) \\ &\quad - 2E_o E_t\cos(\theta_o) - {E_i}^2 + {E_o}^2\Bigg)\Bigg]\cos(\theta_i) \\ &+ \cos(\theta_o)\Big(A\sin(\theta_i)E_i\cos(\theta_o) + W^2\left(-E_t\cos(\theta_o) + E_o\right)\Big)E_i \end{aligned} \tag{93}$$

$$N_{od} = A\Big(- E_t \, \cos(\theta_o) + E_o \Big)^2 \cos^3(\theta_i) + 2\left(- E_t \, \cos(\theta_o) + E_o \right) \times \left[- \frac{1}{4} W^2 \Big(\cos(\theta_o) - 1 \Big) \Big(\cos(\theta_o) + 1 \Big) \Big(- E_t \, \cos(\theta_o) + E_o \Big) \sin(\theta_i) + A E_i \, \cos^3(\theta_o) \right] \tag{94}$$

$$N_{oe} = E_i \, W^2 \Big(\cos(\theta_o) - 1 \Big) \Big(\cos(\theta_o) + 1 \Big) \Big(- E_t \, \cos(\theta_o) + E_o \Big) \sin(\theta_i) + \cos(\theta_o) \, A \Big(\left({E_i}^2 + {E_t}^2 \right) \cos^2(\theta_o) - 2\, E_o \, E_t \, \cos(\theta_o) - {E_i}^2 + {E_o}^2 \Big) \tag{95}$$

Equations 93, 94 and 95 show that N_{oc}, N_{od} and N_{oe} have units of length squared times energy density squared [J^2] as claimed above.

$$N_{of} = 2\, \cos(\theta_o) \, W \Bigg[- \sin(\theta_i) \left(\frac{1}{2} E_t \, \cos(\theta_i) + E_i \right) E_t \, \cos^2(\theta_o) + \Big(\cos(\theta_i) \, E_o \, E_t \, \sin(\theta_i) + E_i \, E_o \, \sin(\theta_i) - \frac{1}{2} {E_i}^2 \sin(\theta_o) \Big) \cos(\theta_o) - \frac{1}{2} {E_o}^2 \sin(\theta_i) \cos(\theta_i) \Bigg] \tag{96}$$

This determines N_{of} as having units of energy density squared times length [J^2/m]

$$N_{og} = \Big(\cos(\theta_i) - \cos(\theta_o) \Big) \Big(\cos(\theta_i) + \cos(\theta_o) \Big) \cos(\theta_i) \tag{97}$$

We note that N_{og} has no units.

$$D_o = 2 \cos^2(\theta_o) \Bigg[- \sin(\theta_i) \left(\frac{1}{2} E_t \, \cos(\theta_i) + E_i \right) E_t \, \cos^2(\theta_o) + \Big(\cos(\theta_i) \, E_o \, E_t \, \sin(\theta_i) + E_i \, E_o \, \sin(\theta_i) - \frac{1}{2} {E_i}^2 \sin(\theta_o) \Big) \cos(\theta_o) - \frac{1}{2} {E_o}^2 \sin(\theta_i) \cos(\theta_i) \Bigg] N_{og} \tag{98}$$

We find that D_o has units of energy density squared [J^2/m^2].

This concludes the terms of equation 89 and thus determines L_o from known quantities. We are now in a position to find the other two facet lengths. We start with the L_i:

$$L_i = \frac{\sqrt{-2\, N_i \cos^2(\theta_i) \sin(\theta_i)} + \Big(- L_o \, \cos(\theta_o) + W \Big) \sin(\theta_i) \cos(\theta_i)}{\sin(\theta_i) \cos^2(\theta_i)} \tag{99}$$

Equation 100 is to be inserted into equation 99 to obtain the full expression for the facet length L_i in terms of known quantities. We note that L_i has units of length as expected (since N_i has units of length squared [m^2], shown below).

$$N_i = \left(\frac{1}{2}\,{L_o}^2 \sin\left(\theta_o\right) \cos\left(\theta_o\right) - L_o\, \sin\left(\theta_o\right) W + A\right) \cos\left(\theta_i\right) - \frac{1}{2}\,\sin\left(\theta_i\right) \Big(- L_o\, \cos\left(\theta_o\right) + W \Big)^2 \tag{100}$$

This shows that N_i has units of length squared [m^2]. Finally we can obtain the last facet length in a straight forward fashion:

$$L_t = -L_i\, \cos\left(\theta_i\right) - L_o\, \cos\left(\theta_o\right) + W \tag{101}$$

This concludes the analytic solution for facet lengths under the CWS displayed in figure 16 for a given cross sectional area.

8.4 MATLAB codes

The MATLAB codes used to generate results shown throughout the thesis are included here for sake of completion. All codes are compatible with MATLAB version 2019a. Some sections are copy/pasted between different codes and thus duplicate lines/sections may appear across different codes. Code functionality is guaranteed but comments inside the code have not been proof-read.

8.4.1 fourarray_bvp5c

This code generates the steady state adatom density plots displayed in section 3.3. This calls the MATLAB-internal function 'bvp5c', which solves multi-point boundary value problems.
The long expression in line 44 is from analytic solution to the simpler problem of an infinite array of NWs, solving for the steady state adatom flux across the NW-mask boundary. This was obtained via a symbolic solver (not included).

```
1  %% Save plots or not?
2  plotsave = 0;
3  plotshow = 'on';
4  %% Defining geometry
5  d = 10000; % inter-array distance
6  w = 150; % NW width
7  p = 450; % NW pitch
8  %% Derived important points in geometry
9  x0 = 0; % boundary points, used for BC's and merging plots
10 x1 = (p-w)/2;
11 x2 = (p+w)/2;
12 x3 = (3*p-w)/2;
13 x4 = (3*p+w)/2;
14 x5 = d/2;
15
16 xresolution = 1; % resolution for x-array, mainly for plotting
17 xarray = linspace(0,d/2,1+(d/2)*xresolution); % for 4-array
18 %% Defining thermodynamic parameters
19 global D_NW nu_NWav nu_NWas F_NW D_SiO nu_SiOav nu_SiOas F_SiO nuNWoverSiO
20 F_beam = 100;  % uniform rate of adatoms from beam
21
22 % for NW
23 difflength_NW = 200; % diffusion length on NW
24 nu_NWav = 0; % adatom to vapor rate factor on NW
25 nu_NWas = 10; % adatom-to-solid from adatom-to-vapor
26 D_NW = (nu_NWav + nu_NWas) * difflength_NW^2; % diffusion constant on NW
27 beammulti_NW = 1;
28 F_NW = F_beam * beammulti_NW; % rate of beam flux onto NW
29
30 % for SiOx
31 difflength_SiO = 2000; % diffusion length on SiO
32 nu_SiOav = 25; % adatom to vapor rate factor on SiO
33 nu_SiOas = 0; % adatom to solid rate factor on SiO
```

```
34 D_SiO = 10 * 0.01 * (nu_SiOav + nu_SiOas) * difflength_SiO^2; % ...
       diffusion constant on NW
35 beammulti_SiO = 1;
36 F_SiO = F_beam * beammulti_SiO;
37 %% Form initial guess (4-array)
38 xmesh = sort(cat(2,xarray,[x1 x2 x3 x4]));
39 yinit = [1; 1];
40 sol = bvpinit(xmesh,yinit);
41 %% Solving differential equation with bvp5c (4-array)
42 sol = bvp5c(@(x,y,r) f(x,y,r), @bc, sol);
43 %% Flux in simple 1D infinite array Maple model
44 JNW2SiO = -D_NW * (-(nu_NWav + nu_NWas) ^ (-0.1e1 / 0.2e1) * D_NW ^ ...
       (-0.1e1 / 0.2e1) * exp(sqrt(nu_NWav + nu_NWas) * D_NW ^ (-0.1e1 / ...
       0.2e1) * w / 0.2e1) * sqrt(D_SiO) * sqrt(nu_SiOav) * ...
       (exp(sqrt(nu_SiOav) * D_SiO ^ (-0.1e1 / 0.2e1) * p / 0.2e1) * ...
       exp(-sqrt(nu_SiOav) * D_SiO ^ (-0.1e1 / 0.2e1) * w / 0.2e1) - ...
       exp(-sqrt(nu_SiOav) * D_SiO ^ (-0.1e1 / 0.2e1) * p / 0.2e1) * ...
       exp(sqrt(nu_SiOav) * D_SiO ^ (-0.1e1 / 0.2e1) * w / 0.2e1)) / ...
       (exp(sqrt(nu_SiOav) * D_SiO ^ (-0.1e1 / 0.2e1) * p / 0.2e1) * ...
       exp(-sqrt(nu_SiOav) * D_SiO ^ (-0.1e1 / 0.2e1) * w / 0.2e1) * ...
       exp(sqrt(nu_NWav + nu_NWas) * D_NW ^ (-0.1e1 / 0.2e1) * w / 0.2e1) ...
       * nu_SiOav ^ (0.3e1 / 0.2e1) * sqrt(D_SiO) + exp(sqrt(nu_SiOav) * ...
       D_SiO ^ (-0.1e1 / 0.2e1) * p / 0.2e1) * exp(-sqrt(nu_SiOav) * ...
       D_SiO ^ (-0.1e1 / 0.2e1) * w / 0.2e1) * exp(-sqrt(nu_NWav + ...
       nu_NWas) * D_NW ^ (-0.1e1 / 0.2e1) * w / 0.2e1) * nu_SiOav ^ ...
       (0.3e1 / 0.2e1) * sqrt(D_SiO) - exp(-sqrt(nu_SiOav) * D_SiO ^ ...
       (-0.1e1 / 0.2e1) * p / 0.2e1) * exp(sqrt(nu_SiOav) * D_SiO ^ ...
       (-0.1e1 / 0.2e1) * w / 0.2e1) * exp(sqrt(nu_NWav + nu_NWas) * D_NW ...
       ^ (-0.1e1 / 0.2e1) * w / 0.2e1) * nu_SiOav ^ (0.3e1 / 0.2e1) * ...
       sqrt(D_SiO) - exp(-sqrt(nu_SiOav) * D_SiO ^ (-0.1e1 / 0.2e1) * p / ...
       0.2e1) * exp(sqrt(nu_SiOav) * D_SiO ^ (-0.1e1 / 0.2e1) * w / ...
       0.2e1) * exp(-sqrt(nu_NWav + nu_NWas) * D_NW ^ (-0.1e1 / 0.2e1) * ...
       w / 0.2e1) * nu_SiOav ^ (0.3e1 / 0.2e1) * sqrt(D_SiO) + ...
       exp(sqrt(nu_SiOav) * D_SiO ^ (-0.1e1 / 0.2e1) * p / 0.2e1) * ...
       exp(-sqrt(nu_SiOav) * D_SiO ^ (-0.1e1 / 0.2e1) * w / 0.2e1) * ...
       exp(sqrt(nu_NWav + nu_NWas) * D_NW ^ (-0.1e1 / 0.2e1) * w / 0.2e1) ...
       * sqrt(nu_NWav + nu_NWas) * sqrt(D_NW) * nu_SiOav - ...
       exp(sqrt(nu_SiOav) * D_SiO ^ (-0.1e1 / 0.2e1) * p / 0.2e1) * ...
       exp(-sqrt(nu_SiOav) * D_SiO ^ (-0.1e1 / 0.2e1) * w / 0.2e1) * ...
       exp(-sqrt(nu_NWav + nu_NWas) * D_NW ^ (-0.1e1 / 0.2e1) * w / ...
       0.2e1) * sqrt(nu_NWav + nu_NWas) * sqrt(D_NW) * nu_SiOav + ...
       exp(-sqrt(nu_SiOav) * D_SiO ^ (-0.1e1 / 0.2e1) * p / 0.2e1) * ...
       exp(sqrt(nu_SiOav) * D_SiO ^ (-0.1e1 / 0.2e1) * w / 0.2e1) * ...
       exp(sqrt(nu_NWav + nu_NWas) * D_NW ^ (-0.1e1 / 0.2e1) * w / 0.2e1) ...
       * sqrt(nu_NWav + nu_NWas) * sqrt(D_NW) * nu_SiOav - ...
       exp(-sqrt(nu_SiOav) * D_SiO ^ (-0.1e1 / 0.2e1) * p / 0.2e1) * ...
       exp(sqrt(nu_SiOav) * D_SiO ^ (-0.1e1 / 0.2e1) * w / 0.2e1) * ...
       exp(-sqrt(nu_NWav + nu_NWas) * D_NW ^ (-0.1e1 / 0.2e1) * w / ...
       0.2e1) * sqrt(nu_NWav + nu_NWas) * sqrt(D_NW) * nu_SiOav) * (F_NW ...
       * nu_SiOav - F_SiO * nu_NWas - F_SiO * nu_NWav) + (nu_NWav + ...
       nu_NWas) ^ (-0.1e1 / 0.2e1) * D_NW ^ (-0.1e1 / 0.2e1) * ...
       exp(-sqrt(nu_NWav + nu_NWas) * D_NW ^ (-0.1e1 / 0.2e1) * w / ...
       0.2e1) * sqrt(D_SiO) * sqrt(nu_SiOav) * (exp(sqrt(nu_SiOav) * ...
```

```
    D_SiO ^ (-0.1e1 / 0.2e1) * p / 0.2e1) * exp(-sqrt(nu_SiOav) * ...
    D_SiO ^ (-0.1e1 / 0.2e1) * w / 0.2e1) - exp(-sqrt(nu_SiOav) * ...
    D_SiO ^ (-0.1e1 / 0.2e1) * p / 0.2e1) * exp(sqrt(nu_SiOav) * D_SiO ...
    ^ (-0.1e1 / 0.2e1) * w / 0.2e1)) / (exp(sqrt(nu_SiOav) * D_SiO ^ ...
    (-0.1e1 / 0.2e1) * p / 0.2e1) * exp(-sqrt(nu_SiOav) * D_SiO ^ ...
    (-0.1e1 / 0.2e1) * w / 0.2e1) * exp(sqrt(nu_NWav + nu_NWas) * D_NW ...
    ^ (-0.1e1 / 0.2e1) * w / 0.2e1) * nu_SiOav ^ (0.3e1 / 0.2e1) * ...
    sqrt(D_SiO) + exp(sqrt(nu_SiOav) * D_SiO ^ (-0.1e1 / 0.2e1) * p / ...
    0.2e1) * exp(-sqrt(nu_SiOav) * D_SiO ^ (-0.1e1 / 0.2e1) * w / ...
    0.2e1) * exp(-sqrt(nu_NWav + nu_NWas) * D_NW ^ (-0.1e1 / 0.2e1) * ...
    w / 0.2e1) * nu_SiOav ^ (0.3e1 / 0.2e1) * sqrt(D_SiO) - ...
    exp(-sqrt(nu_SiOav) * D_SiO ^ (-0.1e1 / 0.2e1) * p / 0.2e1) * ...
    exp(sqrt(nu_SiOav) * D_SiO ^ (-0.1e1 / 0.2e1) * w / 0.2e1) * ...
    exp(sqrt(nu_NWav + nu_NWas) * D_NW ^ (-0.1e1 / 0.2e1) * w / 0.2e1) ...
    * nu_SiOav ^ (0.3e1 / 0.2e1) * sqrt(D_SiO) - exp(-sqrt(nu_SiOav) * ...
    D_SiO ^ (-0.1e1 / 0.2e1) * p / 0.2e1) * exp(sqrt(nu_SiOav) * D_SiO ...
    ^ (-0.1e1 / 0.2e1) * w / 0.2e1) * exp(-sqrt(nu_NWav + nu_NWas) * ...
    D_NW ^ (-0.1e1 / 0.2e1) * w / 0.2e1) * nu_SiOav ^ (0.3e1 / 0.2e1) ...
    * sqrt(D_SiO) + exp(sqrt(nu_SiOav) * D_SiO ^ (-0.1e1 / 0.2e1) * p ...
    / 0.2e1) * exp(-sqrt(nu_SiOav) * D_SiO ^ (-0.1e1 / 0.2e1) * w / ...
    0.2e1) * exp(sqrt(nu_NWav + nu_NWas) * D_NW ^ (-0.1e1 / 0.2e1) * w ...
    / 0.2e1) * sqrt(nu_NWav + nu_NWas) * sqrt(D_NW) * nu_SiOav - ...
    exp(sqrt(nu_SiOav) * D_SiO ^ (-0.1e1 / 0.2e1) * p / 0.2e1) * ...
    exp(-sqrt(nu_SiOav) * D_SiO ^ (-0.1e1 / 0.2e1) * w / 0.2e1) * ...
    exp(-sqrt(nu_NWav + nu_NWas) * D_NW ^ (-0.1e1 / 0.2e1) * w / ...
    0.2e1) * sqrt(nu_NWav + nu_NWas) * sqrt(D_NW) * nu_SiOav + ...
    exp(-sqrt(nu_SiOav) * D_SiO ^ (-0.1e1 / 0.2e1) * p / 0.2e1) * ...
    exp(sqrt(nu_SiOav) * D_SiO ^ (-0.1e1 / 0.2e1) * w / 0.2e1) * ...
    exp(sqrt(nu_NWav + nu_NWas) * D_NW ^ (-0.1e1 / 0.2e1) * w / 0.2e1) ...
    * sqrt(nu_NWav + nu_NWas) * sqrt(D_NW) * nu_SiOav - ...
    exp(-sqrt(nu_SiOav) * D_SiO ^ (-0.1e1 / 0.2e1) * p / 0.2e1) * ...
    exp(sqrt(nu_SiOav) * D_SiO ^ (-0.1e1 / 0.2e1) * w / 0.2e1) * ...
    exp(-sqrt(nu_NWav + nu_NWas) * D_NW ^ (-0.1e1 / 0.2e1) * w / ...
    0.2e1) * sqrt(nu_NWav + nu_NWas) * sqrt(D_NW) * nu_SiOav) * (F_NW ...
    * nu_SiOav - F_SiO * nu_NWas - F_SiO * nu_NWav));
45 % positive J means NW act as sources rather than sinks
46 %% Extracting and plotting rho(x) (4-array)
47 ymulti = 1.2; % used for plotting lines indicating wire boundaries
48 yplotmax = ymulti*max(sol.y(1,:));
49
50 fontsmall = 14;
51 fontlarge = 16;
52
53 innersum = sum(sol.y(1,1+x1*xresolution:1+x2*xresolution)); % "sums" ...
       rho(x) on inner wire [x1 x2]
54 outersum = sum(sol.y(1,1+x3*xresolution:1+x4*xresolution)); % "sums" ...
       rho(x) on outer wire [x3 x4]
55 oiratio = outersum/innersum; % calculates outer/inner ratio
56
57 fignow = figure('visible', plotshow);
58     hold on
59     % nanowire boxes
60     NW1box = fill([x1,x2,x2,x1],[0,0,yplotmax,yplotmax],[0.4 0.4 ...
```

```
            0.4],'EdgeColor','none','DisplayName','Inner NW');
61      NW2box = fill([x3,x4,x4,x3],[0,0,yplotmax,yplotmax],[0.6 0.6 ...
            0.6],'EdgeColor','none','DisplayName','Outer NW');
62      % symmetry lines
63      midline = line([0 0], [0,yplotmax], 'LineWidth',2, 'Color', ...
            [0.8500, 0.3250, 0.0980],'DisplayName','Inner symmetry plane');
64      outline = line([x5 x5], [0,yplotmax], 'LineWidth',2, 'Color', ...
            [0.9290, 0.6940, 0.1250],'DisplayName','Outer symmetry plane');
65      % adatom density
66      rholine = plot(sol.x,sol.y(1,:),'-','LineWidth',2,'Color',[0, ...
            0.4470, 0.7410],'DisplayName','\rho(x), adatom density');
67      % legend
68      mylegend = legend([rholine NW1box NW2box ...
            midline],'Location','SouthEast','FontSize',11);
69          mylegend.Title.String = {['o/i ratio = ...
                ',num2str(oiratio,'%.3f')]};
70          mylegend.FontSize = fontsmall;
71      % plot title
72      ttl = title({['NW width: ',num2str(w),' | NW pitch: ',num2str(p)],...
73          ['NW rate: ',num2str(nu_NWav + nu_NWas),' | Mask rate: ...
                ',num2str(nu_SiOav + nu_SiOas)]});
74      ttl.FontSize = fontlarge;
75      % axes settings
76      xlb = xlabel('Position, x');
77      xlb.FontSize = fontsmall;
78      ylb = ylabel('Adatom density, \rho(x)');
79      ylb.FontSize = fontsmall;
80      xlim([0 3*x4]) % choose x-range for plotting
81      ylim([min(0,yplotmax) max(0,yplotmax)])
82  if plotsave == 1
83      saveas(fignow,'ada_density_ex.png')
84  end
85  %% Setting up derivatives (4-array) - see ...
        (https://se.mathworks.com/help/matlab/math/ ...
        solve-bvp-with-multiple-boundary-conditions.html)
86  function dydx = f(¬,y,region) % equations being solved - y(1)=rho, ...
        y(2)=drho/dx
87
88  global D_NW nu_NWav nu_NWas F_NW D_SiO nu_SiOav nu_SiOas F_SiO nuNWoverSiO
89
90  dydx = zeros(2,1);  % pre-allocate and define first derivatives from ...
        diff. equations
91  dydx(1) = y(2); % y(1) = rho, y(2) = drho/dx
92
93  switch region % 5 regions, mid is first
94      case 1 % x in [x0 x1] - SiO1
95          dydx(2) = (1/D_SiO)*(y(1)*(nu_SiOav + nu_SiOas) - F_SiO);
96      case 2 % x in [x1 x2] - NW1
97          dydx(2) = (1/D_NW)*(y(1)*(nu_NWav + nu_NWas) - F_NW);
98      case 3 % x in [x2 x3] - SiO2
99          dydx(2) = (1/D_SiO)*(y(1)*(nu_SiOav + nu_SiOas) - F_SiO);
100     case 4 % x in [x3 x4] - NW2
101         dydx(2) = (1/D_NW)*(y(1)*(nu_NWav + nu_NWas) - F_NW);
```

```
102     case 5 % x in [x4 x5] - SiO3
103         dydx(2) = (1/D_SiO)*(y(1)*(nu_SiOav + nu_SiOas) - F_SiO);
104 end
105 end
106 %% Setting boundary conditions (4-array) - implied equal to zero
107 function res = bc(YL,YR)
108 
109 global D_NW D_SiO nuNWoverSiO
110 
111 res = [YL(2,1) % drho/dx = 0 at x=0
112        YR(1,1) - YL(1,2) % continuity of rho at x=x1
113        D_SiO*YR(2,1) - D_NW*YL(2,2) % continuity of flux at x=x1
114        YR(1,2) - YL(1,3) % continuity of rho at x=x2
115        D_NW*YR(2,2) - D_SiO*YL(2,3) % continuity of flux at x=x2
116        YR(1,3) - YL(1,4) % continuity of rho at x=x3
117        D_SiO*YR(2,3) - D_NW*YL(2,4) % continuity of flux at x=x3
118        YR(1,4) - YL(1,5) % continuity of rho at x=x4
119        D_NW*YR(2,4) - D_SiO*YL(2,5) % continuity of flux at x=x4
120        YR(2,5)]; % drho/dx = 0 at x=x5=d/2
121 end
```

8.4.2 gamma_plot

This code generates 2D plots of the γ-function from section 4.1.

```
1  %% Choose plotting options
2  plotshow = 0; % show plots yes/no
3  plotsave = 1; % save plots yes/no
4  
5  fontsmall = 10;
6  fontlarge = 14;
7  %% Angles of facets
8  theta_t = 0;
9  theta_i = 25.24 * pi/180; % angle of 113-plane w.r.t. 001 substrate
10 theta_m = 35.26 * pi/180; % angle of 112-plane w.r.t. 001 substrate
11 theta_o = 54.74 * pi/180; % angle of 111-plane w.r.t. 001 substrate
12 theta_v = 90 * pi/180;
13 theta_r = -theta_o; % angle of raised facet - another 111 in this case
14     % t is always flat top, v is always vertical side
15 %% Composition of ternary alloy
16 Infrac = 0; % set fraction of Indium in InGaAs
17 %% Surface energy densities
18 % Values taken from Yeu 2019:
19 % https://www.nature.com/articles/s41598-018-37910-y - units ...
       [meV/angstrom^2]
20 % ------ GaAs ------: Yeu et. al. 2019: GaAs 973K (\mu=-5.9eV)
21 GaAs_E_t = 60; % 60(100)
22 GaAs_E_i = 56; % 56(113A) or 60.5(113B)
23     GaAs_E_m = 71.5; % 71.5 (112A) or 70.0 (112B) - translated from ...
           Jenichen2012
24 GaAs_E_o = 53; % 53(111A) or 45(111B) - surface vibration corrected
```

```
25 GaAs_E_v = 51; % 51(110) — cutoff near 54.5
26 GaAs_E_r = 53; % 53(111A) or 45(111B) — surface vibration corrected
27 % ——— InAs ———: Yeu et. al. 2019: InAs 773K (\mu=—5.65eV)
28 InAs_E_t = 48; % 48(100)
29 InAs_E_i = 44; % 44(113A) or 49(113B)
30     InAs_E_m = 70; % insert for functionality
31 InAs_E_o = 31; % 40(111A) or 31(111B) — surface vibration corrected
32 InAs_E_v = 40; % 40(110) — cutoff near 37.5
33 InAs_E_r = 31; % 40(111A) or 31(111B) — surface vibration corrected
34
35     % In_{Infrac}Ga[1—Infrac}As
36         Gafrac = 1—Infrac;
37     E_t = Infrac*InAs_E_t + (Gafrac)*GaAs_E_t;
38     E_i = Infrac*InAs_E_i + (Gafrac)*GaAs_E_i;
39         E_m = Infrac*InAs_E_m + (Gafrac)*GaAs_E_m;
40     E_o = Infrac*InAs_E_o + (Gafrac)*GaAs_E_o;
41     E_v = Infrac*InAs_E_v + (Gafrac)*GaAs_E_v;
42     E_r = Infrac*InAs_E_r + (Gafrac)*GaAs_E_r;
43
44 Emax = 75; thetatol = 4; % constant for overlap compensation, maximum ...
       SED, angular tolerance for cusp
45
46 ct = 0.95; ci = 0.75; cm = 0.75; co = 1; cv = 1; cr = 1; % c_hkl ...
       constants from eq. 20 (Krogstrup 2013) — assume unity
47 wt = thetatol*pi/180; wi = 0.5*thetatol*pi/180; wm = ...
       0.5*thetatol*pi/180; wo = thetatol*pi/180; wv = thetatol*pi/180; ...
       wr = thetatol*pi/180; % w_hkl constants from eq. 20 (Krogstrup ...
       2013) — assume unity
48 %% Angle vector
49 thetavec = linspace(0,pi/2,1000);
50 %     thetavec = [theta_v, theta_o, theta_i, 0]
51 tterm = ct*(Emax — E_t) ./ (1 + ((thetavec—theta_t)/wt).^2);
52 iterm = ci*(Emax — E_i) ./ (1 + ((thetavec—theta_i)/wi).^2);
53 mterm = cm*(Emax — E_m) ./ (1 + ((thetavec—theta_m)/wm).^2);
54 oterm = co*(Emax — E_o) ./ (1 + ((thetavec—theta_o)/wo).^2);
55 vterm = cv*(Emax — E_v) ./ (1 + ((thetavec—theta_v)/wv).^2);
56 rterm = cr*(Emax — E_r) ./ (1 + ((thetavec—theta_r)/wr).^2);
57
58 gammavec = Emax — (tterm + iterm + mterm + oterm + vterm + rterm);
59 %% Plotting
60 ku_red = [144, 26, 30] * 1/255;
61 ku_gold = [204, 166, 119] * 1/255;
62
63 xs = gammavec .* sin(thetavec);
64 ys = gammavec .* cos(thetavec);
65
66 figgamma = figure('Visible',plotshow);
67     hold on
68     grid on
69     pltg = plot(xs,ys,'Color',ku_red,'LineWidth',2);
70     plti = plot([0 Emax*tan(theta_i)],[0 Emax],'——k');
71     pltm = plot([0 Emax*tan(theta_m)],[0 Emax],'——k');
72     plto = plot([0 Emax*tan(theta_o)],[0 Emax],'——k');
```

```
73      xlim([0 Emax])
74      ylim([0 Emax])
75
76  if plotsave == 1
77      namecomp = strcat( 'gammaplot_Emax_', num2str(Emax),'_thetatol_', ...
            num2str(thetatol),'.png' );
78      saveas(figgamma, namecomp)
79  end
```

8.4.3 wulff_caller_timovr

This code generates equilibrium shape evolutions shown in sections 4.4.3 via a call of the function "wulff_func_timovr".
For high values of the surface energy density associated with facet m (introduced in section 4.4.4), this caller with associated function will produce plots as if the model was effectively 5-facet (as in section 4.4.3), since the m-facet will be excluded from the Wulff construction as shown in section 4.3.
For all intents and purposes this 6-facet model is more general, as is included the 5-facet model.

```
1  %% Choose plotting options
2  plotshow = 1; % show plots yes/no
3  plotsave = 0; % save plots yes/no
4
5  fontsmall = 10;
6  fontlarge = 14;
7  %% Angles of facets
8  theta_i = 25.24 * pi/180; % angle of 113-plane w.r.t. 001 substrate
9  theta_m = 35.26 * pi/180; % angle of 112-plane w.r.t. 001 substrate
10 theta_o = 54.74 * pi/180; % angle of 111-plane w.r.t. 001 substrate
11 theta_r = theta_o; % angle of raised facet - another 111 in this case
12     % t is always flat top, v is always vertical side
13 %% Composition of ternary alloy
14 Infrac = 0; % set fraction of Indium in InGaAs - naively assumin ...
       linear interpolation
15 %% Surface energy densities
16 % Values taken from Yeu 2019:
17 % https://www.nature.com/articles/s41598-018-37910-y - units ...
       [meV/angstrom^2]
18 % ------ GaAs ------: Yeu et. al. 2019: GaAs 973K (\mu=-5.9eV)
19 GaAs_E_t = 60; % 60(100)
20 GaAs_E_i = 56; % 56(113A) or 60.5(113B)
21     GaAs_E_m = 71.5; % 71.5 (112A) or 70.0 (112B) - translated from ...
           Jenichen2012
22 GaAs_E_o = 53; % 53(111A) or 45(111B) - surface vibration corrected
23 GaAs_E_v = 51; % 51(110) - cutoff near 54.5
24 GaAs_E_r = 53; % 53(111A) or 45(111B) - surface vibration corrected
25 % ------ InAs ------: Yeu et. al. 2019: InAs 773K (\mu=-5.65eV)
26 InAs_E_t = 48; % 48(100)
27 InAs_E_i = 44; % 44(113A) or 49(113B)
```

```
28      InAs_E_m = GaAs_E_m; % inset for code functionality - needs ...
            literature value
29  InAs_E_o = 40; % 40(111A) or 31(111B) - surface vibration corrected
30  InAs_E_v = 40; % 40(110) - cutoff near 37.5
31  InAs_E_r = 40; % 40(111A) or 31(111B) - surface vibration corrected
32
33      % In_{Infrac}Ga[1-Infrac}As
34          Gafrac = 1-Infrac;
35      E_t = Infrac*InAs_E_t + Gafrac*GaAs_E_t;
36      E_i = Infrac*InAs_E_i + Gafrac*GaAs_E_i;
37          E_m = Infrac*InAs_E_m + Gafrac*GaAs_E_m;
38      E_o = Infrac*InAs_E_o + Gafrac*GaAs_E_o;
39      E_v = Infrac*InAs_E_v + Gafrac*GaAs_E_v;
40      E_r = Infrac*InAs_E_r + Gafrac*GaAs_E_r;
41  %% Begin Volume loop (to show time evolution)
42  FullWidth = 120; % trenchs width
43  FullVolume = tan(theta_o)*(FullWidth/2)^2;
44
45  xmid = 0; % x-midpos of NW for plotting
46  yoff = 0; % y-basepos of NW boundaries for plotting
47
48  Vlow = 0.10 * FullVolume; % choose sweep parameters for volume - min ...
        volume
49  Vhigh = 1.50 * FullVolume;
50  Vstep = 0.10 * FullVolume;
51
52  Vpercent = 100*Vhigh/(FullVolume);
53
54  nVstep = 1; % current step
55      nVsteps = 1 + ceil((Vhigh-Vlow)/Vstep);
56
57  L_t  = zeros(1,nVsteps); % preallocate vector for t-facet lengths
58  L_i  = zeros(1,nVsteps);
59  L_m  = zeros(1,nVsteps);
60  L_o  = zeros(1,nVsteps);
61  L_v  = zeros(1,nVsteps);
62  L_r  = zeros(1,nVsteps);
63
64  xti = zeros(1,nVsteps); % preallocate vector for t-i boundary
65  yti = zeros(1,nVsteps);
66  xim = zeros(1,nVsteps);
67  yim = zeros(1,nVsteps);
68  xmo = zeros(1,nVsteps);
69  ymo = zeros(1,nVsteps);
70
71  Esols = zeros(1,nVsteps);
72
73  Volumes = zeros(1,nVsteps); % tracks widths for overgrowth
74  Widths = zeros(1,nVsteps);
75
76  for Volumevalue = Vlow:Vstep:Vhigh % sweep for volume
77  %% Define volumes and widths, then call
78      Volumes(nVstep) = Volumevalue; % save volume for plotting
```

```
79      HalfVolume = Volumevalue/2; % adjustments for all code written on ...
            right half side
80      HalfWidth = FullWidth/2;
81
82      B = HalfVolume;
83      W = HalfWidth;
84      Widths(nVstep) = 2*W; % save width for plotting (constant unless ...
            overgrowth)
85
86      % Solve minimum energy function, output facet lengths
87          Lsols = wulff_func_timovr(HalfVolume, HalfWidth, theta_i, ...
                theta_m, theta_o, theta_r, E_t, E_i, E_m, E_o, E_v, E_r);
88              L_t(nVstep) = Lsols(1); L_i(nVstep) = Lsols(2); ...
                    L_m(nVstep) = Lsols(3); L_o(nVstep) = Lsols(4); ...
                    L_v(nVstep) = Lsols(5); L_r(nVstep) = Lsols(6);
89              Esols(nVstep) = E_t*L_t(nVstep) + E_i*L_i(nVstep) + ...
                    E_m*L_m(nVstep) + E_o*L_o(nVstep) + E_v*L_v(nVstep) + ...
                    E_r*L_r(nVstep);
90
91      nVstep = nVstep + 1; % next step of volume sweep
92  end % Ends volume loop
93  %% Plot boundary evolution
94  % total lengths of facets: ———————— REDO FROM HERE TO INCLUDE V FACET!
95  Lx_t = L_t;
96  Ly_t = zeros(1,nVsteps);
97
98  Lx_i = L_i * cos(theta_i); % horizontal length of i-facet
99  Ly_i = L_i * sin(theta_i); % vertical length of i-facet
100
101 Lx_m = L_m * cos(theta_m);
102 Ly_m = L_m * sin(theta_m);
103
104 Lx_o = L_o * cos(theta_o);
105 Ly_o = L_o * sin(theta_o);
106
107 Lx_v = zeros(1,nVsteps);
108 Ly_v = L_v;
109
110 Lx_r = L_r * cos(theta_r);
111 Ly_r = L_r * sin(theta_r);
112 %% Plotting sample solution
113 %(k, nVstep)
114 xt = [zeros(1,nVsteps); L_t]; % x goes 0 to t
115 yt = [Ly_t+Ly_i+Ly_m+Ly_o+Ly_v+Ly_r; Ly_i+Ly_m+Ly_o+Ly_v+Ly_r]; % y ...
        goes timovr to imovr
116
117 xi = [L_t; L_t+Lx_i]; % x goes t to ti
118 yi = [Ly_i+Ly_m+Ly_o+Ly_v+Ly_r; Ly_m+Ly_o+Ly_v+Ly_r]; % y goes imovr ...
        to movr
119
120 xm = [L_t+Lx_i; L_t+Lx_i+Lx_m]; % x goes ti to tim
121 ym = [Ly_m+Ly_o+Ly_v+Ly_r; Ly_o+Ly_v+Ly_r]; % y goes movr to ovr
122
```

```
123 xo = [L_t+Lx_i+Lx_m; L_t+Lx_i+Lx_m+Lx_o]; % x goes tim to timo
124 yo = [Ly_o+Ly_v+Ly_r; Ly_v+Ly_r]; % y goes ovr to vr
125
126 xv = [L_t+Lx_i+Lx_m+Lx_o; L_t+Lx_i+Lx_m+Lx_o+Lx_v]; % x goes timo to timov
127 yv = [Ly_v+Ly_r; Ly_r]; % y goes vr to v
128
129 xr = [L_t+Lx_i+Lx_m+Lx_o+Lx_v; L_t+Lx_i+Lx_m+Lx_o+Lx_v-Lx_r]; % x goes ...
        timov to timovr
130 yr = [Ly_r; zeros(1,nVsteps)]; % y goes r to 0
131 %% Do figure
132 strcomp = strcat( 'Growth of In_{', num2str(Infrac),'}Ga_{', ...
        num2str(Gafrac),'}As' );
133
134     if plotshow == 1
135         figshow = 'on';
136     elseif plotshow == 0
137         figshow = 'off';
138     end
139
140 lw = 1;
141
142 fig_tiovr = figure('Visible',figshow);
143     hold on
144     grid on
145     set(gca,'DataAspectRatio',[1 1 1])
146
147     plot(xt+xmid,yt+yoff, 'k', 'LineWidth', lw) % plots right sides
148     plot(xi+xmid,yi+yoff, 'k', 'LineWidth', lw)
149     plot(xm+xmid,ym+yoff, 'r', 'LineWidth', lw)
150     plot(xo+xmid,yo+yoff, 'k', 'LineWidth', lw)
151     plot(xv+xmid,yv+yoff, 'k', 'LineWidth', lw)
152     plot(xr+xmid,yr+yoff, 'k', 'LineWidth', lw)
153     plot(-xt+xmid,yt+yoff, 'k', 'LineWidth', lw) % plots left sides
154     plot(-xi+xmid,yi+yoff, 'k', 'LineWidth', lw)
155     plot(-xm+xmid,ym+yoff, 'r', 'LineWidth', lw)
156     plot(-xo+xmid,yo+yoff, 'k', 'LineWidth', lw)
157     plot(-xv+xmid,yv+yoff, 'k', 'LineWidth', lw)
158     plot(-xr+xmid,yr+yoff, 'k', 'LineWidth', lw)
159 scatter([-FullWidth/2+xmid FullWidth/2+xmid],[0+yoff 0+yoff],'kd', ...
        'filled') % Width markers
160
161 if plotsave == 1
162     filenameex = ['/shapes/wulff_reprod_timovr.png'];
163     saveas(fig_tiovr, [pwd filenameex])
164 end
```

8.4.4 wulff_func_timovr

This code minimizes surface energies under constraints via the MATLAB-internal function `'fmincon'` which minimizes a given function under a set of constraints. "wulff_func_timovr" is called by "wulff_caller_timovr" and "excesses_dGdN".

```
1  function Lsols = wulff_func_timovr(volume, width, theta_i, theta_m, ...
       theta_o, theta_r, E_t, E_i, E_m, E_o, E_v, E_r)
2      %% Define geometry
3      W=width; V=volume;
4      Et=E_t; Ei=E_i; Em=E_m; Eo=E_o; Ev=E_v; Er=E_r;
5      thetai=theta_i; thetam=theta_m; thetao=theta_o; thetar=theta_r;
6      %%
7      funE = @(L) Et*L(1) + Ei*L(2) + Em*L(3) + Eo*L(4) + Ev*L(5) + ...
           Er*L(6); % Energy function to be minimized, Lt=L(1), Li=L(2), ...
           Lm=L(3), Lo=L(4), Lv=L(5), Lr=L(6)
8      L0s = [W/2, W/4, W/8, W/4, 0, 0]; % initial guesses for lengths
9
10     A = []; % linear inequality constraints - none, since bound are ...
           set by "lb" and "ub"
11     b = [];
12     Aeq = []; % linear equality constraints - none
13     beq = [];
14
15     lb = [0,0,0,0,0,0]; % all length values must be 0+
16     ub = [];
17
18     options = optimoptions('fmincon','Display','off'); % suppresses ...
           large text output for each iteration of solution
19
20     Lsols = fmincon(funE, L0s, A, b, Aeq, beq, lb, ub, @nonlinconstr, ...
           options);
21     %% L(3)cal functions used
22     function [c,ceq] = nonlinconstr(L) % c's are inequalities implied ...
           less than or equal to zero, ceq's are equalities implied equal ...
           to zero
23         c = []; % no inequality constraints
24         ceq(1) = V - ((1/2)*(L(1) + L(1) + ...
               L(2)*cos(thetai))*L(2)*sin(thetai) ...
25             + (1/2)*(L(1) + L(2)*cos(thetai) + L(1) + L(2)*cos(thetai) ...
                   + L(3)*cos(thetam))*L(3)*sin(thetam) ...
26             + (1/2)*(L(1) + L(2)*cos(thetai) + L(3)*cos(thetam) + L(1) ...
                   + L(2)*cos(thetai) + L(3)*cos(thetam) + ...
                   L(4)*cos(thetao))*L(4)*sin(thetao) ...
27             + (L(1) + L(2)*cos(thetai) + L(3)*cos(thetam) + ...
                   L(4)*cos(thetao))*L(5) ...
28             + (1/2)*(W + W + L(6)*cos(thetar))*L(6)*sin(thetar)); % ...
                   volume equality - implied equal to zero
29         ceq(2) = (W + L(6)*cos(thetar)) - (L(1) + L(2)*cos(thetai) + ...
               L(3)*cos(thetam) + L(4)*cos(thetao)); % width equality
30     end
31 end
```

8.4.5 excesses_dGdN

This code generates figure 29, in part via a call of the function "wulff_func_timovr" and subsequent numerical differentiation.

```
1 %% Choose plotting options
2 plotshowdEdN = 1; % show plots yes/no
3 plotsave = 1; % save plots yes/no
4
5 fontsmall = 11;
6 fontlarge = 12;
7 %% Angles of facets
8 theta_i = 25.24 * pi/180; % angle of 113-plane w.r.t. 001 substrate
9 theta_m = 35.26 * pi/180; % angle of 112-plane w.r.t. 001 substrate
10 theta_o = 54.74 * pi/180; % angle of 111-plane w.r.t. 001 substrate
11 theta_r = theta_o; % angle of raised facet - another 111 in this case
12     % t is always flat top, v is always vertical side
13 %% Composition of ternary alloy
14 Infrac = 0; % set fraction of Indium in InGaAs
15 volstep = 0.01;
16 finalVmulti = 2.25; % final step is finalmulti times full pyramid
17 %% Surface energy densities
18 % Values taken from Yeu 2019: ...
       https://www.nature.com/articles/s41598-018-37910-y
19 % ------ GaAS ------: Yeu et. al. 2019: GaAs 973K (\mu=-5.9eV)
20 GaAs_E_t = 60 * 100; % 60(100) - 0.01 factor conversion [meV/AA^2] -> ...
       [meV*/nm^2]
21 GaAs_E_i = 56 * 100; % 56(113A) or 60.5(113B)
22     GaAs_E_m = 71.5* 100; % 71.5 (112A) or 70.0 (112B) - translated ...
           from Jenichen2012
23 GaAs_E_o = 53 * 100; % 53(111A) or 45(111B) - surface vibration corrected
24 GaAs_E_v = 51 * 100; % 51(110) - cutoff near 54.5
25 GaAs_E_r = 53 * 100; % 53(111A) or 45(111B) - surface vibration corrected
26 % ------ InAs ------: Yeu et. al. 2019: InAs 773K (\mu=-5.65eV)
27 InAs_E_t = 48 * 100; % 48(100)
28 InAs_E_i = 44 * 100; % 44(113A) or 49(113B)
29     InAs_E_m = GaAs_E_m; % inset for code functionality - needs ...
           literature value
30 InAs_E_o = 40 * 100; % 40(111A) or 31(111B) - surface vibration corrected
31 InAs_E_v = 40 * 100; % 40(110) - cutoff near 37.5
32 InAs_E_r = 40 * 100; % 40(111A) or 31(111B) - surface vibration corrected
33
34     % In_{Infrac}Ga[1-Infrac}As
35         Gafrac = 1-Infrac;
36     E_t = Infrac*InAs_E_t + Gafrac*GaAs_E_t;
37     E_i = Infrac*InAs_E_i + Gafrac*GaAs_E_i;
38         E_m = Infrac*InAs_E_m + Gafrac*GaAs_E_m;
39     E_o = Infrac*InAs_E_o + Gafrac*GaAs_E_o;
40     E_v = Infrac*InAs_E_v + Gafrac*GaAs_E_v;
41     E_r = Infrac*InAs_E_r + Gafrac*GaAs_E_r;
42
43     Omega = (1/4) * (Infrac*0.60583^3 + Gafrac*0.565325^3); % 4 pairs ...
           per unit cell
44     gammat = Infrac*InAs_E_t + Gafrac*GaAs_E_t;
45     gammao = Infrac*InAs_E_o + Gafrac*GaAs_E_o;
46
47 epsilon1 = 0; % strain contributions
48 epsilon2 = 0;
```

```
49 %% Begin Volume loop (to show time evolution)
50 FullWidth = 120; % trenchs width
51 FullVolume = tan(theta_o)*(FullWidth/2)^2;
52
53 Vlow = volstep * FullVolume; % choose sweep parameters for volume
54 Vhigh = finalVmulti * FullVolume;
55
56 Vstep = volstep * FullVolume;
57 Vpercent = 100*Vhigh/(FullVolume);
58 %% 2-facet Δ-mu calculations (<111> and <001>)
59 num = 50; % number of intervals for plots
60 h_max = (FullWidth/2) * tan(theta_o); % max height of pyramid
61 h1array = linspace(1,num,num) * h_max / num;
62 h2_max = ...
       (sqrt(4*cot(theta_o)*(finalVmulti-1)*(FullVolume/2)+FullWidth^2) - ...
       FullWidth) / cot(theta_o);
63 h2array = linspace(1,num,num) * h2_max / num;
64
65 csa1 = FullWidth .* h1array - cot(theta_o).*h1array.^2;
66 csa2 = (FullWidth/2) * h_max + 2 * ( h2array.*(FullWidth/2) + ...
       h2array.^2*cot(theta_o)/4 );
67 %% Preallocating for volume loop
68 nVstep = 1;
69 nVsteps = 1 + floor((Vhigh-Vlow)/Vstep);
70
71 L_t  = zeros(1,nVsteps); % preallocate vector for t-facet lengths
72 L_i  = zeros(1,nVsteps);
73 L_o  = zeros(1,nVsteps);
74 L_v  = zeros(1,nVsteps);
75 L_r  = zeros(1,nVsteps);
76
77     L_t_e = zeros(1,nVsteps); % preallocate vector for t-facet lengths
78     L_o_e = zeros(1,nVsteps);
79     L_r_e = zeros(1,nVsteps);
80
81 xti = zeros(1,nVsteps); % preallocate vector for t-i boundary
82 yti = zeros(1,nVsteps);
83 xio = zeros(1,nVsteps);
84 yio = zeros(1,nVsteps);
85
86 Esols = zeros(1,nVsteps);
87     Esols_e = zeros(1,nVsteps);
88
89 Volumes = zeros(1,nVsteps); % tracks widths for overgrowth
90
91 for Volumevalue = Vlow:Vstep:Vhigh % sweep for volume
92 %% Wulff caller (V, Ea, Ev) with first facet being most horizontal
93     Volumes(nVstep) = Volumevalue; % save volume for plotting
94     HalfVolume = Volumevalue/2; % adjustments for all code written on ...
           right half side
95     HalfWidth = FullWidth/2;
96
97     % full 6-facet model
```

```
98          Lsols = wulff_func_timovr(HalfVolume, HalfWidth, theta_i, ...
                theta_m, theta_o, theta_r, E_t, E_i, E_m, E_o, E_v, E_r);
99              L_t(nVstep) = Lsols(1); L_i(nVstep) = Lsols(2); ...
                    L_m(nVstep) = Lsols(3); L_o(nVstep) = Lsols(4); ...
                    L_v(nVstep) = Lsols(5); L_r(nVstep) = Lsols(6);
100             Esols(nVstep) = 2*( E_t*L_t(nVstep) + E_i*L_i(nVstep) + ...
                    E_o*L_o(nVstep) + E_v*L_v(nVstep) + E_r*L_r(nVstep) );
101
102     if Volumevalue ≤ FullVolume % treats the restricted case regime 1
103         hnow = ( FullWidth − sqrt(FullWidth^2 − ...
                4*cot(theta_o)*Volumevalue) ) / (2*cot(theta_o));
104             Esols_e(nVstep) = 2* ( E_t * (HalfWidth−cot(theta_o)*hnow) ...
                    + E_o * (hnow/sin(theta_o)) );
105     elseif Volumevalue > FullVolume % treats the restricted case ...
            regime 2
106         hnow = ( sqrt(4*cot(theta_o)*HalfVolume + FullWidth^2) − ...
                FullWidth ) / cot(theta_o);
107         l = FullWidth/(2*cos(theta_o)); d = hnow/(2*sin(theta_o));
108         Esols_e(nVstep) = 2*E_o*( l+2*d );
109     end
110     nVstep = nVstep + 1; % next step of volume sweep
111 end % Ends volume loop
112 %% Analytic solutions for <111> and [001] facet model
113 Δmu_s_h = ( Omega*(gammao − gammat*cos(theta_o)) ) ./ ( sin(theta_o)*( ...
        HalfWidth − cot(theta_o)*h1array ) ) + epsilon1;
114 Δmu_s_h2 = ( Omega*gammao ) ./ ( sin(theta_o)*( HalfWidth + ...
        h2array*cot(theta_o)./2 ) ) + epsilon2;
115
116 nAtoms = Volumes ./ (Omega); % number of atoms in volume − half ...
        because of symmetry used throughout
117 dEdnA = diff(Esols) ./ diff(nAtoms);
118 volcut = Volumes([1:end−1]);
119 %% Plot boundary evolution
120 % total lengths of facets
121 Lx_t = L_t;
122 Ly_t = zeros(1,nVsteps);
123
124 Lx_i = L_i * cos(theta_i); % horizontal length of i−facet
125 Ly_i = L_i * sin(theta_i); % vertical length of i−facet
126
127 Lx_o = L_o * cos(theta_o);
128 Ly_o = L_o * sin(theta_o);
129
130 Lx_v = zeros(1,nVsteps);
131 Ly_v = L_v;
132
133 Lx_r = L_r * cos(theta_r);
134 Ly_r = L_r * sin(theta_r);
135 %% Plotting sample solution
136 %(k, nVstep)
137 xt = [zeros(1,nVsteps); L_t];
138 yt = [Ly_t+Ly_i+Ly_o+Ly_v+Ly_r; Ly_i+Ly_o+Ly_v+Ly_r];
139
```

```
140 xi = [L_t; L_t+Lx_i];
141 yi = [Ly_i+Ly_o+Ly_v+Ly_r; Ly_o+Ly_v+Ly_r];
142
143 xo = [L_t+Lx_i; L_t+Lx_i+Lx_o];
144 yo = [Ly_o+Ly_v+Ly_r; Ly_v+Ly_r];
145
146 xv = [L_t+Lx_i+Lx_o; L_t+Lx_i+Lx_o];
147 yv = [Ly_r; Ly_v+Ly_r];
148
149 xr = [L_t+Lx_i+Lx_o; L_t+Lx_i+Lx_o-Lx_r];
150 yr = [Ly_r; zeros(1,nVsteps)];
151 %% Setup for figures
152 c1 = [0, 0, 0];
153 c2 = [0.20, 0.20, 0.20];
154 c3 = [0.40, 0.40, 0.40];
155 c4 = [0.60, 0.60, 0.60];
156 c5 = [0.80, 0.80, 0.80];
157
158 plotnamecomp = strcat( 'excesses_regimes_In', num2str(Infrac), '_Ga', ...
        num2str(Gafrac), '_As.png' );
159 strcomp = strcat( 'Growth of In_{', num2str(Infrac), '}Ga_{', ...
        num2str(Gafrac), '}As' );
160
161     if plotshowdEdN == 1
162         figshowdEdN = 'on';
163     elseif plotshowdEdN == 0
164         figshowdEdN = 'off';
165     end
166
167     lw = 2;
168 %% Do figures
169 % strcomp = [];
170
171 fig_dEdN = figure('Visible',figshowdEdN);
172     hold on
173     grid on
174         reg1 = plot(csa1, Δmu_s_h, 'Color', c4, 'LineWidth', lw, ...
                'DisplayName', '3-facet model analytic');
175         reg2 = plot(csa2, Δmu_s_h2, 'Color', c4, 'LineWidth', lw);
176         tiovr = ...
                plot(volcut,dEdnA,'Color',c1,'LineWidth',lw,'DisplayName', ...
                '5-facet model numerical');
177     xlb = xlabel('Cross sectional area [nm^2]', 'FontSize', fontsmall);
178     ylb = ylabel('\Δ\mu_{s} [meV]', 'FontSize', fontsmall);
179     ylim([0, 0.5/1000]);
180     lgd = legend([reg1 tiovr],'FontSize', fontsmall, 'Location', ...
            'SouthEast');
181
182 if plotsave == 1
183     filename_dEdN = strcat('tiovr_dEdN_In', num2str(Infrac), 'Ga', ...
            num2str(Gafrac), 'As.png');
184     saveas(fig_dEdN, filename_dEdN)
185 end
```